Ups and Downs with a Bit of Strange: A STAR Analysis of $\pi/K/p$ Spectra at High p_T in Au+Au collisions at $\sqrt{s_{NN}}$ = 7.7, 11.5, 19.6, 27.0, 39.0, and 62.4 GeV and Its Physics Implications

by

Evan Warren Sangaline

A dissertation submitted in partial satisfaction of the
requirements for the degree of
Doctor of Philosophy

in

Physics

in the

Graduate Division
of the
University of California, Davis

Committee in charge:

Professor Daniel Cebra, Chair
Professor Manuel Calderón de la Barca Sánchez
Professor Ramona Vogt

Spring 2014

The dissertation of Evan Warren Sangaline, titled Ups and Downs with a Bit of Strange: A STAR Analysis of $\pi/K/p$ Spectra at High p_T in Au+Au collisions at $\sqrt{s_{NN}} = 7.7$, 11.5, 19.6, 27.0, 39.0, and 62.4 GeV and Its Physics Implications, submitted in partial satisfaction of the requirements for the degree of

Doctor of Philosophy

Master of Science

in Nuclear Physics

Daniel Cebra, Chair — Date

Manuel Calderón de la Barca Sánchez — Date

Ramona Vogt — Date

University of California, Davis

Ups and Downs with a Bit of Strange: A STAR Analysis of $\pi/K/p$ Spectra at High p_T in Au+Au collisions at $\sqrt{s_{NN}}$ = 7.7, 11.5, 19.6, 27.0, 39.0, and 62.4 GeV and Its Physics Implications

Evan Warren Sangaline

Abstract

Ups and Downs with a Bit of Strange: A STAR Analysis of $\pi/K/p$ Spectra at High p_T in Au+Au collisions at $\sqrt{s_{NN}}$ = 7.7, 11.5, 19.6, 27.0, 39.0, and 62.4 GeV and Its Physics Implications

by

Evan Warren Sangaline

Doctor of Philosophy in Physics

University of California, Davis

Professor Daniel Cebra, Chair

This is Evan's abstract.

To the mermaid and the polar bear, wherever she may be.
Oh... and my parents, advisor, friends, and stuff too.

Contents

List of Figures

List of Tables

List of Acronyms

AGS Alternating Gradient Synchrotron. 9, 19, 79

BBC Beam-Beam Counter. 30

BEMC Barrel Electro-Magnetic Calorimeter. 30

BES Beam Energy Scan. 1, 14, 15, 17, 19, 29, 31, 41, 48, 53, 78, 79, 81, 82, 89

BNL Brookhaven National Laboratory. 1, 16

BRAHMS Broad RAnge Hadron Magnetic Spectrometers. 1, 19, 20

BTA Booster-To-AGS. 19

CERN European Council for Nuclear Research. 1

CFN Center for Functional Nanomaterials. 16

CTB Central Trigger Barrel. 30

DCA Distances of Closest Approach. 31–33, 36, 41, 69

DELPHI Detector with Lepton, Photon, and Hadron Identification. 10

FGT Forward GEM Tracker. 20

GEANT4 GEometry ANd Tracking version 4. 67, 69, 74

GMC Glauber Monte Carlo. 42–44

IFC Inner Field Cage. 21

IR Interaction Region. 19, 30

ISR Intersecting Storage Rings. 10

L0 Level 0. 30

L1 Level 1. 30

L2 Level 2. 30

L3 Level 3. 30

LEP Large Electron-Positron Collider. 10

LHC Large Hadron Collider. 1, 3, 6, 13, 65, 78, 79, 82

MC Monte Carlo. 42, 44, 67, 69

MRPC Multigap Resistive Plate Chamber. 25–27, 36, 38

MTD Muon Telescope Detector. 20

MWPC Multi-Wire Proportional Chamber. 22, 23

NNDC National Nuclear Data Center. 16

NSLS National Synchrotron Light Source. 16

PHENIX Pioneering High Energy Nuclear Interaction eXperiment. 1, 4, 5, 9–11, 19, 20

PHOBOS ?. 1–3, 19, 20, 78, 82

PID Particle Identification. 31, 51, 54, 76

pQCD Perturbative Quantum Chromodynamics. 66

QCD Quantum Chromodynamics. 1, 2, 11, 12

QGP Quark Gluon Plasma. 1, 11, 13, 14, 76, 82, 89, 90

RCF RHIC Computing Facility. 16

RF Radio Frequency. 19, 23

RHIC Relativistic Heavy Ion Collider. 1–4, 11–19, 29–31, 65, 66, 76, 78, 79, 89

SPS Super Proton Synchrotron. 1, 9, 14, 16, 65, 76, 78, 79, 89

sQGP strongly interacting QGP. 13

STAR Solenoidal Tracker at RHIC. 1, 4–6, 14, 19–22, 24, 26, 29, 30, 39, 41, 42, 51, 53, 67, 69, 74, 76, 79, 89

TOF Time-of-Flight. 25–27, 33, 36, 51, 53, 57, 61, 62, 69

TPC Time Projection Chamber. 20–26, 31, 33, 36, 41, 51, 62, 67

TTB Tandem-To-Booster. 19

upVPD Upgraded Pseudo Vertex Position Detector. 26

UrQMD Ultrarelativistic Quantum Molecular Dynamics. 69, 71, 72

ZDC Zero Degree Calorimeter. 30

Chapter 1

Introduction

When the Relativistic Heavy Ion Collider (RHIC) at Brookhaven National Laboratory (BNL) began operation in 2000, a new high energy frontier was reached in the field of nuclear physics. The highest heavy-ion collision energies before RHIC were achieved at the Super Proton Synchrotron (SPS) at European Council for Nuclear Research (CERN) with center of mass collision energies of 17.3 GeV, over an order of magnitude below the 200 GeV top energy of RHIC due, in part, to it being a fixed target accelerator. A wide range of results were quickly produced by the experiments at RHIC which directly addressed the question of whether a Quark Gluon Plasma (QGP) was formed.

In 2005, Broad RAnge Hadron Magnetic Spectrometers (BRAHMS), Pioneering High Energy Nuclear Interaction eXperiment (PHENIX), ? (PHOBOS), and Solenoidal Tracker at RHIC (STAR) each published a whitepaper summarizing their results and how they related to the possibility of QGP formation. The perspectives expressed in those papers largely set the tone of exploration for both the higher energy collisions that have since been studied at the Large Hadron Collider (LHC) at CERN and the low energy Beam Energy Scan (BES) program that has taken place at RHIC. The BES program will be the focus of this thesis. We will begin by introducing several of the most important observations in the RHIC whitepapers and discuss how LHC results have evolved our understanding where applicable. From here, we will go through some of the motivations for the BES program and then present several new analyses that further extend our understanding of Quantum Chromodynamics (QCD) physics. Note that natural units with $c = 1$ will be

used throughout.

1.1 Signatures of a Deconfined State of QCD Matter

Many interesting physics measurements have came out of RHIC, too many to cover entirely in a brief overview. We will instead focus on a sampling of those that are particularly relevant as signatures of a deconfined state of QCD matter. These observables will also be of key importance at lower collision energies in order to better understand the QCD phase diagram.

1.1.1 Energy Density and Integrated Yields

Intuitively, it seems reasonable to expect a possible breakdown of hadronic stability when the energy density significantly exceeds the ~ 500 MeV/fm^3 density of a nucleon. In fact, as a result of this, the idea of using relativistic heavy-ion collisions to study the behavior of nuclear matter at high energy densities actually predates the formulation of QCD [1]. By the time of RHIC, our theoretical understanding of nuclear matter had progressed significantly. Lattice QCD calculations predicted a critical energy density of $\epsilon_c = 700 \pm 50\%$ MeV/fm^3, above which there would exist a distinct state of QCD matter [2].

PHOBOS estimated the energy density [3] in 6% central Au+Au collisions at $\sqrt{s_{NN}} =$ 200 GeV to be 5 GeV/fm^3 [4]. This estimate was made using the volume assumptions proposed by Bjorken: negligible radial expansion and a longitudinal extent of 2 fm. These assumptions are commonly used and the resulting energy density estimate is often called the Bjoreken energy density. Additionally, they used elliptic flow results to place an upper limit of 2 fm on the time for the system to reach equilibrium which produces a lower bound of ≥ 3 GeV/fm^3 with the assumption of $\beta_{\parallel} \approx 1$ for longitudinal expansion and $\beta_{\perp} \approx 0.6$ for radial expansion [4]. This conservative estimate far exceeded the lattice QCD predictions and was an incredible six times higher than the density of a nucleon. It may not be particularly surprising given the energy of the projectiles, but this measurement of an energy density that is clearly above lattice QCD predictions for a phase transition is one

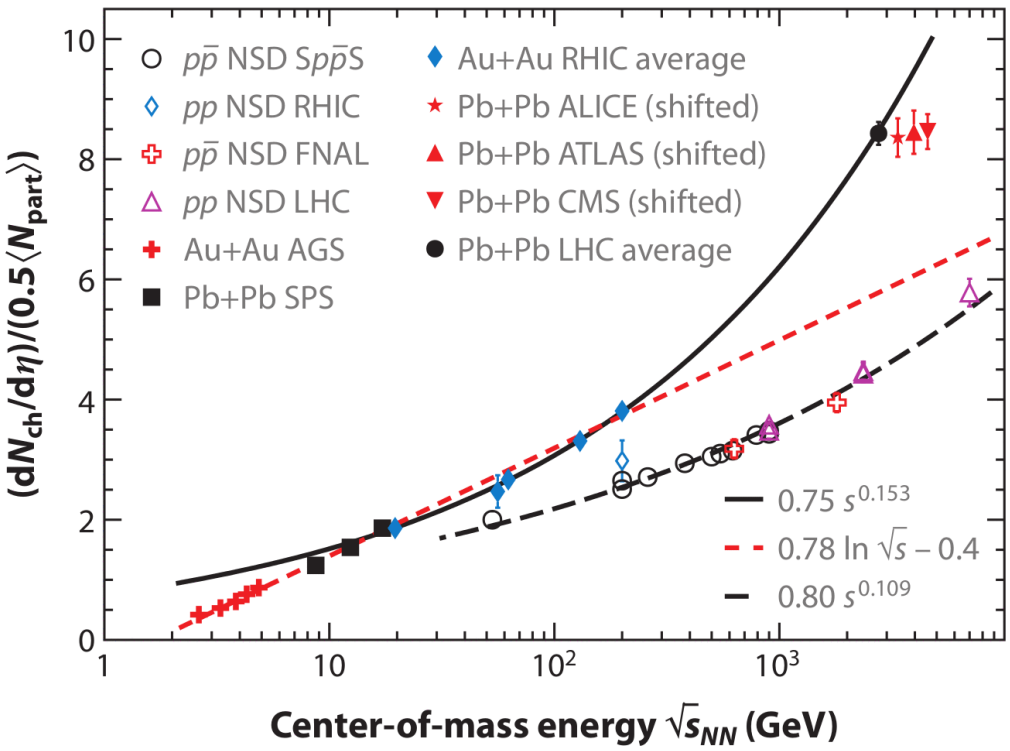

Figure 1.1: Charge particle pseudorapidity density

Densities of charged particles at mid-rapidity in p+p and A+A collisions at a wide range of collision energies [5]. The straight dashed line shows the logarithmic fit that was shown in the PHOBOS whitepaper [4]. The LHC results demonstrated that the logarithmic scaling did not extend to higher energies and that a power-law fit does a reasonable job of describing the data above 19.6 GeV.

of the most unambiguous RHIC observations.

The LHC experiments estimated a Bjorken energy density of 15 GeV/fm^3 for Pb+Pb collisions with $\sqrt{s_{NN}} = 2.76$ TeV which is of course significantly higher than that of RHIC [5, 6]. They also measured integrated yields which are often used as proxy for energy density when $\langle m_T \rangle$ is not changing drastically. The results are shown in Figure 1.1 where a clear breaking of the previously observed logarithmic scaling can be seen. Measurements of $^{dN_{\rm ch}}/_{d\eta}$ and energy density at additional collision energies would help to understand the scaling behavior of these two related quantities.

1.1.2 Elliptic Flow and n_q Scaling

When elliptic flow results were produced from RHIC data, there was pronounced splitting observed between mesons and baryons with baryons exhibiting more flow. The increased v_2 in baryons was not consistent with a picture of hadronic flow but could easily be described by partonic flow. Take the scenario where quarks were flowing hydrodynamically and for a given transverse momentum followed a density distribution ${}^{dN}/_{d\phi}$ proportional to $1 + 2v_2 \cos(\phi - \Psi)$. If the quarks then coalesced into hadrons we would expect the meson cross section to go as $({}^{dN}/_{d\phi})^2$ resulting in a density distribution proportional to $(1 + 2v_2 \cos(\phi - \Psi))^2 \approx 1 + 4v_2 \cos(\phi - \Psi)$ and the baryon cross section to go as $({}^{dN}/_{d\phi})^3$ resulting in a density distribution proportional to $(1 + 2v_2 \cos(\phi - \Psi))^3 \approx 1 + 6v_2 \cos(\phi - \Psi)$. The linear terms are a sufficient approximation here because $v_2^2 \ll v_2 \ll 1$. Additionally, the naive expectation would be that the momentum of the resulting hadron is the sum of the constituent quarks. Scaling both the measured v_2 and the transverse momentum by the number of constituent quarks should result in consistent measurements between mesons and baryons if quarks are flowing freely and coalescing.

STAR and PHENIX flow results scaled by the number of constituent quarks, n_q, can be seen in Figure 1.2. There is generally reasonable agreement, certainly better than without the scaling. Despite this, the pions very clearly appear to be shifted to a lower p_T than the other, heavier, particles. Since these early observations it has become better understood that the assumption that the momentum of the resulting hadron will be the sum of the constituent quarks is too simplistic. The chiral symmetry breaking during coalescence results in far more massive hadrons than what the sum of the quark masses would suggest. As a result of this, ${}^{(m_T - m_0)}/_{n_q}$ is a more natural scaling than ${}^{p_T}/_{n_q}$ and resolves the pion discrepancy. Elliptic flow won't be addressed directly in the work done in this thesis but it stands as one of the strongest signatures that a state of matter with partonic degrees of freedom is created in heavy-ion collisions.

1.1.3 High p_T Particle Suppression

One of the most striking features observed in the RHIC 200 GeV data was the apparent suppression of high p_T particles. Particles with transverse momentum larger than

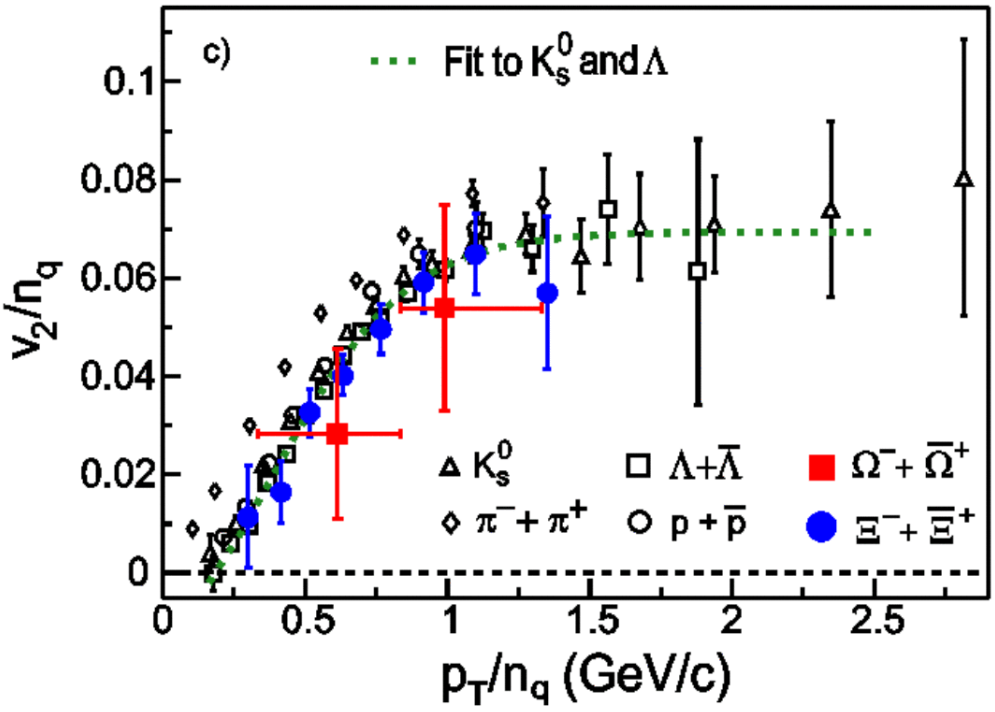

Figure 1.2: STAR and PHENIX Elliptic Flow Results

STAR results on elliptic flow for K^s_0, Λ [7], Ξ, and Ω [8] shown with PHENIX results for π and p [9] reproduced from the STAR whitepaper [10].

approximately 2 GeV in a collision are predominantly the result of hard parton scatterings during the initial collision. These should therefore scale as the number of nucleon+nucleon collisions, N_{coll}, in a nuclear collision. By taking the ratio of N_{coll} normalized p_T spectra between central and peripheral events we can construct the nuclear modification factor R_{CP}:

$$R_{CP} \equiv \left(\frac{1}{\langle N_{coll}\rangle_{\mathrm{C}}} \times \frac{d^2N_{\mathrm{C}}}{dydp_T}\right) / \left(\frac{1}{\langle N_{coll}\rangle_{\mathrm{P}}} \times \frac{d^2N_{\mathrm{P}}}{dydp_T}\right) \tag{1.1}$$

where the subscripts C and P represent central and peripheral events, respectively. Central events are collisions with significant transverse overlap between the colliding nuclei while peripheral events are collisions with a small amount of transverse overlap between the nuclei. If scattered partons travel through a volume of colored medium then we would expect them to lose energy which would result in R_{CP} values less than one at high p_T due to the exponentially falling spectra.

The STAR R_{CP} results at $\sqrt{s_{NN}} = 200$ GeV are shown in Figure 1.3 and demonstrate a clear suppression at high transverse momentum. Suppression itself could also be described as a result of gluon saturation but the trend of the suppression is not consistent with this model. LHC experiments have made measurements at transverse momentum values up to 100 GeV for both R_{CP} and the related nuclear modification factor R_{AA}

$$R_{AA} \equiv \left(\frac{1}{\langle N_{coll}\rangle_{\mathrm{C}}} \times \frac{d^2N_{\mathrm{C}}}{dydp_T}\right) / \left(\frac{d^2N_{\mathrm{p+p}}}{dydp_T}\right) \tag{1.2}$$

which uses $p + p$ collisions rather than peripheral $A + A$ collisions as a reference. These results are presented in Figure 1.4. A clear suppression is seen at all values of p_T but at around 6 GeV the nuclear modification reaches a minimum and begins increasing. This is again consistent with partonic energy loss because as the power-law tail of the spectra flattens at high p_T the same amount of energy loss will result in less suppression at high p_T.

1.1.4 Enhancement of Baryons at High p_T

The production process for high transverse momentum particles is expected to be dominated by hard parton scatterings which then fragment into jets. The nonperturbative process of jet fragmentation is parameterized by fragmentation functions measured from

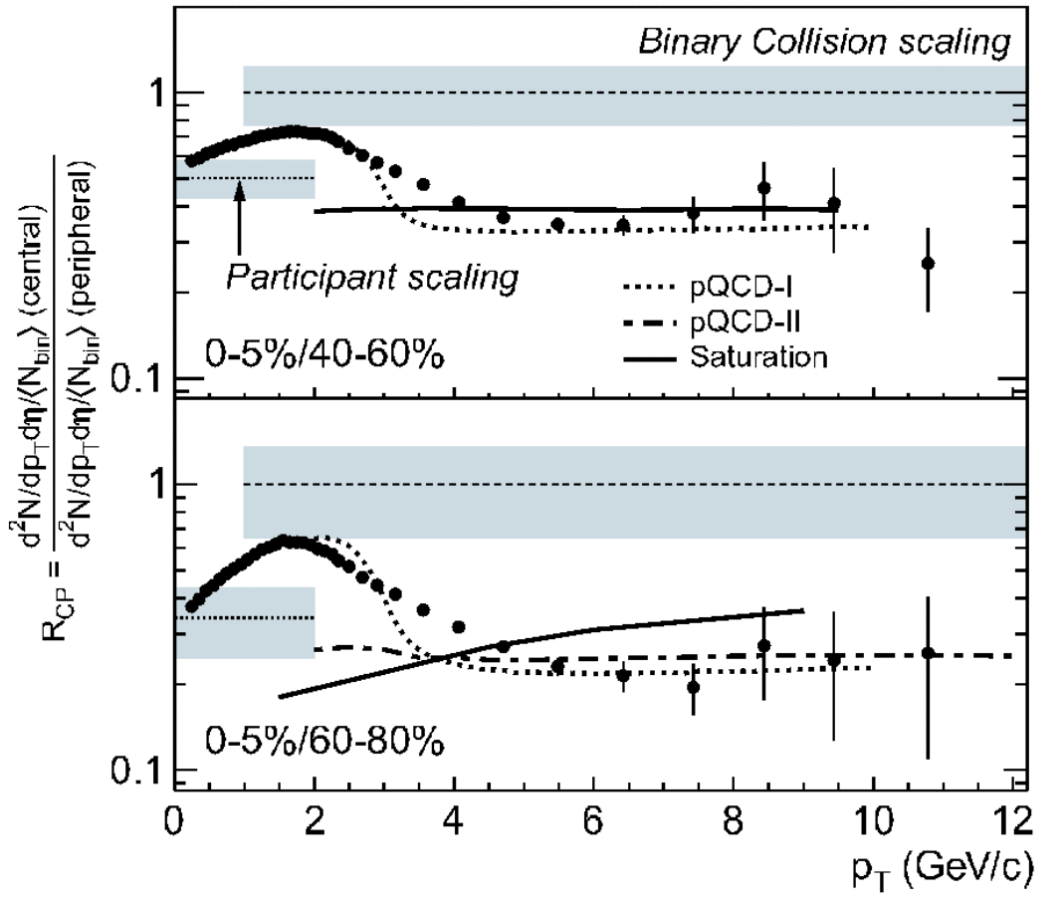

Figure 1.3: STAR Measurement of Unidentified Particle R_{CP} at $\sqrt{s_{NN}} = 200$ GeV
The ratio of central to peripheral binary collision scaled invariant yields from $\sqrt{s_{NN}} = 200$ GeV Au+Au collisions reproduced from Reference [11]. The shaded bands indicate the systematic uncertainty in the number of participants scaling at low p_T and the number of binary collisions scaling at high p_T. Both the Cronin effect and partonic energy loss are included in the pQCD-I [12] and pQCD-II [13] models which were fit to the data. The gluon saturation model does not include partonic energy loss.

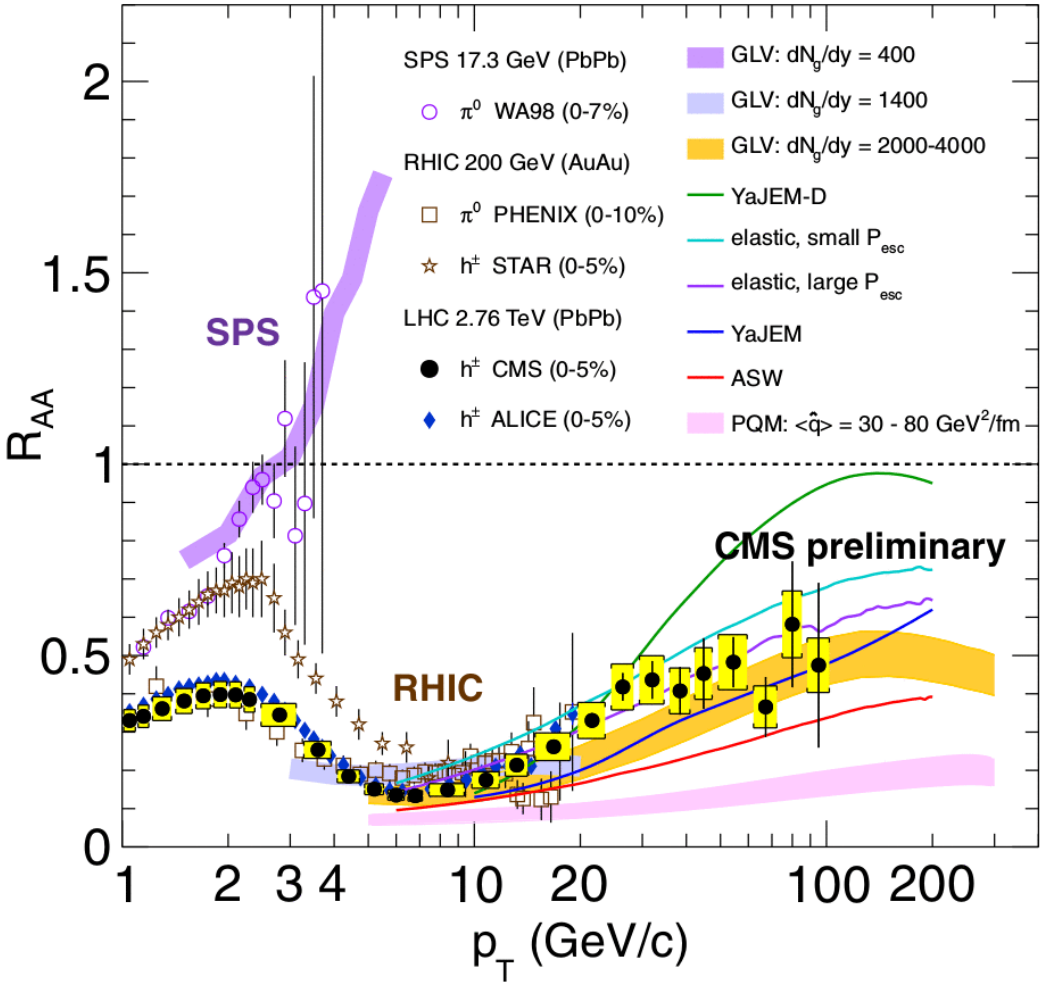

Figure 1.4: CMS R_{AA} Measurement

The ratios of binary collision scaled invariant yields in central heavy-ion collisions at center of mass energies of $\sqrt{s_{NN}}$ =17 GeV, 200 GeV, and 2.76 TeV reproduced from Reference [14]. The lines indicate various models. The error bars on the data points represent statistical uncertainties while the boxes and bands represent systematic uncertainties.

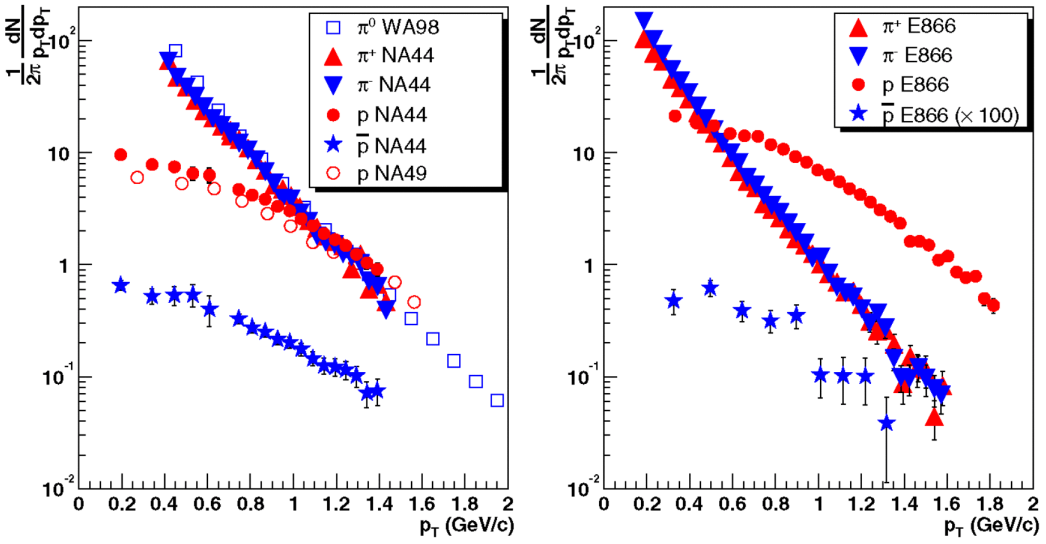

Figure 1.5: Production of p and π at the SPS and AGS

Invariant p and π yields at mid-rapidity for central collisions of Pb+Pb with $\sqrt{s_{NN}} = 17$ GeV at the SPS in the left panel and of Au+Au with $\sqrt{s_{NN}} = 5$ GeV at the Alternating Gradient Synchrotron (AGS) in the right panel as it appeared in the PHENIX whitepaper [18]. The data comes from the experiments E866 [19, 20], NA44 [21], NA49 [22], and WA98 [23].

data which, if collinear factorization holds, should be universally applicable. Baryons have repeatedly been observed to be suppressed in fragmentation relative to mesons [15, 16]. This can be phenomenologically explained by the increased energy cost of producing a diquark-antidiquark pair to lead to the formation of a baryon relative to the cost of producing a quark-antiquark pair to produce a meson [17]. If fragmentation were to occur in an environment rich with free quarks then baryon formation could potentially proceed from a single quark-antiquark pair production.

Although baryon enhancement was observed in lower energy collisions at the SPS and AGS, this was in the soft region where $p_T \leq 2$ GeV and was unique to the positively charged particles as illustrated by Figure 1.5. This can be simply understood as a result of increased baryon stopping in central collisions at these energies, whereas a modification in fragmentation should extend to high p_T and affect proton and antiproton yields similarly.

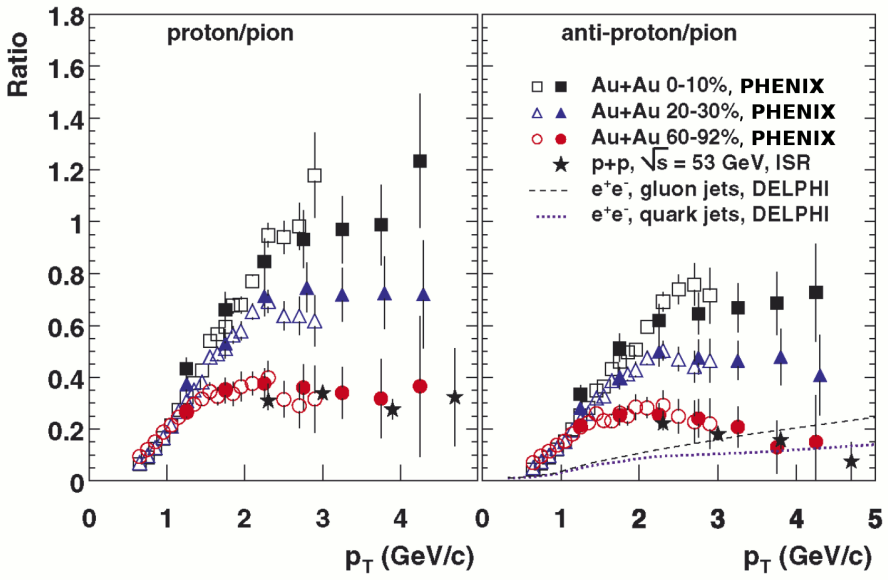

Figure 1.6: p/π Enhancement in Central Au+Au Events

PHENIX p/π ratios for various centralities in Au+Au collisions at $\sqrt{s_{NN}} = 200$ GeV as it appeared in Reference [24]. Open points represent $\pi^{+/-}$ while closed points signify π^0. Intersecting Storage Rings (ISR) data from p+p collisions are shown with stars while Detector with Lepton, Photon, and Hadron Identification (DELPHI) measurements of $(\bar{p}+p)/(\pi^+ + \pi^-)$ ratios in quark and gluon jets at Large Electron-Positron Collider (LEP) are denoted by the dashed lines [15, 16].

At RHIC, this modification in fragmentation has been primarily studied by PHENIX [18]. They constructed the ratios between proton and pion p_T spectra for different centrality classes producing the results shown in Figure 1.6. The ratios above $p_T = 2$ GeV are more than twice as large in central collisions than they are in peripheral and p+p collisions. This behavior is exhibited in both protons and antiprotons, although it does appear that the ratios are slightly larger for protons.

An alternative explanation for this enhancement is radial flow, which would boost the momentum of protons and antiprotons more significantly than the much lighter pions. This effect was ruled out as a full explanation by radial flow limits imposed by hydrodynamic fits to flow and spectra [18]. In light of this, the baryon enhancement remains a compelling piece of evidence for modification of jet fragmentation. This could also be the result of cold nuclear matter effects but is also consistent with a QGP description.

1.1.5 Conclusions

The general tone of the white papers was one of hesitancy in drawing conclusions about QGP formation. It was generally accepted that a number of observables were not consistent with a hadronic picture of the collision but not a single experiment was willing to claim conclusive evidence for QGP formation. It had been expected that a QGP would be weakly interacting but the produced medium appeared to interact strongly. Many people were also expecting divergent fluctuations and strong discontinuities in observables but everything evolved smoothly as a function of collision energy, centrality, and rapidity. The fact that these expectations were not met led to an overall feeling that a state of matter with partonic degrees of freedom was formed but that it was not necessarily the QGP state.

1.2 Current Perspective

In the early years of RHIC there was significant disagreement within the theory community over whether a first order phase transition should be expected at a baryon chemical potential, μ_b, of zero. In figure 1.7, which was reproduced from a 2002 lattice QCD paper

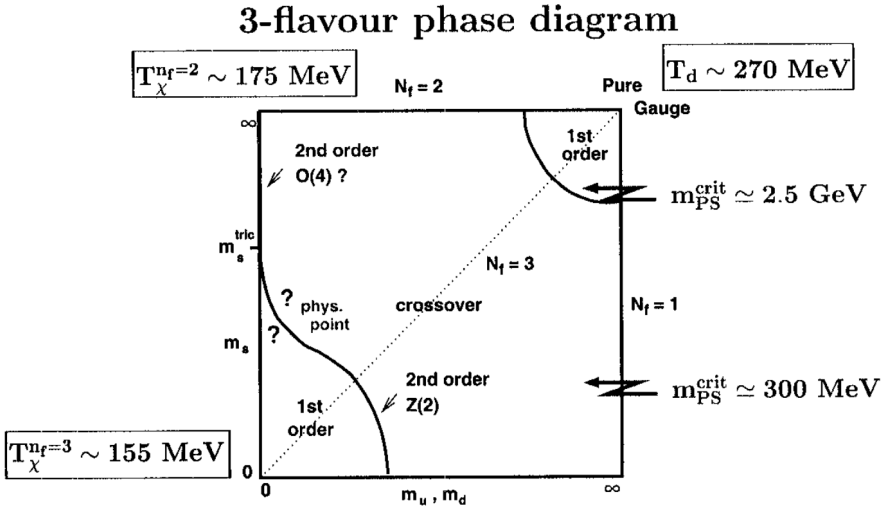

Figure 1.7: The QCD phase diagram of 3-flavor QCD

QCD phase diagram with degenerate (u,d)-quark masses and a strange quark mass of m_s reproduced from Reference [2].

[2], you can see question marks floating around the physical point indicating the uncertainty over whether it falls within the region of a first order phase transition. In light of this, it's understandable that the experiments would worry somewhat about the lack of evidence for a first order phase transition. The theory landscape has, however, changed significantly in the interim.

Lattice QCD calculations have, in general, matured significantly in the decade since the RHIC whitepapers were published. This has been partly due to improvements in discretization schemes (actions) which have reduced discrepancies between research groups. It is also the result of the staggering growth in available computing resources [25]. For a sense of scale, one group in Frankfurt recently reported that their lattice calculations ran at 60 gigaflops on a consumer level graphics card [26]. This inexpensive desktop machine would have outperformed a number of the top 500 supercomputers in the world when RHIC began operating [27].

With these vast improvements in lattice QCD calculations has a come a much more refined view of the QCD phase diagram. The phase transition at $\mu_b = 0$ with physical values for the quark masses has been clearly shown to be a crossover through multiple

independent approaches [28]. It has been shown directly to be non-critical and analytic in the continuum limit [29] and through the explicit mapping out of the chiral critical line (though with course lattice sizes) [30]. In light of this, it should be no surprise that no discontinuities in observables were observed at RHIC or the LHC. Our understanding of the phase as being strongly interacting has also grown considerably and so the fact that this has been observed is no longer considered surprising [31].

Our understanding of the relationship between Au+Au collisions and theory calculations has also grown considerably, particularly with respect to fluctuations. The impact of effects such as limited centrality resolution and reconstruction efficiency have become analytically understood while charge conservation, limited acceptance, lack of non-local thermal equilibrium, and fluctuations in energy deposition and the geometry of initial conditions recognized as extremely significant factors. Overall, we've learned that fluctuation analyses have little to no relationship with thermodynamic susceptibilities and are instead an extremely complicated convolution of these effects. Any expectation for divergences in fluctuation observables were, and continue to be, at least partially misguided.

As perspectives have developed the overall perception has shifted towards a full acceptance that a QGP is formed in nuclear collisions and at RHIC. This was initially qualified as a strongly interacting QGP (sQGP) but in common usage QGP is now often used to refer to a sQGP. There are still many open questions surrounding the nature of the QGP but it's formation is generally agreed upon and many of the initial expectations are now seen as being overly idealistic.

1.3 The STAR Beam Energy Scan

Even with the widespread acceptance of the formation of a QGP there is still a lack of indisputable evidence demonstrating it beyond the shadow of a doubt. The evidence that could fulfill this role of smoking gun most easily is the same one that people were hoping to find at RHIC top energy: clear signs of a first order phase transition. With the establishment that the transition would be a crossover when $\mu_B \approx 0$ it became clear that the transition would need to be probed at higher values of μ_B in order to find evidence of either a first order phase transition or a critical point marking the boundary between

the first order and crossover phase transitions. This could be accomplished by running experiments at lower center of mass energies where baryon stopping plays a larger role in the thermodynamics of the collision as illustrated in Figure 1.8.

A proposal was drafted by STAR to run a BES of lower collision energies at RHIC in order to search for evidence of a first order phase transition, evidence of a critical point, and for the turn off of QGP signatures [32]. The proposed BES would revisit the SPS energy regime and fill in the gaps between this and the RHIC top energy. RHIC had already done some test runs at lower energies but the BES would produce much higher statistics, allowing for analyses that were not possible with the test data. The proposal was accepted and the scan carried out during 2010 and 2011. The analysis outlined in this thesis aims to revisit, at BES energies, several of the key QGP signatures observed at $\sqrt{s_{NN}} = 200$ GeV in order to address the primary BES goal of identifying the turn off of QGP signatures.

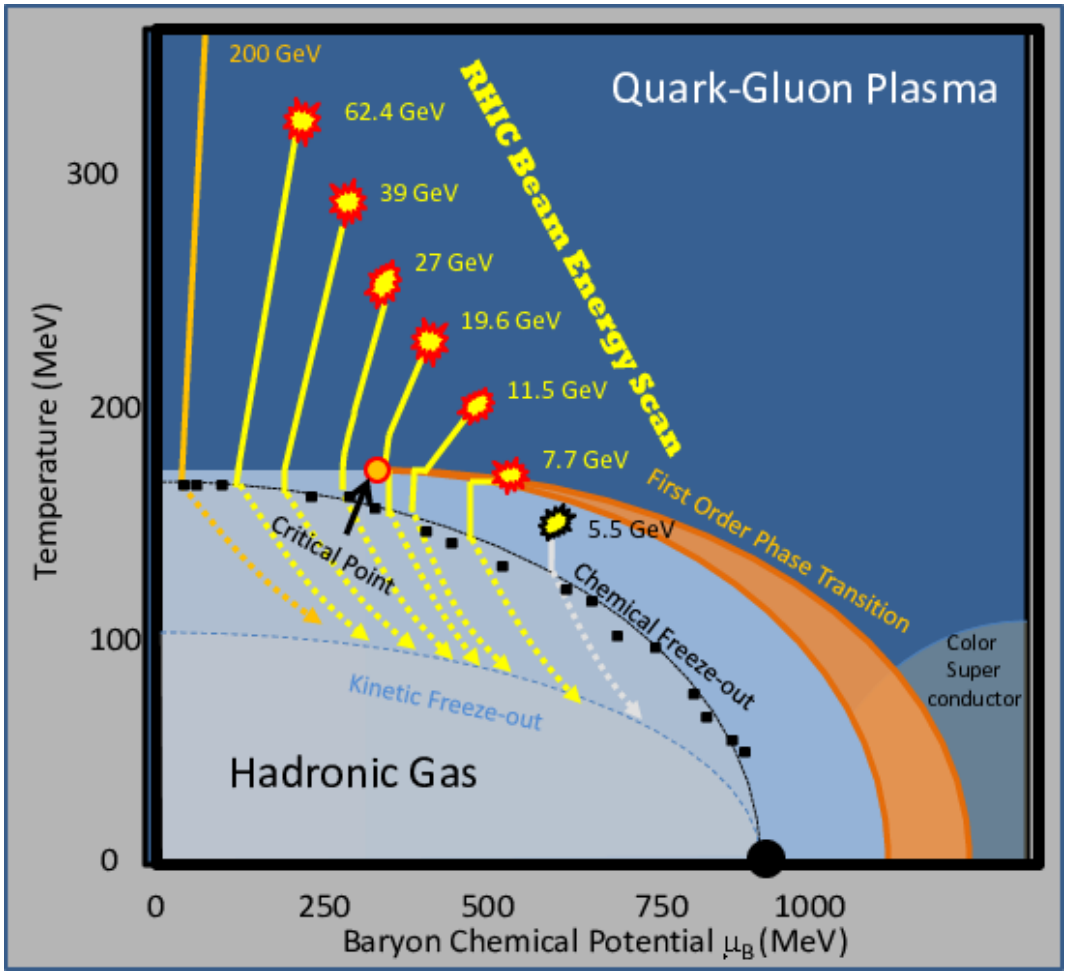

Figure 1.8: The QCD phase diagram

The possible evolution of collisions through the phase diagram for RHIC top energy, the 6 BES energies, and an additional energy of $\sqrt{s_{NN}} = 5.5$ GeV that was never run. This figure was obtained through private communication with Daniel Cebra.

Chapter 2

Experimental Setup

2.1 The Relativistic Heavy Ion Collider

The datasets used in this analysis were produced at RHIC which is located at BNL. Brookhaven was originally founded as nuclear research facility in 1946 on the former US Army training base, Camp Upton, on Long Island, New York. Despite the fact that converting a military training base into a nuclear research facility in 1946 may appear less than serendipitous, the lab actually houses an active nonproliferation department and is focused on pure science rather than programmatic work. Since its inception the lab has in fact grown into a multidisciplinary research facility with work being done in chemistry, neuroscience, environmental science, biology, and of course physics. In addition to RHIC and its assorted components, BNL also houses Center for Functional Nanomaterials (CFN), National Synchrotron Light Source (NSLS), the upcoming NSLS-II, National Nuclear Data Center (NNDC), and RHIC Computing Facility (RCF) which are all world-class facilities. Research performed at the lab has led to four Physics and two Chemistry Nobel Prizes while the lab is also credited as the birthplace of electronic table tennis or, as it is more commonly known, Pong.

The layout of the RHIC facility can be seen in Figure 2.1. It is a symmetric collider and was the first of its kind in heavy-ion physics. The fact that it is a collider allows it to achieve much higher collision energies than a comparable synchrotron fixed-target experiment would be able to. The SPS, for example, has a circumference of 6.9 km and

$\sqrt{s_{NN}}$ (GeV)	p_{lab} (GeV)		p_{lab} ratio (fixed/collider)
	symmetric collider	fixed-target	
7.7	3.7	30.6	8.2
11.5	5.7	69.5	12.2
19.6	9.8	203	20.9
27.0	13.5	387	28.8
39.0	19.5	809	41.5
62.4	31.2	2072	66.5
200.0	100	21315	213

Table 2.1: Momentum per nucleon in fixed-target and collider experiments

a top energy of $\sqrt{s_{NN}}$=17.3 GeV for heavy ion collisions while RHIC has a circumference of 3.8 km and a top heavy-ion energy of $\sqrt{s_{NN}}$=200.0 GeV. Table 2.1 gives a comparison of the lab momentum that would be required to achieve a $\sqrt{s_{NN}}$ equal to each of the BES energies as well as RHIC top energy. The magnetic field required for a synchrotron scales linearly with the lab momentum so the field strength will scale roughly linearly with respect to center of mass energy for a collider and quadratically for a fixed target experiment. This not only allowed for RHIC to produce much higher collision energies than previous facilities but also allows it to operate over a much wider range of collision energies, a fact that is extremely relevant to the analysis at hand. The collision energy range of RHIC requires the magnets to operate at magnetic fields varying by factors of 1-27 while a fixed target accelerator would require the magnets to operate precisely over a range of 1-697.

2.1.1 The Acceleration Process

Before acceleration may begin the gold atoms must be ionized. This is done using a cesium sputter ion source which gives the atoms a -1 charge state and allows them to be accelerated to the terminal of the tandem Van de Graff where the beam passes through a carbon stripper foil which brings the ions to a +12 charge state. This switch from

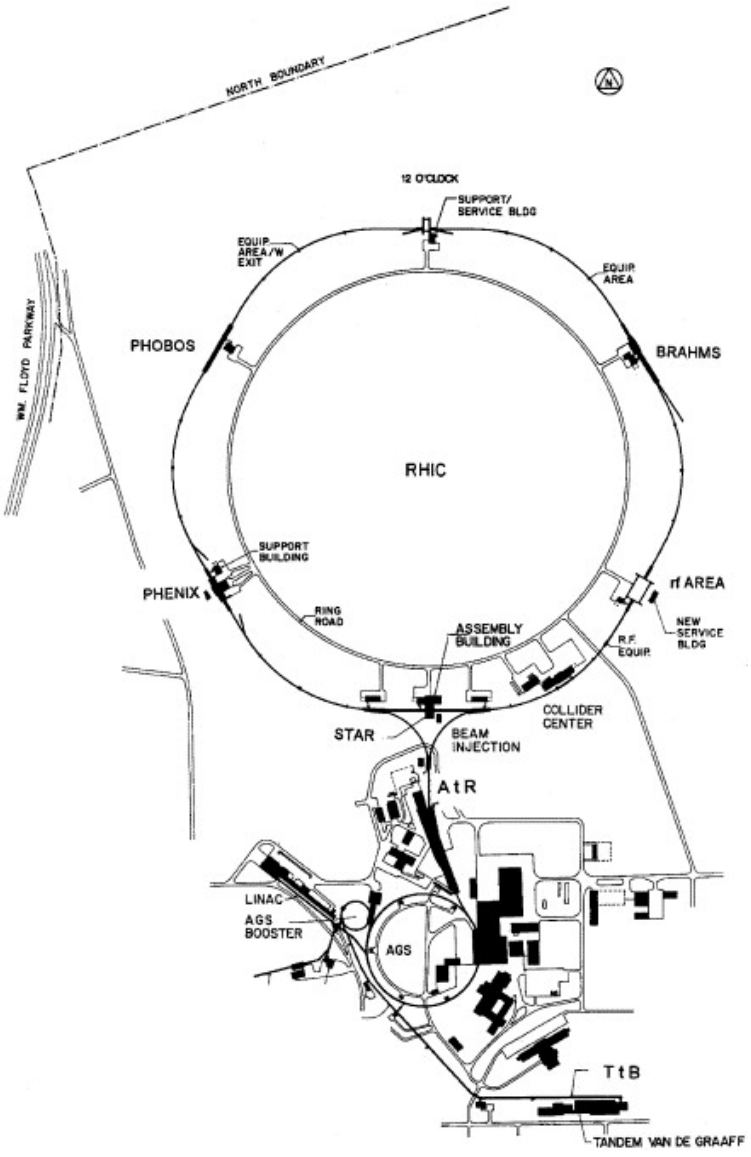

Figure 2.1: RHIC collider layout

The layout of the RHIC complex which shows the locations of each experiment and the components of the accelerator reproduced from Reference [33].

negatively to positively charged allows for the ions to be accelerated back in the opposite direction using the same electric field. When they reach the opposite terminal of the tandem they pass through an object stripper foil which brings them to a +32 charge. At this point the beams have a momentum of roughly 1 MeV per nucleon and are ready to be transferred to the Booster via the Tandem-To-Booster (TTB)[34].

The Booster is a synchrotron accelerator with a radius of 201.8 meters. It accelerates the beams until they reach 72 MeV per nucleon at which point they exit, pass through another stripper which brings them to a charge state of +77, and finally enter the AGS though the Booster-To-AGS (BTA) line. The AGS is another synchrotron accelerator with a radius four times larger than that of the booster. The AGS employs alternating gradient focusing in which the magnetic field gradient ($\partial B/\partial r$) alternates around the ring for the purpose of focusing [35]. When the beam leaves the AGS it has a momentum of 9.8 GeV per nucleon, at which point it is stripped of its final two electrons and injected into the main accelerator [36].

The main accelerator is comprised of two rings which are named Blue (clockwise) and Yellow (counter clockwise). It has a radius that is 19/4 times that of the AGS and is capable of accelerating the beams up to 100 GeV per nucleon or storing them below the standard injection energy as was done during the BES. The technical details of the accelerator are innumerable and not of particular relevance to the analysis at hand. In light of this we will refrain from going into finer details and instead point the interested reader to the wealth of literature available on topics such as the beam instrumentation [37], vacuum system [38], control system [39], personal safety system [40], magnet system [41, 42], cryogenics [43], or RHIC in general [33, 44].

2.1.2 The RHIC Experiments

Before focusing in on STAR we should briefly mention the other experiments on the RHIC ring. There are six Interaction Region (IR)s on the RHIC ring where the Blue and Yellow beams cross and can be steered for collisions. One IR houses the RHIC Radio Frequency (RF) system, another has remained unused, and the four others house the BRAHMS, PHOBOS, PHENIX, and STAR experiments [45]. The locations of these

experiments are shown in Figure 2.1. BRAHMS was designed for momentum spectroscopy to study small x saturation physics and completed its goals in 2006 [46]. PHOBOS had the largest pseudorapidity coverage of the experiments and was particularly well suited for measuring multiplicity distributions out to high rapidity and ceased operation in 2005 [47]. PHENIX was designed primarily for the detection of rare hard probes such as electrons, muons, and direct photons [48]. Finally, STAR is a general purpose hadronic detector with a large solid angle covered at midrapidity [49].

2.2 The STAR Detector

A few general comments about STAR should be made first before addressing specific detector systems. First, the coordinate system is defined such that the beam is parallel to the z axis and the $x-z$ plane is parallel to the surface of the earth. Spherical coordinates are then defined such that ϕ gives the azimuthal angle around the z axis and θ is the polar angle. Also, a solenoidal magnet surrounds STAR with an axial magnetic field of 0.5 T which is parallel to the beam line. This magnet results in curvature of charged particle trajectories which can be used to make momentum measurements.

The STAR experiment is made up of a large number of detector subsystems. Many of these detectors serve specific purposes that are only relevant to specific types of analyses. The Muon Telescope Detector (MTD) is, for example, designed specifically to detect decay muons from quarkonia [50] and the Forward GEM Tracker (FGT) serves the even more specific purpose of identifying the charge of W bosons decay to leptons [51]. These detectors and many others at STAR are amazing technical achievements that are used to produce interesting physics results, but they are not used in the analysis that is the topic of this thesis and as such they will not be discussed further. Instead, we will focus on the detectors which are of fundamental importance to this analysis.

2.2.1 The Time Projection Chamber

The Time Projection Chamber (TPC) is undoubtedly the heart of the STAR experiment. It forms a cylinder around the beam pipe with dimensions of 4.2 m in length and

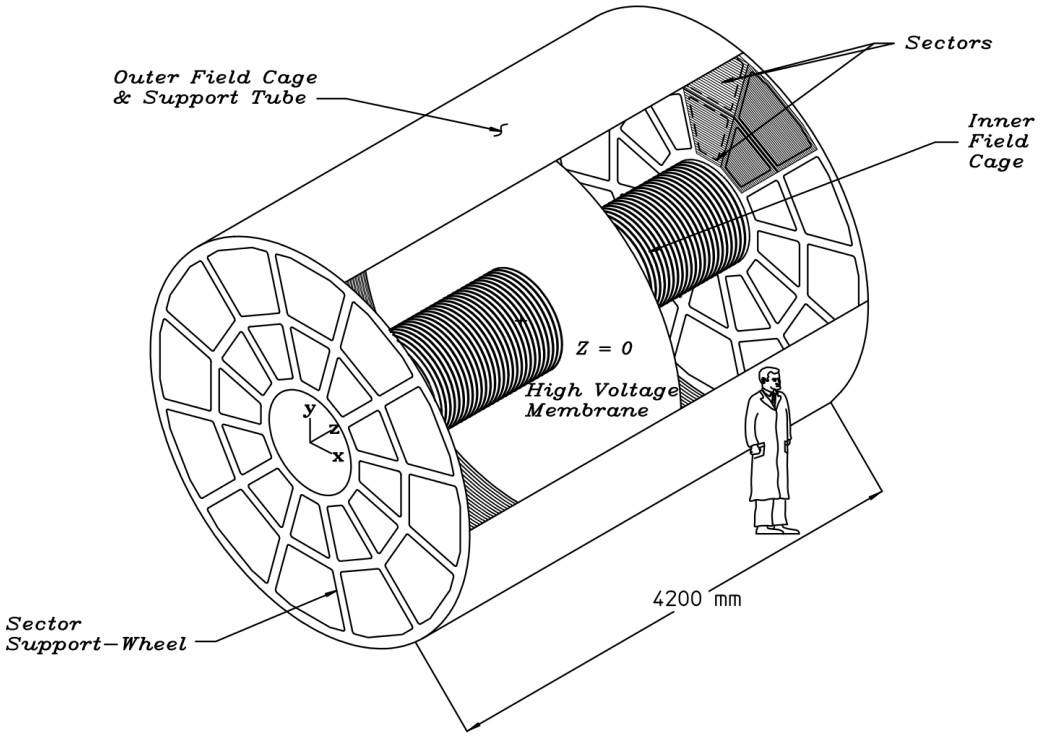

Figure 2.2: The STAR TPC geometry

An illustration of the STAR TPC geometry showing the locations of the sectors, the central membrane, and the inner field cage reproduced from Reference [52].

4 m in diameter, affording it a full 2π azimuthal acceptance and a pseudorapidity extent of roughly ± 1.8 units. It is under normal circumstances the only detector necessary for track reconstruction near mid-rapidity and additionally gives ionization energy loss (dE/dx) measurements that are one of the primary methods of particle identification at STAR. The design of the TPC can be seen in Figure 2.2.

The endcaps of the TPC are grounded and it is divided in the middle by a high voltage membrane operated at -28 kV which results in an axial electric field of roughly 135 V/cm. The Inner Field Cage (IFC) is comprised of a series of conductive rings separated by precision resistors to ensure that the field remains uniform. The volume is filled with p10 gas (10% methane, 90% argon) which is ionized when charged particles pass through it [53]. The freed electrons then drift towards the nearest endcap at a rate of 5.45 cm/μs, a velocity that is calibrated through the use of lasers to ionize the gas [54]. The gas and

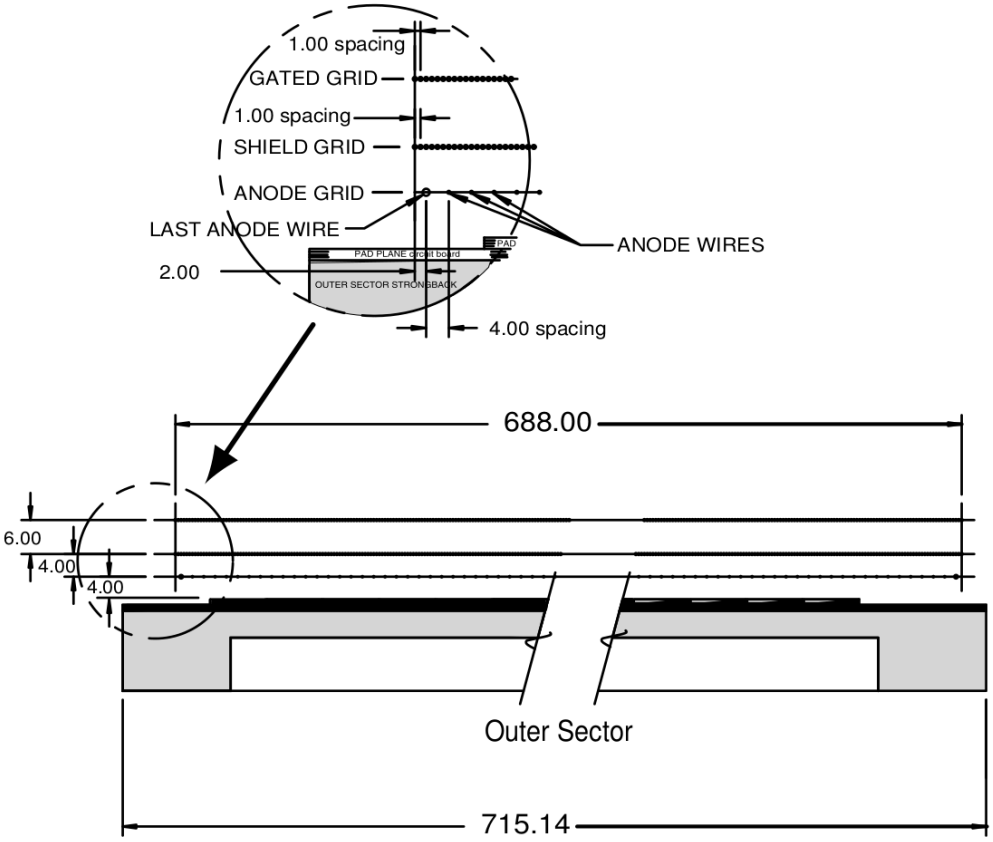

Figure 2.3: TPC grid configuration

Configuration of the gating, ground, and anode grid with respect to the pad plane for an outer sector of the TPC reproduced from Reference [52].

electric field strength were chosen to maximize this drift rate so that it would change as little as possible in response to pressure and temperature variations. The uniform electric field coupled with the 0.5 T field of the STAR magnet allow for very little transverse drift during this process.

When electrons reach the end of the TPC they can be read out using Multi-Wire Proportional Chambers (MWPCs). The MWPC at each end of the TPC consists of a fine wire anode grid, ground grid, gating grid, and a readout pad plane made up of 12 sectors. The grids are made up of many small parallel wires and serve three distinct purposes.

The gating grid acts as a shutter to control the entry of electrons from the TPC volume

and to prevent positive ions in the MWPC from drifting towards the central membrane and distorting the field. When its voltage is brought to -110 V it is essentially transparent to drifting ions. When the voltage on neighboring wires is shifted ± 75 V from the nominal value then ions will be drawn to the grid wires and the gate closes. It is only opened when an event is triggered to be read out [55].

Spaced 6 mm beyond the gating grid is the ground grid which serves to terminate the drift field and to act as RF shielding for the readout pads. Once electrons have reached the ground shield grid they are drawn to the anode grid which is located 4 mm away and held at 1170 V for the inner subsectors and 1390 V for the outer subsectors. Because the electric field around the anode wires grows as $1/r$, the electrons accelerate rapidly and cause an avalanche of other electrons as they move towards the anodes. This process amplifies the signal by a constant factor on the order of 1000-3000.

The electron avalanches leave clusters of positive ions which will disperse towards the central membrane but because they are so massive they do this at a slow rate compared to the electrons and will not be able to escape before the gating grid is closed. The electric fields created by these positive charges are what the readout pads actually detect from 2 mm away in the inner subsectors and 4 mm in the outer. Multiple adjacent pads pick up the field from a single avalanche and as a result the overall hit resolution is smaller than the size of a single pad.

The layout of the readout pads for one sector can be seen in Figure 2.4. There are 45 pad rows in each sector and a total of 5692 pads. This allows a typical charged particle to leave up to 45 hits in the detector, although this number can be larger for low momentum tracks. Each hit has associated (x, y) coordinates that come from the location of the hit on the endcap and a z coordinate that is a projection based on the timing of the hit and the known drift velocity. It additionally carries a measure of the ionization that is proportional to the rate of energy loss for the track.

The collection of TPC hits that are collected on a triggered event are then reconstructed into tracks using an algorithm based on Kalman filtering. The radii of the resulting helical tracks gives their momenta and their handedness gives their charges. The average of the ionization between all of the hits in a track would give a measure of its energy loss but a procedure is followed by which the largest 30% of ionization mea-

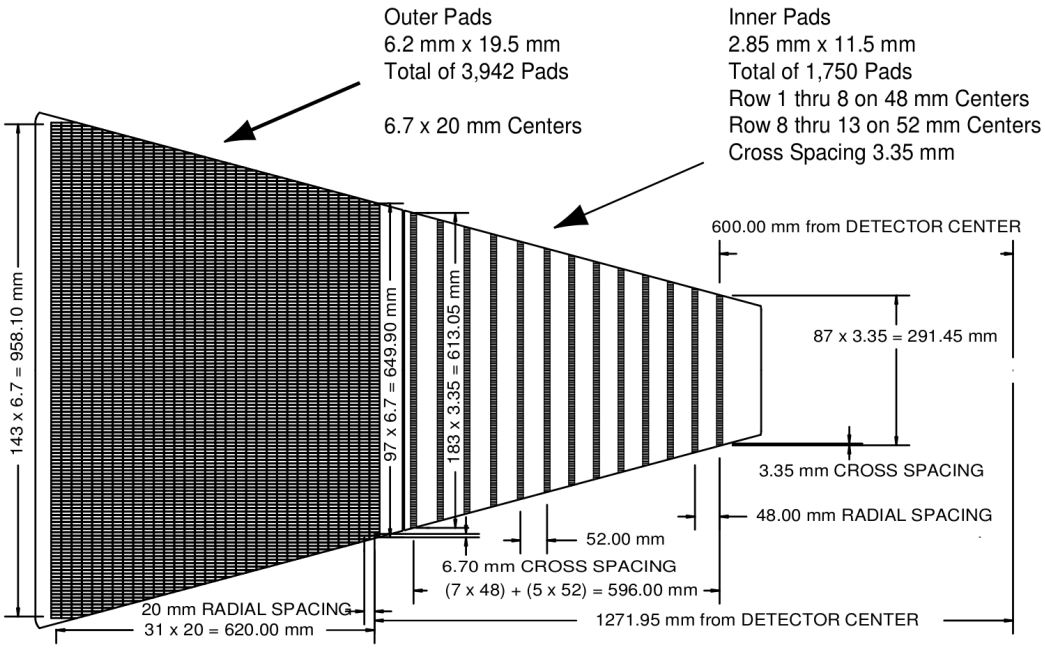

Figure 2.4: Anode pad plane of the STAR TPC

The readout pad plane for one sector of the STAR TPC reproduced from Reference [52]. The outer sector is shown on the left and has no spacing between pads while the inner sector is on the right and made up of pad rows that are widely spaced.

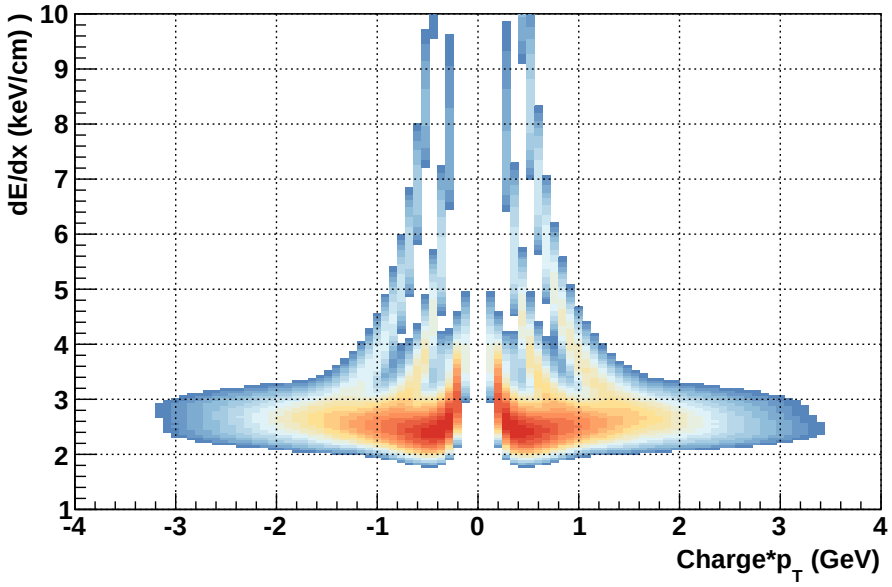

Figure 2.5: dE/dx vs rigidity in $\sqrt{s_{NN}}$=62.4 GeV collisions

surements for each track are rejected before this averaging takes place. This is done to truncate the high tail of the roughly Landau distribution for ionization and results in more symmetric $^{dE}/_{dx}$ distributions.

The charge, momentum, and $^{dE}/_{dx}$ measurements obtained from the TPC form the core set of data used in this analysis. Figure 2.5 demonstrates how this information can be used for particle identification but also illustrates how the $^{dE}/_{dx}$ values for different particle species are not easily distinguishable above $p_T = 1.5$ GeV. This limitation necessitates the use of the Time-of-Flight (TOF) at high transverse momentum to gain additional information about the identity of the tracks.

2.2.2 The Time of Flight Detector

The TOF system is a cylindrical detector immediately surrounding the TPC. The technology at the core of the TOF is that of the Multigap Resistive Plate Chamber (MRPC). Each MRPC covers an area of about 10 cm by 20 cm and consists of 0.54 mm

thick stacked resistive plates separated by six gaps of 220 μm. A 14 kV voltage difference is applied across graphite electrodes attached to the outer surface of 1.1 mm thick outer glass plates. These gaps are filled with a gas made up of approximately 95% R-134a and 5% isobutane which is ionized when charged particles pass through it. This ionization, in the presence of a strong electric field, results in avalanches of electrons. The resistivity of the glass plates prevents the propagation of streamers, or sharp ionization waves, while simultaneously allowing the electric fields caused by the avalanches to be picked up by the 6 copper pickup pads which are isolated from the outer electrodes by mylar [56].

The signals read by the pickups are converted to digital timing measurements with a resolution of about 100 ps. These TOF hits are associated with TPC tracks which provides both a path length and a momentum measurement for the corresponding particles. If the time of the collision is known then we can calculate $1/\beta = \Delta t/L_{\text{path}}$ which is related to the mass of the particle through $m = p\sqrt{1/\beta^2 - 1}$. Historically, STAR has used the Upgraded Pseudo Vertex Position Detector (upVPD) (or one of its related incarnations) to obtain start time information [57]. This consists of two identical scintillator detectors located close to the beam pipe outside of the STAR magnet. They detect extremely forward high energy photons from the Au+Au collisions and are able to measure the collision time with a resolution on order of 20 ps. It was found that reliable upVPD signals were not obtained at collision energies below $\sqrt{s_{NN}} = 39.0$ GeV and so an alternative start-less TOF algorithm was employed. The approach assumes that any track with 0.2 GeV $< p_T <$ 0.6 GeV and within two standard deviations of the expected pion dE/dx value is indeed a pion. It then averages the estimates of the start time for each of these tracks based on the mass, momentum, and track length. This procedure has been shown to produce results that are consistent with those obtained with the upVPD.

The MRPCs are arranged in 120 trays, each covering roughly one unit of pseudorapidity and $\pi/30$ of azimuthal angle. The arrangement within a single tray can be seen in Figure 2.6. The final configuration gives full 2π coverage for $|\eta| < 0.9$ which includes the entire kinematic region used in this analysis [59]. Measurements of $1/\beta$ as a function of rigidity can be seen in Figure 2.7. Clear separation of the different particle species can be seen to extend out to much higher momentum values than are possible with the TPC dE/dx measurements. Additionally, measurements from the two detectors are highly

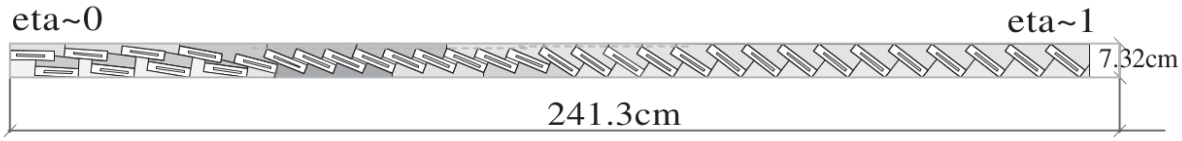

Figure 2.6: Layout of MRPCs in a single TOF tray

The arrangement of 32 MRPCs in a TOF tray reproduced from [58]. The MRPCs are slanted to remain perpendicular to tracks coming from collisions in the center of the detector.

complementary at high transverse momentum where kaons and protons are difficult to distinguish in $^{dE}/_{dx}$ while kaons and pions are difficult to distinguish in $^{1}/_{\beta}$. By combining information from both detectors when analyzing data we will be able to remove the ambiguity that exists in measurements from a single detector.

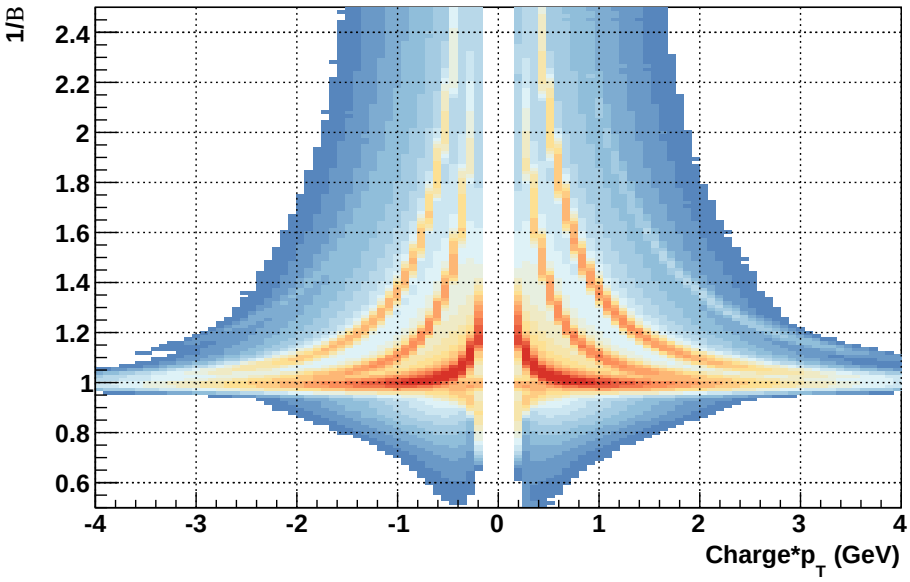

Figure 2.7: $1/\beta$ vs rigidity in $\sqrt{s_{NN}}$=62.4 GeV collisions

Chapter 3

Datasets and Quality Assurance

3.1 Datasets

The data used in this analysis was recorded as part of the RHIC BES during the years 2010 and 2011. Four of the center of mass collision energies, 7.7, 11.5, 39.0, and 62.4 GeV, were run during 2010 while 19.6 and 27.0 GeV were run during 2011. This distinction is worth noting as the acceptance and performance of the detectors does change from year to year as components become damaged or repaired. These differences in acceptance between years, and additionally within each individual year, are carefully corrected for and the final results are not believed to be influenced by them in any way. The details of these corrections will be discussed in depth in Chapter 6.

The raw detector data were processed into individual tracks with spatial, momentum, $1/\beta$, dE/dx, and various other information as was described in the detector overviews in Subsections 2.2.1 and 2.2.2. Tracks sharing a common point in time and space were associated with the point as a vertex and grouped together as a single event collision. The resulting number of events at each collision energy are listed in Table 3.1. The processing of the data into these physical abstractions was done at a collaboration level within the STAR experiment and the datasets that were used directly in this analysis already included the abstractions.

Collision Energy (GeV)	Number of Minimum Bias Events (million)
7.7	12.7
11.5	21.5
19.6	48.6
27.0	95.4
39.0	170.6
62.4	120.4

Table 3.1: Event numbers at each collision energy

The number of minimum bias events recorded at each collision energy before the application of quality cuts which constrain quantities such as the vertex location.

3.2 Triggering

When the collider is running, decisions need to be made very quickly about when to read out data from the detectors and write it to disk. This process of decision making is called triggering and at STAR it is broken up into four stages with distinct time scales: Level 0 (L0), Level 1 (L1), Level 2 (L2), and Level 3 (L3) [60, 61]. Each time that there is a bunch crossing of gold nuclei in the STAR IR, which is roughly once every 107 ns, there is the possibility of one or more Au+Au collisions occurring. The trigger system is synchronized with the RHIC clock and at these crossings the L0 trigger must determine within 1.5 μs whether the detectors are ready to accept a new event and whether there is any evidence that a collision has actually happened. The L1 and L2 triggers then have larger windows of respectively 100 μs and 5 ms to make more detailed evaluations.

These early triggering stages rely primarily around output from fast detectors such as the Zero Degree Calorimeters (ZDCs) [62], Beam-Beam Counters (BBCs) [63], Barrel Electro-Magnetic Calorimeter (BEMC) [64], and Central Trigger Barrel (CTB) [60]. This detector output has time to undergo only very basic processing and often involves Boolean logic applied to thresholds on summed signals. The L3 trigger, on the other hand, performs track and event reconstruction on the 1000 events that are read out each second, allowing it to incorporate basic cuts on particle identification and momentum correlations before

writing events to disk [61].

The goal of the BES trigger configurations was primarily to record minimum bias data that accurately reflects the underlying crosssections for Au+Au collisions. The exact configuration varied but the settings were chosen to accomplish this goal at each energy. The trigger had to be far less selective than it would need to be at top RHIC energy due to the significantly lower luminosity that was achieved during the BES and because of this the logic did not need to be as sophisticated. Additionally, the lower collision energies led to far noisier signals in the forward trigger detectors due to how the projectiles fragmented. Almost any signal in the detectors would lead to an event trigger at these energies. As a result of this, there are wide vertex distributions along the z axis and relatively high background event rates.

3.3 Bad Run Rejection

The datasets are divided into runs which correspond to periods of continuous data taking. Each has a duration on the order of 30 minutes. The conditions of the experiment vary over time and if possible we would like to identify time periods where the conditions were not ideal and then exclude them from the analysis. One example of non-ideal conditions would be an unusually high rate of background caused by poor focusing of the beams at RHIC. Another example would be a situation where one of the detectors was not functioning correctly so the tracking or Particle Identification (PID) data was biased in some odd way.

The way that we can approach the problem of identifying runs with issues is to look at the average of various quantities within each run. If part of the TPC wasn't functioning properly during a run then we will see a lower number of tracks in events during that run. If there was an unusually high amount of background then we will see higher vertex Distance of Closest Approaches (DCAs) due to the lower quality tracking.

We studied the run averages of a variety of event and track quantities and chose a set of each that appeared sensitive to the type of conditions that we're trying to eliminate. For events the quantities looked at were the number of tracks, the quality ranking the vertex, and the z coordinate of the vertex. For tracks they were the number of dE/dx

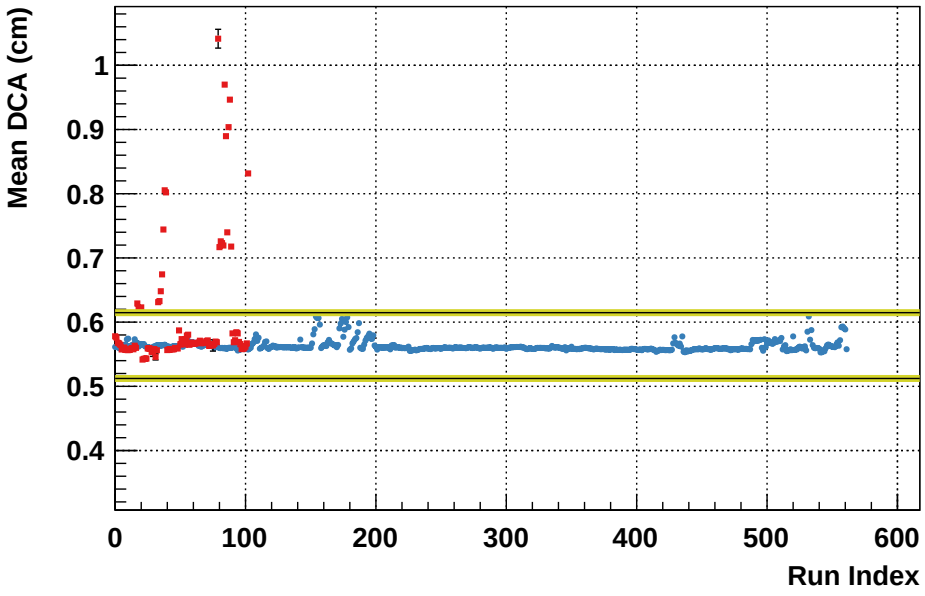

Figure 3.1: Bad run exclusion based on DCA at $\sqrt{s_{NN}}$ =62.4 GeV

An example of bad run exclusion cuts being applied on DCA. The red points indicate runs that were tagged as problematic while the blue points indicate runs deemed acceptable. The green lines indicate the five sigma cut, outside of which any run would be considered bad. A number of bad runs appear within five sigmas of the mean DCA; these were identified as bad runs by similar cuts on other track and event quantities.

points, the fraction of TPC hits fit to a track over the number of possible TPC hits for the track, the pseudorapidity, the transverse momentum, and the vertex DCA.

The mean and standard deviation of each averaged quantity was calculated for all of the runs in a given energy. Anything outside of five sigmas from the mean was marked as a bad run and the process was repeated several times to eliminate the initial inflation of the standard deviations caused by extreme outliers. A typical example showing how these cuts were applied can be seen in Figure 3.1.

The run index in Figure 3.1 is chronologically assigned and so it is apparent that the majority of bad runs occurred in the earlier period of running at 62.4 GeV. This was also the case for the other energies and it is because each new collision energy required a new configuration of the collider. As the accelerator physicists gained experience working with a new energy, the performance improved and the frequency of bad runs dropped.

3.4 Event Selection

After the elimination of bad runs it is important to also remove as many problematic events as possible. Our event cuts are relatively simple and designed for several distinct purposes. The event cuts for collisions at $\sqrt{s_{NN}}$ =7.7 GeV are listed in Table 3.2. The only difference for other collision energies is that the location of the beam spot changes for each energy.

There is the possibility for collisions of gold or secondary fragments with either the beam pipe or residual gas in the vacuum. These will tend to have reconstructed vertices that are offset from the location of the beam and can be largely eliminated by placing a tight 1 cm cut around the beam spot, as shown in Figure 3.2.

Another class that we would like to exclude are pileup events from successive bunch crossings. Tracks in pileup events can be reconstructed in the TPC but will not have valid TOF information. We can exclude these by requiring each event to have greater than two valid TOF matches. It should be noted that this cut has a significant impact on the trigger efficiency for peripheral events because events with very low multiplicities are likely to not pass this cut regardless of whether or not they are pileup events. It is essential that the same cut is used when correcting for trigger efficiency as described in

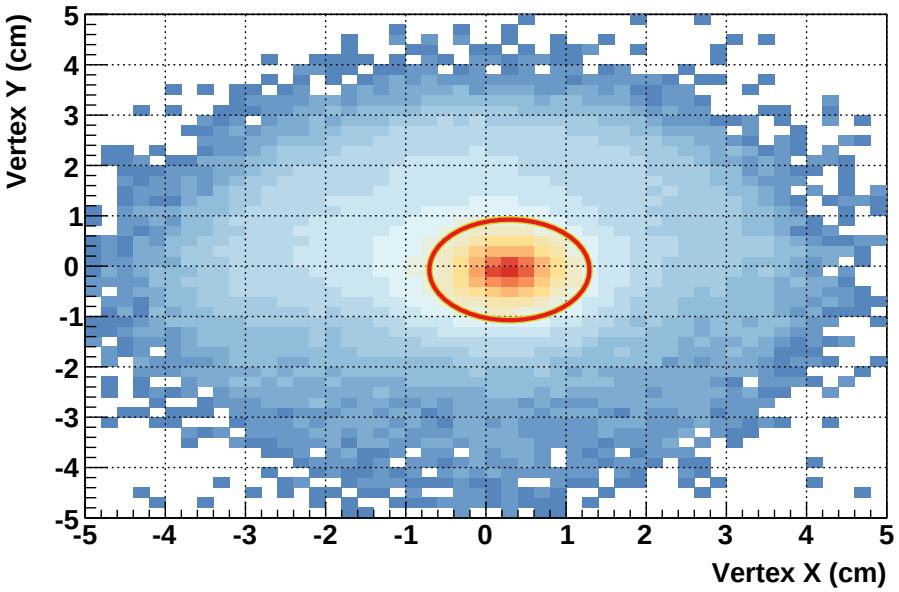

Figure 3.2: Vertex x, y cut at $\sqrt{s_{NN}}$ =39.0 GeV

The red line indicates the 1 cm radial cut around the beam center for the 39.0 GeV dataset. The z scale is logarithmic and the background level at 1 cm is roughly four orders of magnitude below the peak.

Quantity	Cut
(x, y) of vertex	$\sqrt{(0.2009 \text{ cm} - x)^2 + (-0.2547 \text{ cm} - y)^2} < 1$ cm
z of vertex	-30 cm $< z < 30$ cm
Number of ToF Matches	$3 \leq$ ToF Matches

Table 3.2: Event quality cuts at $\sqrt{s_{NN}}$ =7.7 GeV

Quantity	Cut
Number of Fit Points	$16 \leq$ Fit Points
Distance of Closest Approach	DCA < 1 cm
Fit Point Fraction	$0.52 <$ Fit Points/Possible Fit Points
$^{dE}/_{dx}$ Points	$11 \leq {}^{dE}/_{dx}$ Points
Global Over Primary Momentum	$0.7 <$ Global p_T/Primary $p_T < 1.43$
TOF Y-Local Variable	-1.6 cm $< y$-Local < 1.6 cm
TOF Z-Local Variable	-2.8 cm $< z$-Local < 2.8 cm

Table 3.3: Track quality cuts at all collision energies

Section 4.4.

The final event quality cut is the requirement that the z coordinate of the vertex be within 30 cm of the center of the detector. The purpose of this cut is to keep the track acceptance reasonably consistent between events. The possibility of extending the cut to accommodate the broad vertex distributions was considered but the increase in event numbers was not deemed significant enough to warrant the complex implications for the efficiency corrections.

3.5 Track Selection

A number of cuts are also applied to individual tracks in order to ensure their quality. A summary of these cuts is presented in Table 3.3. One specific goal of the cuts is to

eliminate tracks that do not correspond to real particles. It is possible for tracks to be reconstructed from collections of hits in the TPC that were left from many different particles. We only consider tracks with greater than 16 fit points in order to exclude these fake tracks. It also happens that the detector hits left by a single particle are reconstructed as two tracks with similar momenta. To avoid double counting in these cases we require that each track fit includes more than half of the maximum number of hits that the corresponding particle could have left.

We're solely interested in tracks that came directly from the collision and so we require that all analyzed tracks have a DCA of less than 1 cm. This helps to remove particles coming from Λ decays as well as secondary collisions in detector material. It also eliminates tracks that may have originated in the collision but that were too poorly tracked to point back to the primary vertex. Along these same lines we reject tracks where the momentum obtained when fitting only the detector hits, or the global momentum, differs significantly from the momentum obtained when the fit is required to include the event vertex, known as the primary momentum. The relationship between these two momentum values is shown in Figure 3.3. This cut eliminates tracks that are not consistent with originating at the primary vertex and also improves the momentum resolution.

We also want to exclude tracks that are not well suited for particle identification. Tracks with very few $^{dE}/_{dx}$ hits in the TPC have a poor overall $^{dE}/_{dx}$ resolution and so we remove these from the analysis by requiring at least 11 $^{dE}/_{dx}$ measurements for each track. The copper pickups in the MRPCs can measure signals from several centimeters beyond their edges but there is a much higher rate of mismatches and noise in these cases. We limit the variables y-local and z-local, which determine the location of a TOF hit relative to the center of a pickup, such that $|y\text{-local}| < 1.6$ cm and $|z\text{-local}| < 2.8$ cm to suppress background in the $^{1}/_{\beta}$ distributions. The importance of the y-local cut is illustrated in Figure 3.4.

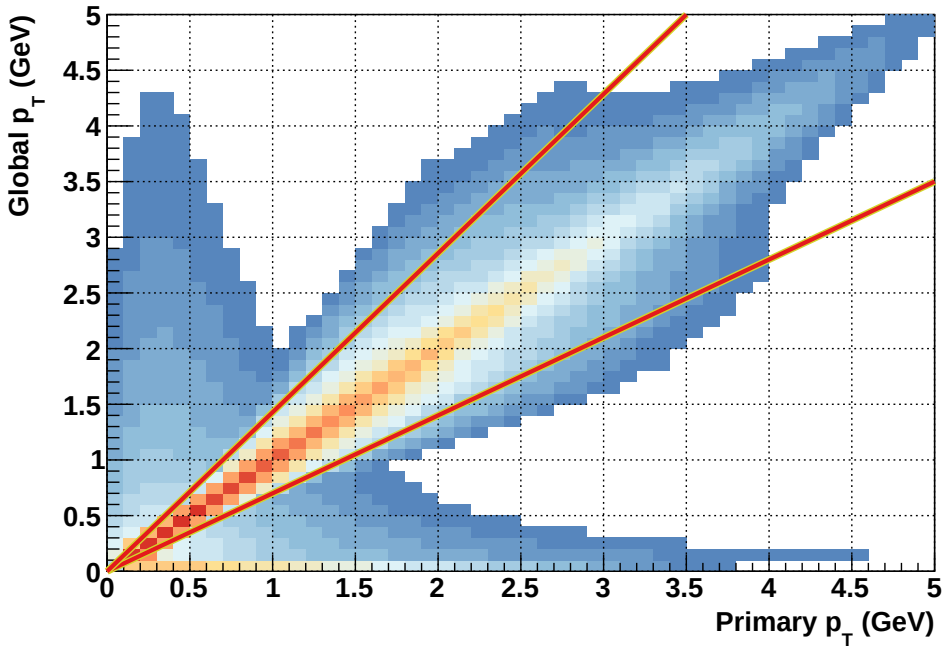

Figure 3.3: Global and primary momenta at $\sqrt{s_{NN}} = 62.4$ GeV

The relationship between primary and global transverse momentum shown on a log scale. The red lines indicate the applied cuts. The vast majority of tracks have nearly identical global and primary momentum but there are tails due to the finite momentum resolution. The background mainly consists of tracks with low global momentum and significantly high primary momentum, likely corresponding to particles created in secondary collisions that appear more rigid when they're pointed back to the primary vertex. Tracks with particularly bad momentum resolution are also eliminated.

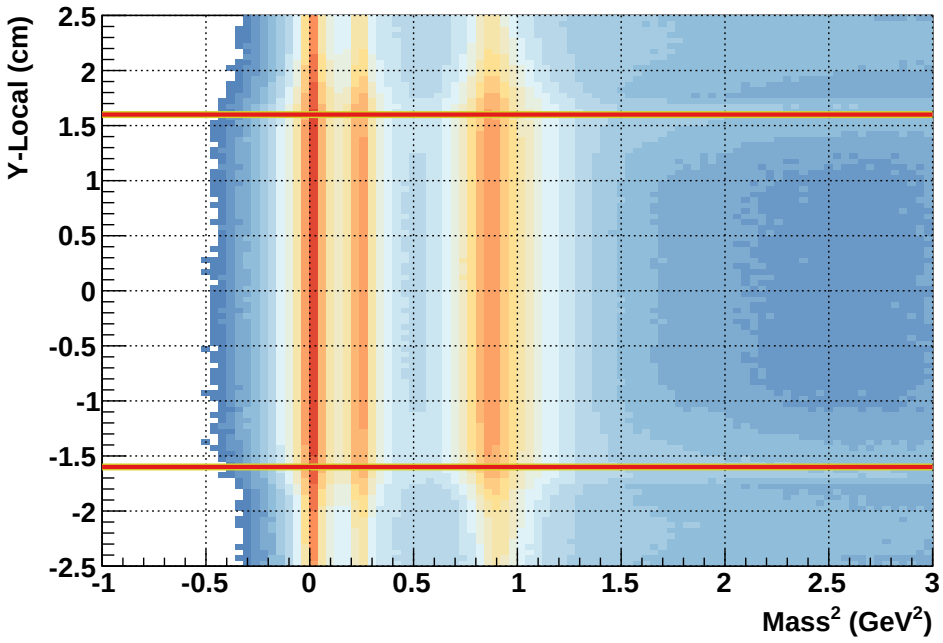

Figure 3.4: TOF y-local cut $\sqrt{s_{NN}} = 11.5$ GeV

The density of tracks as a function of y-local and reconstructed m^2 shown on a log scale for clarity in the backgrounds. The red lines correspond to the y-local cuts which correspond roughly to the edges of the MRPCs' pickups. Outside of these cuts the π, K, and p mass signals are much lower, and the background much higher, than they are around y-local$= 0$.

Chapter 4

Collision Centrality

The centrality of a nuclear collision is closely related to the impact parameter,b , which is the transverse distance between the centers of two nuclei during a collision. Collisions with an impact parameter of zero are maximally central events while larger impact parameters correspond to increasingly peripheral collisions. One possible definition of centrality is the cumulative distribution function of the Au+Au crosssection as a function of impact parameter. This gives the centrality as a number between zero and one or, alternatively, as a percentage.

The methodology surrounding the determination of centrality is very important in the current analysis. It allows us to differentiate between central collisions, where a significant volume of QGP is most likely to be formed, and peripheral collisions, which are more closely related to $p+p$ collisions and can therefore used as a null reference when looking for QGP signatures. It also provides trigger efficiency corrections and appropriate scaling factors for the various observables that are studied so that they can be reasonably compared between different centralities and collision systems. We will go through this methodology in some depth due to the key role it plays in the current analysis.

4.1 The General Approach

There is no way to measure the impact parameter directly and so we must try to infer centrality from what can be observed. The approach taken at STAR is to count the

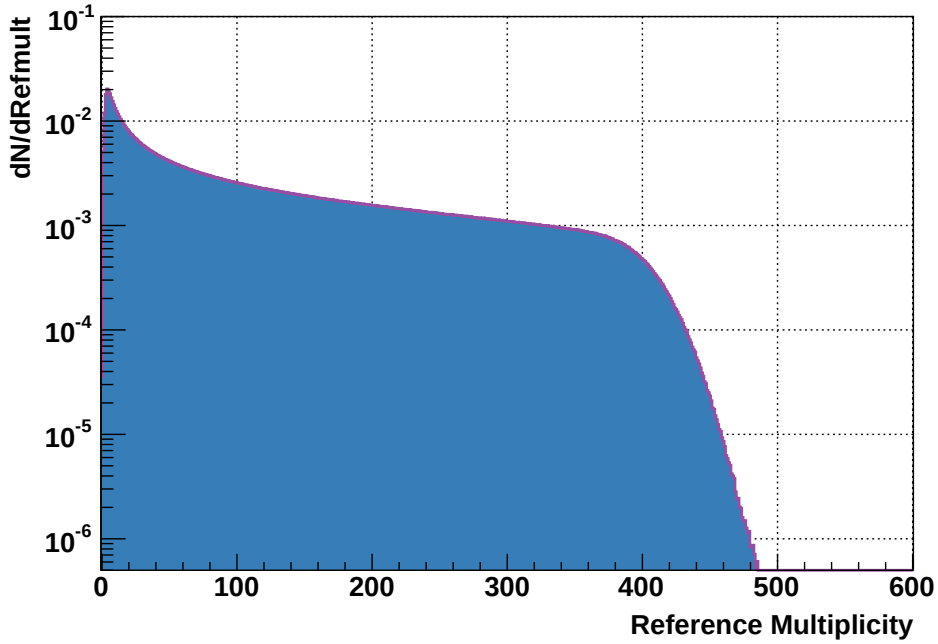

Figure 4.1: Reference multiplicity distribution for collisions at $\sqrt{s_{NN}}$ =62.4 GeV

number of observed charged particles with $\eta < 0.5$ and a DCA to the vertex less than 3 cm in an event. The pseudorapidity restriction attempts to ensure that there is uniform acceptance when varying the location of the collision along the z axis and the DCA cut limits contributions from decays and secondary interactions. The resulting quantity is often called a reference multiplicity, Ref_{mult}, or N_{ch} and a typical distribution can be seen in Figure 4.1.

The raw reference multiplicity has historically been used at STAR but in the BES data a correction step has been added. A major factor in the TPC reconstruction efficiency is whether there are any non-functioning sectors. During data taking for all BES energies there was at least one sector that was not functioning. This only affects TPC hits on one side of the central membrane and as a result the overall reconstruction efficiency varies as a function of the z coordinate of a collision which determines the ratio of hits on each side of the membrane. The relative efficiency as a function of this z coordinate was calculated from the data and the raw reference multiplicity was weighted to eliminate this dependence. The resulting value is often called the corrected reference multiplicity or $Ref_{multcorr}$.

The reference multiplicity is highly correlated with the volume of the emission system given that temperature is relatively constant as a function of centrality. The volume is, in turn, inversely correlated with the impact parameter. The complement to the percentile of reference multiplicity will therefore by closely related to the percentile of impact parameter. The distinctions between defining centrality in terms of the percentile in multiplicity, volume, or impact parameter are relatively subtle and often treated as interchangeable. These subtleties are hugely important for fluctuation analyses but when measuring particle yields the differences are much less important because the yields scale approximately linearly with volume.

A difficulty arises when using this definition in that a non-negligible fraction of peripheral events (~25%) have multiplicities that are too small to be triggered or reconstructed as events. This trigger inefficiency is quite clear in the region of small reference multiplicity in Figure 4.1, where the distribution turns over and falls towards zero. When using the percentile of observed reference multiplicity directly this would result in centrality estimations that are skewed towards peripheral values. To account for this, we must es-

timate the expected distribution of reference multiplicity and use this to determine the centrality percentile.

4.2 The Glauber Model

The trigger efficiency can be determined by using a Glauber Monte Carlo (GMC). There is some variation in how GMCs are formulated and we will focus on the procedure used in the present analysis. In the GMC, each colliding nucleus is modeled as a collection of nucleons which are randomly distributed according to the charge density of the nucleus. The relative x and y coordinates of the nuclei themselves are uniformly random over a range that encompasses all impact parameters that have a realistic opportunity for some interaction. A pair of nucleons, one from each nucleus, is considered a binary collision if the transverse distance between their centers is less than $\sqrt{\sigma_{\text{inel}}^{\text{NN}}/\pi}$, where $\sigma_{\text{inel}}^{\text{NN}}$ denotes the inelastic nucleon-nucleon cross section. Figure 4.2 illustrates a initial Monte Carlo (MC) geometry for a collision and differentiates between nucleons that have collided and those that have not.

The total number of collisions is denoted as N_{coll} while the total number of nucleons participating in at least one collision is written as N_{part}. The hard component of a collision scales with the number of binary collisions while the soft part scales more closely with the number of participants which is closely related to the volume. The total multiplicity of an event depends on both of these components which is addressed by introducing a mixing parameter x. The total reference multiplicity of an event with given values of N_{coll} and N_{part} is modeled according to a negative binomial distribution:

$$NB\left(N_{ch}; k, n_{pp}, m\right) \equiv \binom{N_{ch}+k-1}{N_{ch}} \left(\tfrac{n_{pp}}{k}\right)^{N_{ch}} / \left(\tfrac{n_{pp}}{k}+1\right)^{N_{ch}+k} \tag{4.1}$$

where n_{pp} represents the average reference multiplicity in a $p+p$ event, k determines the variance in a $p+p$ event to be $\sigma_{pp}^2 = n_{pp} + {}^{n_{pp}^2}/_k$, and m is scaling quantity equal to $[xN_{coll} + (1-x)\,{}^{N_{part}}/_2]$. After a random multiplicity is drawn, the effect of track reconstruction efficiency is applied by randomly generating a new multiplicity from a binomial distribution with efficiency ϵ. For the STAR detector the reconstruction efficiency is modeled as $\epsilon\left(N_{ch}\right) = 0.9\left(1 - \frac{N_{ch}}{2520}\right)$ which corresponds to an efficiency of 90% in $p+p$ and of

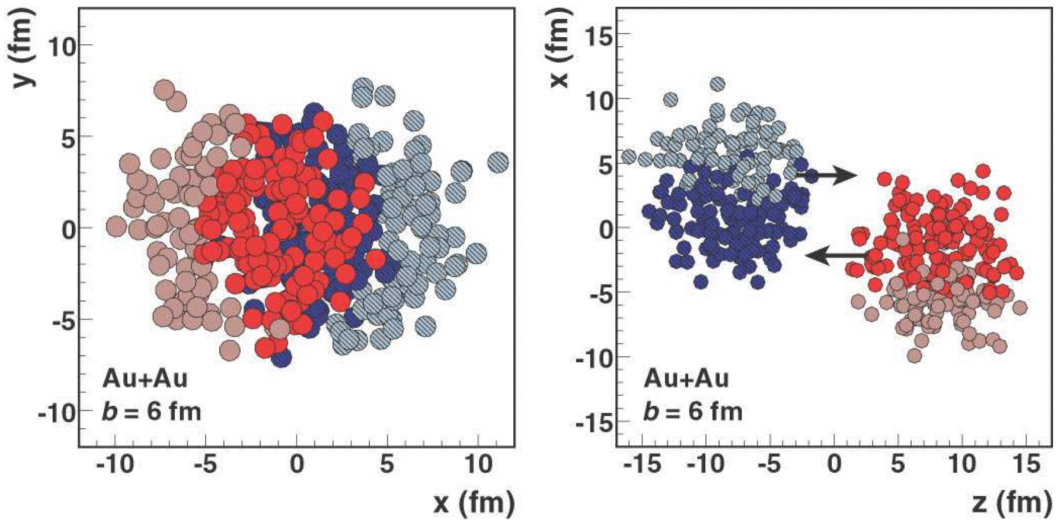

Figure 4.2: A Glauber Monte Carlo event

A GMC Au+Au event at a collision energy of $\sqrt{s_{NN}}$ =200 GeV with an impact parameter of 6 fm [65]. The left panel shows the transverse plane and the right panel shows the view along the beam axis. The nucleons are drawn as circles with radii equal to $\sqrt{\sigma_{\mathrm{inel}/\pi}^{\mathrm{NN}}}/2$ and participating nucleons are indicated with darker colors. Note that the right panel is shown without Lorentz contraction for clarity.

70% in fully central $Au + Au$ at $\sqrt{s_{NN}} = 200$ GeV. This is a rather crude approximation but any additional efficiency effects can be well described with small adjustments to the negative binomial parameters.

There are a number of parameters in the GMC that determine the resulting multiplicity distributions. The charge density as a function of radius for Au+Au is modeled with a Woods-Saxon distribution:

$$\rho\left(r\right) = \rho_0 \frac{1 + w\left(r/R\right)^2}{1 + e^{(r-R)/a}} \tag{4.2}$$

which has four parameters: ρ_0, the density at the center of the nucleus; R, the radius; a, the skin depth; and w, a parameter used to implement deviations from a spherical shape. These parameters have been measured in electron scattering experiments and values of $R = 6.38 \pm 0.136$ fm, $a = 0.535 \pm 0.05$ fm, and $w = 0$ were used, while ρ_0 becomes a normalization constant when treating the density as a probability distribution for each nucleon.

To determine the size of the nucleons at each energy, values of $\sigma_{\text{inel}}^{\text{NN}}$ are needed. These were determined using interpolations of world data. For $\sqrt{s}$ =7.7, 11.5, 19.6, 27.0, 39.0, and 62.4 GeV the respective resulting values were $\sigma_{\text{inel}}^{\text{NN}}$ =30.8 ± 1.5, 31.2 ± 1.6, 32.0 ± 1.6, 33.0 ± 1.7, 34.0 ± 1.7, and 36.0 ± 1.8. Additionally, values of n_{pp}, x, and k are needed to find the mean number of particles as a function of N_{coll} and N_{part}. In previous work, done by PHOBOS, it was found that $x = 0.145$ at 200 GeV and $x = 0.12$ at 19.6 GeV [66]. A central value of $x = 0.12$ was assumed for each of the BES energies but varied by ± 0.2 for the determination of systematic errors. Although n_{pp} and k could in principal be determined from $p + p$ data they are in practice determined by fits to the Au+Au multiplicity distributions.

4.3 Glauber Fits

A very large number of MC events are required to evaluate the likelihood for a single set of parameters for fitting. The fact that $\sigma_{\text{inel}}^{\text{NN}}$ is not a fit parameter allows for distributions of N_{coll} vs N_{part} to be precomputed and then values drawn from these distributions. An example of one such distribution is shown in Figure 4.3. The values drawn from

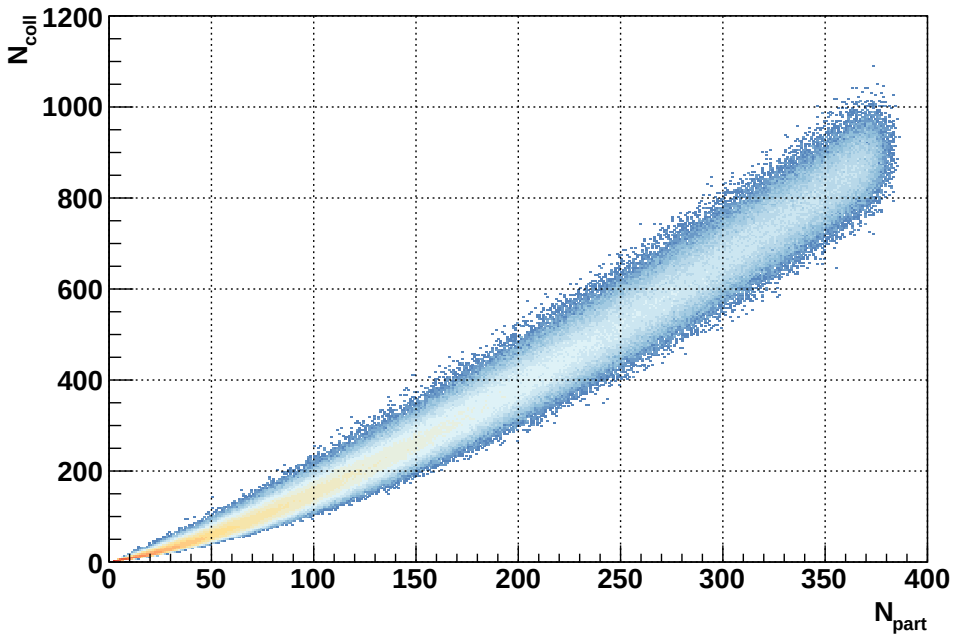

Figure 4.3: N_{coll} vs N_{part} distribution

N_{coll} vs N_{part} distribution for collisions at $\sqrt{s_{NN}}$ =7.7 GeV, shown with a log z-scale. This distribution is entirely determined for a given collision system by the parameters of the Fermi distribution and $\sigma_{\text{inel}}^{\text{NN}}$.

Fit Parameter	N_{ch} at Each Collision Energy (GeV)					
	7.7	11.5	19.6	27.0	39.0	62.4
n_{pp}	0.89	1.07	1.29	1.385	1.52	1.6
k	2.0	2.0	1.8	1.65	1.5	2.0

Table 4.1: Glauber fit parameters

these distributions are then used to generate initial multiplicities from negative binomial distributions with different parameter values. This process greatly reduces the required computation time and makes fitting a tractable problem.

The fits were restricted to regions of high multiplicity where the trigger efficiency is close to constant in order to avoid biases caused by the trigger efficiency. The fits themselves were done via χ^2 minimization and were carried out using a grid search on the n_{pp} and k parameters. The resulting parameters are listed in Table 4.1. It should be noted that these values, especially k, are sensitive to detector performance and reconstruction efficiency. The break in the downward trend of k at $\sqrt{s_{NN}} = 62.4$ GeV is simply a result of this.

4.4 Centrality Bins and Weights

After performing Glauber fits to the multiplicity distribution it is straightforward to determine the centrality for a given multiplicity as it is simply the value of the cumulative distribution function from the fit. A number of the corresponding values from the fits at each energy are shown in Table 4.2. The centrality percentages shown in the table are those used as the edges of centrality bins in the spectra analysis, though the 60-70% and 70-80% bin were merged for the R_{CP} analysis.

The definition of centrality bins such as these allows us to determine which centrality class an event belongs to but additional information about the trigger efficiency is needed in order to compute observables within the bin. The average spectra across the 70-80% bin for example would be skewed high because there are many more events with centralities towards the 70% side of the bin than the 80% side due to the trigger efficiency. In order

Centrality	N_{ch} at Each Collision Energy (GeV)					
	7.7	11.5	19.6	27.0	39.0	62.4
5%	185	221	263	288	316	339
10%	154	184	220	241	265	285
20%	106	127	152	168	185	199
30%	72	86	102	114	125	135
40%	46	56	66	74	81	88
50%	28	34	40	45	50	54
60%	16	19	23	26	28	30
70%	8	10	12	13	15	16
80%	4	5	6	6	7	7

Table 4.2: Reference multiplicities for various collision centralities

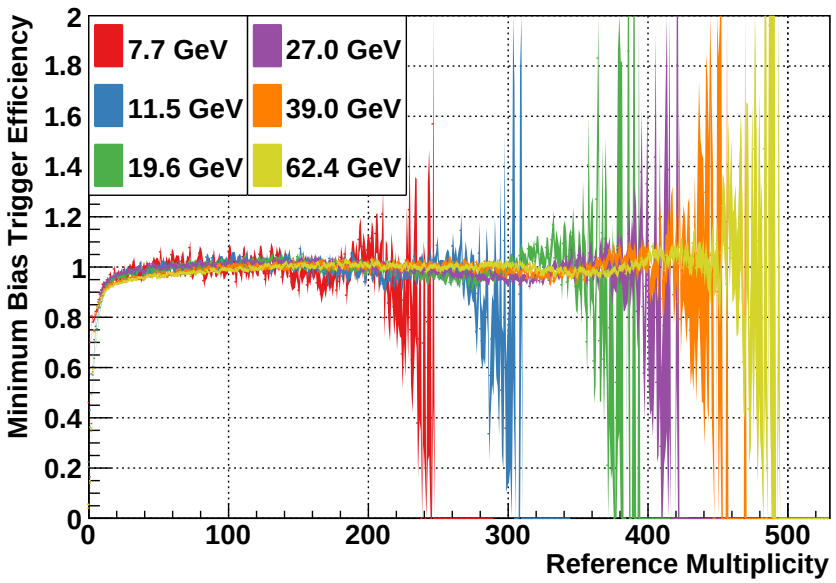

Figure 4.4: Minimum bias trigger efficiency

to account for this effect each event within a centrality bin needs to be weighted by the inverse of its trigger efficiency which can be calculated by taking the ratio of the observed multiplicity distribution over the Glauber fit to the distribution.

The trigger efficiency as a function of multiplicity can be seen at each BES energy in Figure 4.4. In all cases there is a clear drop in the efficiency for low multiplicity events and some distortion in extremely central events. This distortion is indicative of the minor breaking of the negative binomial assumption for particle production but has a negligible impact on the yields within the central bins.

4.5 Scaling Factors

Once the centrality bins and the parameters of the Glauber fit have been determined it is possible to simulate Glauber events, bin events on multiplicity, and then determine the distributions of quantities such as impact parameter, N_{part}, and N_{coll} for each bin. The natural scaling of hard processes with N_{coll} and soft processes with N_{part} make these quantities of particular interest when looking at spectra, as they are as scaling factors to compare between collision systems and centralities. Their mean values are given in Tables 4.3 and 4.4. The systematic errors in the tables were determined by varying the Glauber parameters according to their errors as were described in Section 4.2.

Very little collision energy dependence is observed in the mean N_{part} and N_{coll} values for a given centrality bin, but in the most central bins there is a clear rise as a function of collision energy. This can be explained by increased correlation between the centrality defined as percentile of multiplicity and that defined as percentile of N_{coll} or N_{part}. This correlation becomes strong in higher multiplicity events where the fluctuations of the negative binomial distribution become less relevant. For more peripheral bins, the increased correlation changes the width of N_{part} or N_{coll} but not the mean value. In central bins, on the other hand, the distributions are already truncated at their maximum values so an increased correlation primarily reduces the tail on the low side which results in higher average values overall. The largest magnitude of the effect on N_{part}, which dominates the low p_T spectra, is on order of 1% while that on N_{coll}, which dominates the high p_T spectra is on order of 15%. This centrality resolution effect is present in the spectra but

is accounted for in the other results where appropriate scaling factors are used.

Centrality	$\langle N_{coll} \rangle$ at Each Collision Energy (GeV)					
	7.7	11.5	19.6	27.0	39.0	62.4
0-5%	774±28	784±25	800±27	841±28	853±27	904±27
5-10%	629±20	635±20	643±20	694±22	687±21	727±21
10-20%	450±22	453±23	458±24	497±26	491±26	519±25
20-30%	283±24	284±23	285±26	312±28	306±27	322±27
30-40%	171±23	172±22	170±23	188±25	183±24	192±26
40-50%	96±19	98±18	96±18	106±20	104±20	109±21
50-60%	52±13	52±14	51±13	56±15	55±14	57±15
60-70%	25±9	25±9	25±8	27±10	27±9	27±10
70-80%	12±5	12±6	12±5	12±6	12±6	12±6

Table 4.3: N_{coll}values for each centrality bin

Centrality	$\langle N_{part} \rangle$ at Each Collision Energy (GeV)					
	7.7	11.5	19.6	27.0	39.0	62.4
0-5%	337±2	338±2	338±2	343±2	342±2	345±2
5-10%	290±6	291±6	290±6	299±6	294±6	297±6
10-20%	226±8	226±8	225±9	234±9	230±9	232±8
20-30%	160±10	160±9	158±10	166±11	162±10	164±10
30-40%	110±11	110±10	108±11	114±11	111±11	113±11
40-50%	72±10	72±10	71±10	75±10	74±10	75±10
50-60%	45±9	44±9	44±9	47±9	46±9	46±9
60-70%	26±7	26±7	25±7	27±8	26±7	27±7
70-80%	14±4	14±6	14±5	14±6	14±5	14±5

Table 4.4: N_{part} values for each centrality bin

Chapter 5

Particle Identification

5.1 Introduction

The process of PID is the main challenge of the analysis. As discussed in Section 2.2, the TPC gives $^{dE}/_{dx}$ measurements for tracks and the TOF information can be used to calculate $^{1}/_{\beta}$. These values vary as a function of $\beta\gamma$ and mass which allows them to be used for the purpose of PID. Use of ionization measurements for extracting particle yields has a long history at STAR and there is a standard parameterization of $^{dE}/_{dx}$, known as the Bichsel parameterization [67]. This is related to the Bethe-Bloch formula but includes a variety of additional corrections and is tailored specifically to the conditions in the STAR TPC. The relationship between $^{1}/_{\beta}$ and mass follows directly from $p = \gamma\,(\beta m)$ and is simply $^{1}/_{\beta} = \sqrt{1 + \left(\frac{m}{p}\right)^2}$. The parameterizations for both $^{dE}/_{dx}$ and $^{1}/_{\beta}$ are given in Figure 5.1 for π, K, p, and e. The electrons are included for reference but their yields at $p_T > 0.5$ GeV are negligible compared to pions, kaons, and protons and their yields are not extracted in this analysis.

At low momentum (< 0.5 GeV), the different particle species can be very easily identified from either $^{dE}/_{dx}$ or $^{1}/_{\beta}$ information because the distributions are so well separated. Narrow momentum slices of their distributions can be fit with Gaussian distributions or the number of particles can even be directly counted. The situation becomes more difficult as the $^{dE}/_{dx}$ values begin to merge at higher momentum values. Starting at around $p = 1.3$ GeV there are no longer any discernible peaks. If the shapes were known exactly

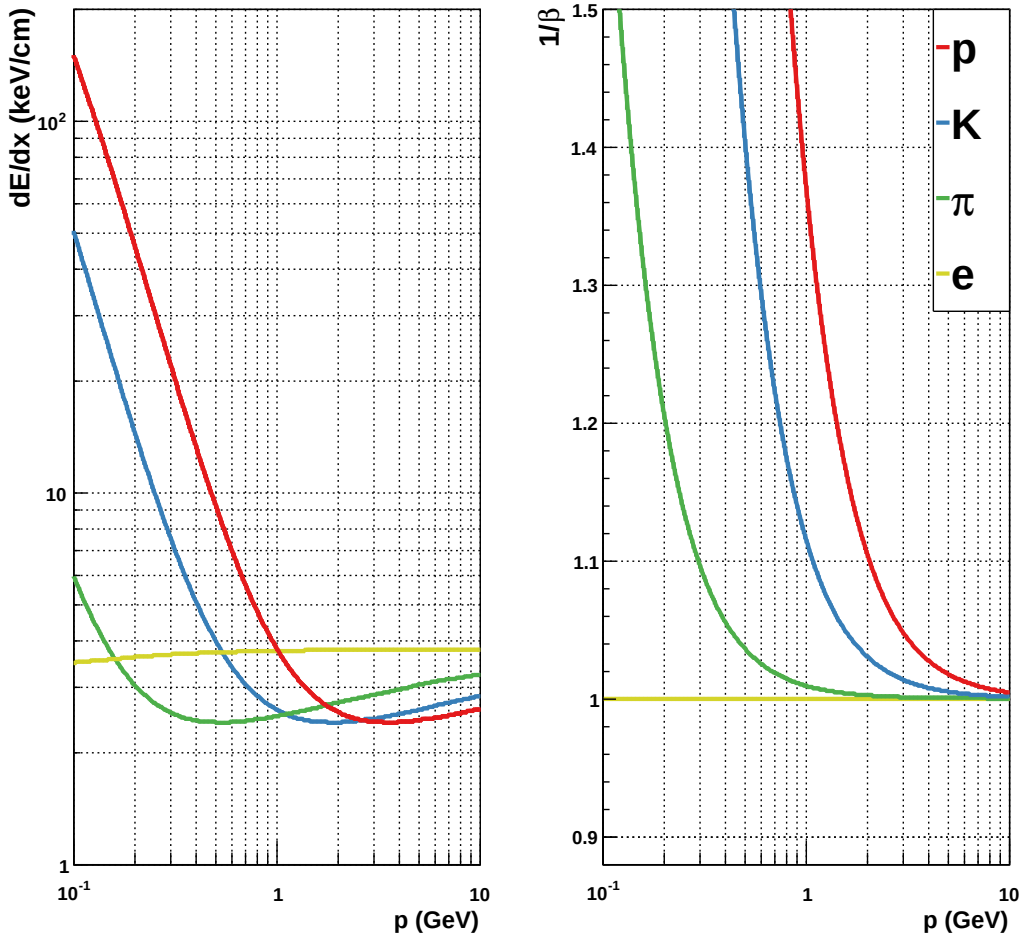

Figure 5.1: $1/\beta$and dE/dx as a function of momentum

The scales of the y axes are chosen to represent the space in which measurement errors are constant: logarithmic for dE/dx and linear for $1/\beta$. This means that the visual separation between curves is an accurate indicator for how easily particle types can be distinguished. The measurement errors at STAR are approximately 7% for dE/dx and 0.012 for $1/\beta$.

then it would still be possible to extract the yields by fitting to the distribution but in practice this is not the case.

The Bichsel parameterization does a very good job describing the data but it carries significant assumptions and is not exact. The calibrations of the detectors are also not perfect and there are many very small momentum and particle species dependent effects that bias measurements. For these reasons, assuming that the parameterizations hold directly when the peaks are not discernible can lead to extremely biased results that still appear to fit the data. Letting the means vary in a fit, on the other hand, does not constrain the problem well enough and there will be no convergence.

This situation has been dealt with in the past by treating protons and kaons as a single peak when fitting and then subtracting the K^0_S yield from the combined yield to get the proton yield [68]. This method carries significant systematic errors and there is really no way to know how many of the kaons end up in the "combined" yield relative to the pion yield. The ratio is highly dependent on the width that is chosen for the combined yield and it's easy to get proton yields that drift away from their true values at high p_T.

Another approach that has developed since the installation of the TOF is to rely on $1/\beta$ fits once the dE/dx peaks merge. The TOF gives good separation of pions and kaons up to about $p = 1.9$ GeV and of the protons up until $p = 3.0$ GeV. Above those points the same fitting difficulties arise and then worsen at higher momentum.

A natural extension of these methods would be to look at the 2d distribution of $1/\beta$ vs dE/dx and fit in this space. This was the approach first attempted in this analysis but a number of numerical stability issues were encountered and, with 6 energies x 6 centrality bins x 6 particle types = 216 sets of spectra to fit, the additional overhead of squaring the number of bins in each fit was quite large. These same issues had been encountered with STAR collaborators working on flow in the BES who took the approach of performing a rotation in $(1/\beta, dE/dx)$ and projecting onto the axis that maximized the separation between pions and kaons, allowing for identified flow measurements up to a maximum p_T of about 3.5 GeV [69].

We set out to extend the momentum reach of reliable particle identification as high as possible in the BES data. The procedure is outlined in the sections that follow.

5.2 Measurement Recentering and Correction

One of the main difficulties in extracting invariant yields at high p_T, where the peaks are not discernible, is that the widths of the distributions change drastically as a function of p_T. The widths must be extrapolated from low p_T in order to fit in the regions where the peaks are not discernible. This is not easy to do reliably when the widths are decreasing rapidly but will presumably level out to a constant value at some point. The complexity of these extrapolations is not a result of the measurement errors changing with momentum; these actually remain quite constant. It is instead caused by the fact that a single bin in transverse momentum and rapidity corresponds to a range of momentum values. The energy loss and time of flight measurements change drastically with momentum at low p_T and this results in a distinct broadening of the peaks.

A common way to reduce this broadening is to recenter the measurements around the theoretically expected value for the particle of interest. For ${}^{dE}/_{dx}$ the recentered distribution is typically defined as $z_{dE/dx}(X) \equiv \log({}^{dE}/_{dx_{\text{obs}}}) - \log({}^{dE}/_{dx_{\text{th},X}})$ where ${}^{dE}/_{dx_{\text{obs}}}$ is the observed energy loss and ${}^{dE}/_{dx_{\text{th},X}}$ is the Bichsel parameterization value for a particle of type X. Note that the $\log({}^{dE}/_{dx})$ is used because the measurement errors are constant in this space and the shapes can be more accurately modeled with Gaussian distributions. The units in the logarithm are arbitrary because any conversion would cancel in the subtraction. The equivalent recentering for ${}^{1}/_{\beta}$ is $z_{1/\beta}(X) \equiv {}^{1}/_{\beta_{\text{obs}}} - {}^{1}/_{\beta_{\text{th},X}}$ where ${}^{1}/_{\beta_{\text{obs}}}$ and ${}^{1}/_{\beta_{\text{th},X}}$ have analogous meanings. Each of these recentering definitions result in the particle of interest in having an approximately momentum-independent distribution centered near zero.

The recentering procedure improves the resolution of the peaks significantly but it is only a partial solution. Only the particle of interest will have a momentum-independent expectation and so the peaks for any other particle will still be broadened, again preventing reliable extrapolations. A nonlinear correction is necessary in order to recenter multiple particle species at once while preserving their measurement errors.

Let m correspond to a PID measurement, with normally distributed errors, such as ${}^{1}/_{\beta}$ or $\log({}^{dE}/_{dx})$ for a recorded track with momentum p. Then we can express the likelihood that the track corresponds to a particle with a specific identity X as:

$$\mathcal{L}\left(X|p,m\right)=\frac{1}{\sigma_X\left(p\right)\sqrt{2\pi}}e^{-\frac{\left(m-\mu_X(p)\right)^2}{2\sigma_X(p)^2}} \tag{5.1}$$

where $\mu_X\left(p\right)$ and $\sigma_X\left(p\right)$ are the mean and standard deviation of measurements for a particle of type X with momentum p. We then define our nonlinear recentering $z^{'}$ as:

$$\begin{aligned} z^{'}\left(X^{'}\right) \equiv & \frac{\sum_X \mathcal{L}\left(X|p,m\right)\left(m+\mu_X\left(\langle p\rangle\right)-\mu_X\left(p\right)\right)}{\sum_X \mathcal{L}\left(X|p,m\right)} \\ & - \frac{\sum_X \mathcal{L}\left(X|p,\mu_{X'}\left(p\right)\right)\left(m+\mu_X\left(\langle p\rangle\right)-\mu_X\left(p\right)\right)}{\sum_X \mathcal{L}\left(X|p,\mu_{X'}\left(p\right)\right)} \end{aligned} \tag{5.2}$$

where $\langle p\rangle$ is the average momentum of tracks in the current p_T and y bin. The first term uses a likelihood-weighted average adjustment of the measurement to what we would expect it to be if its momentum were $\langle p\rangle$ for each particle type X. This is the nonlinear transformation that removes most of the momentum dependence within the bin. The second term then subtracts the centroid of the peak for particle $X^{'}$ so that this distribution will be centered at zero. Recentering in this way is equivalent to the standard procedure when there is no variability of p within a bin. When p does vary, the corrected recentering procedure significantly outperforms the standard procedure which is demonstrated in Figure 5.2. We have denoted the corrected recentering as $z^{'}$ here but, from now on, we will refer to it as z for simplicity.

The quantities $\mu_X\left(p\right)$ and $\sigma_X\left(p\right)$ are not known exactly so instead we use the theoretical parameterizations for the means and the representative standard deviations of 0.07 for $^{dE}/_{dx}$ and 0.012 for $^{1}/_{\beta}$. These values are also used elsewhere when we refer to cuts on the number of standard deviations away from the particle centroids. The correction itself is not particularly sensitive to the values used unless they are very unrealistic and these approximations are quite good. The values of the standard deviation were varied by a factor of two as a cross-check and there was no significant change in the extracted yields.

When the distributions are well separated then the weighted average is entirely dominated by the most likely particle. Overlapping distributions allow for contributions to the correction from multiple particle types. This leads to some distortion in the shapes. The degree of distortion increases as the range of momentum values in each bin. The rapidity bin size was varied and the amount of variation in the centroids after recentering was measured to study this effect. It was found that the recentering procedure contributed

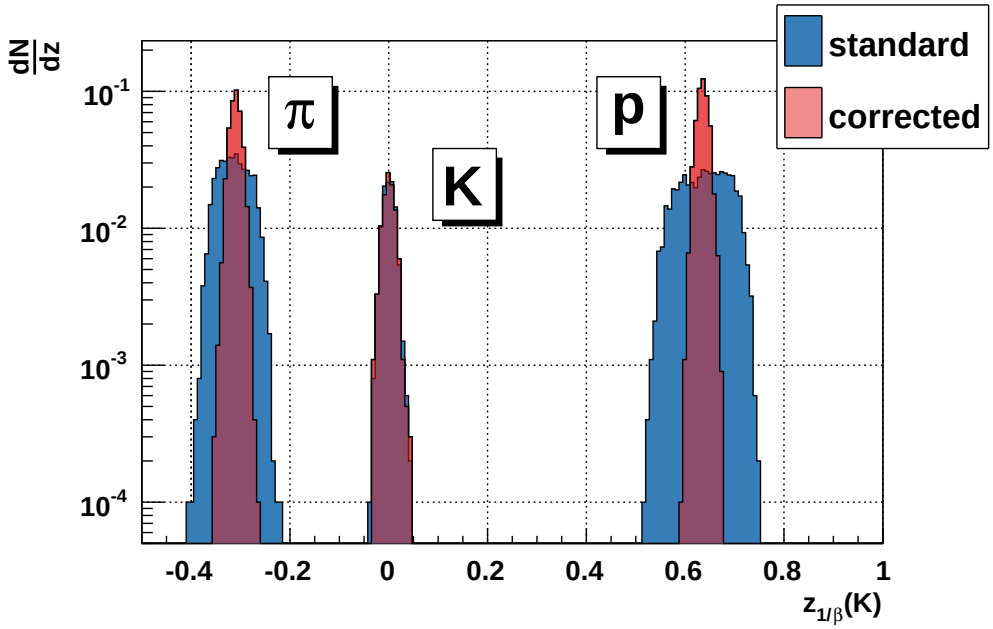

Figure 5.2: Corrected and uncorrected $z_{1/\beta}\,(K)$ variable

Comparison of the standard and corrected recentering methods for simulated data with $0.5 < p_T < 0.6$ and $|\eta| < 0.25$. The broadening of the pion and proton peaks is very apparent with the standard recentering procedure while the correction procedure results in much narrower distributions. More importantly, the widths become approximately constant as a function of momentum which allows for reliable extrapolations.

a maximum of about 5% to the $\log\left(^{dE}/_{dx}\right)$ and $^{1}/_{\beta}$ standard deviations with a rapidity window of $|y|< 0.25$. For larger bins the contribution grew significantly so this window was chosen as a balance between maximizing statistics and keeping the widths constant. Additionally, the contributions to the widths from this effect were measured and added in quadrature to the extrapolated values to account for the mild broadening.

5.3 Simultaneous Fitting

The general approach of the yield extraction was to produce a number of one dimensional distributions from the measured $z_{^{1}/_{\beta}}$ vs $z_{^{dE}/_{dx}}$ and then to perform fits to these 1D distributions. Four $z_{^{1}/_{\beta}}$ distributions were extracted for each p_T bin: one that includes all TOF matched tracks and three that include only tracks within a one standard deviation $z_{^{dE}/_{dx}}$ cut around the centroid for each particle type π, K, and p. A set of four were also extracted for $z_{^{dE}/_{dx}}$ with the same set of cuts applied to $z_{^{1}/_{\beta}}$ along with additional cuts at 3 σ above the protons and 3 σ below the pions to exclude deuterons and electrons, respectively. These eight distributions capture the vast majority of the information contained in the full $z_{^{1}/_{\beta}}$ vs $z_{^{dE}/_{dx}}$ distribution but have a tractable number of bins for numerical minimization.

The central idea is that the six distributions constructed with one sigma cuts will have a relative enhancement of their particular particle type as can be clearly seen in Figures 5.3 and 5.4. We take advantage of this by fitting all of the distributions simultaneously with a single set of shape parameters for each particle type. This allows us to leverage information from both detectors to determine the shapes of each particle distribution even when there is significant overlap of the peaks.

The parameterizations chosen were Gaussian distributions for each particle peak. This models the $z_{^{dE}/_{dx}}$ distributions very precisely and those of $z_{^{1}/_{\beta}}$ reasonable well, although the kurtoses of the true measurement errors are noticeably larger. The possibility of using Student's t-distribution was explored but the ν parameter was poorly constrained due to the large background. Instead, the fits were constrained to be within two standard deviations of the particle peaks and the uncertainty in TOF yields included as a systematic error.

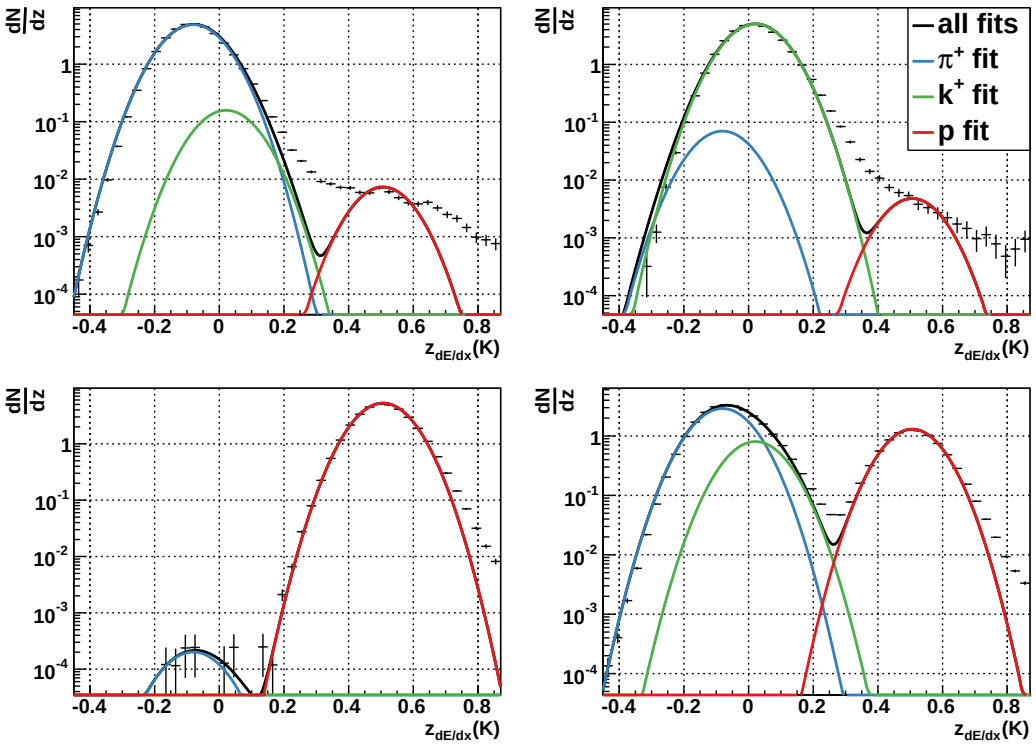

Figure 5.3: Particle-enhanced $^{dE}/_{dx}$ distributions at 19.6 GeV

Distributions of $z_{dE/dx}$ for the 0.8-0.9 GeV p_T bin for 0-5% central events at $\sqrt{s_{NN}}$ = 19.6 GeV. The distributions are pion enhanced, kaon enhanced, proton enhanced, and unenhanced in the upper left, upper right, lower left, and lower right panels, respectively. Notice that in the unenhanced distribution, which would typically be the sole distribution used for yield extraction, that the pion and kaon peaks are overlapping to such a degree that their relative yields are very ambiguous. The pion-enhanced and kaon-enhanced distributions give very clean samples which allow us to determine the correct shape for each particle type and to extract the yields from the unenhanced distribution.

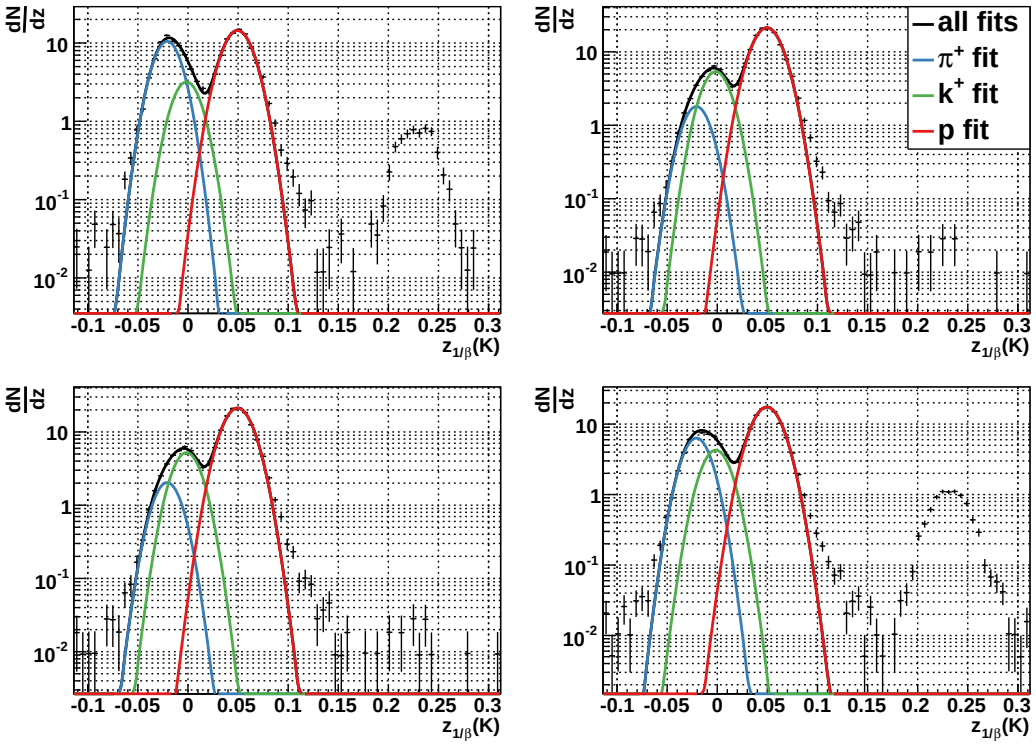

Figure 5.4: Particle-enhanced $^1/_\beta$ distributions at 19.6 GeV

Distributions of $z_{dE/dx}$ for the 2.4-2.6 GeV p_T bin for 0-5% central events at $\sqrt{s_{NN}}$ = 19.6 GeV. The distributions are pion enhanced, kaon enhanced, proton enhanced, and unenhanced in the upper left, upper right, lower left, and lower right panels, respectively. These distributions demonstrate the pion and kaon overlap in $z_{1/\beta}$ at high p_T. The pion and kaon enhanced distributions allow us to again disentangle the shapes so that we can extract yields, as was explained in the caption of Figure 5.3.

The set of eight distributions used in the simultaneous fitting all influence the μ and σ parameters for each particle type but only the two distributions without the enhancement cuts are used to extract the final yields. The particle yields in these two distributions should be the same but the yields will be significantly less in the enhanced distributions due to the restrictive cuts. We therefore allow the yield parameters in the enhanced distributions to all float freely while we require the yields in the unenhanced $z_{dE/dx}$ and $z_{1/\beta}$ to match.

This fitting procedure has proven to be very robust and to work well across collision energies and centralities without any fine tuning. Where pions and kaons are difficult to distinguish from $z_{dE/dx}$ measurements around $p_T = 1$ GeV the distributions can be accurately determined using the $z_{1/\beta}$ measurements. At $p_T \approx 2$ GeV the proton and kaon peaks become merged in $z_{dE/dx}$ while the pion and kaon peaks merge in $z_{1/\beta}$. The simultaneous fitting procedure allows us to combine information from both detector systems to disentangle these merged peaks and to extract yields with minimal shape assumptions.

As we move to higher momentum we eventually run into issues due to the low statistics and increased merging of the peaks in both $z_{dE/dx}$ and $z_{1/\beta}$. We address this issue by constraining the widths of the fit distributions. The means tend to drift as a function of p_T due to various calibration issues and subtle physics effects but the measurement widths remain relatively constant thanks to the recentering correction procedure. The recentering does cause some very minor broadening at high p_T but this is added in quadrature to the measurement width to determine the fit width. By fixing the measurement standard deviations once they have stabilized, we are able to leave the means unconstrained and extract yields out to $p_T = 7$ GeV.

5.4 Systematic Errors

There are two major assumptions in the outlined procedure which need to be reflected in the systematic errors of the extracted yields. The first is that the measurement widths are constant as a function of p_T. We address this by first evaluating the measurement widths where they are most easily determined from fitting. With $z_{1/\beta}$ this is taken to be 1.3 GeV $< p_T <$ 2.0 GeV for protons and 0.7 GeV $< p_T <$ 1.2 GeV for pions and

kaons. The lower limit on the ranges are there to eliminate contributions from momentum resolution and energy loss which broaden the peaks at low p_T. The corresponding ranges with $z_{dE/dx}$ are 0.6 GeV $< p_T <$ 1.0 GeV for pions, kaons, and protons. The average value of each width in these ranges is used at high p_T as the extrapolated value and the standard deviation of the width parameter is taken to be the systematic error.

To propagate the systematic errors through to the extracted yields we must determine how sensitive the yields are to the width parameters. We do this by randomly choosing each width parameter from a normal distribution with a standard deviation equal to the systematic uncertainty. The fitting procedure is then repeated 20 times and the standard deviation in the extracted yields is taken as the systematic error due to the uncertainty in the widths.

The other major contribution to the systematic error stems from the correspondence between the unenhanced $z_{1/\beta}$ and $z_{dE/dx}$ yields. These should ideally be exactly the same but in practice they differ due to mismatches, in-flight decays, and imperfect fit functions. To take these effects into account we introduced an additional fit parameter which determined the ratio between the unenhanced $z_{1/\beta}$ and $z_{dE/dx}$ yields and left it unconstrained in fits at low p_T where all of the particle distribution peaks are well separated. We found that the deviations varied but were on order of 5-20%.

Significant effort was invested in understanding the various effects responsible for the deviations but the ultimate conclusion was that these need to be included as a systematic uncertainty. The parameters were uniformly distributed between 0.8 and 1.2 when performing the set of fits for systematics in order to propagate this uncertainty through to the final yields. An illustration of this systematic uncertainty for each particle species is shown in Figure 5.5. It should be noted that the overall effect is more complicated than simply scaling the yields because it also shifts the means of each particle distribution. This necessitates repeating the fitting procedure with different values of the TOF matching efficiency to understand the impact on the final yields.

A number of other systematic errors will be introduced in Chapter 6 but the two systematic uncertainties outlined here will remain dominant.

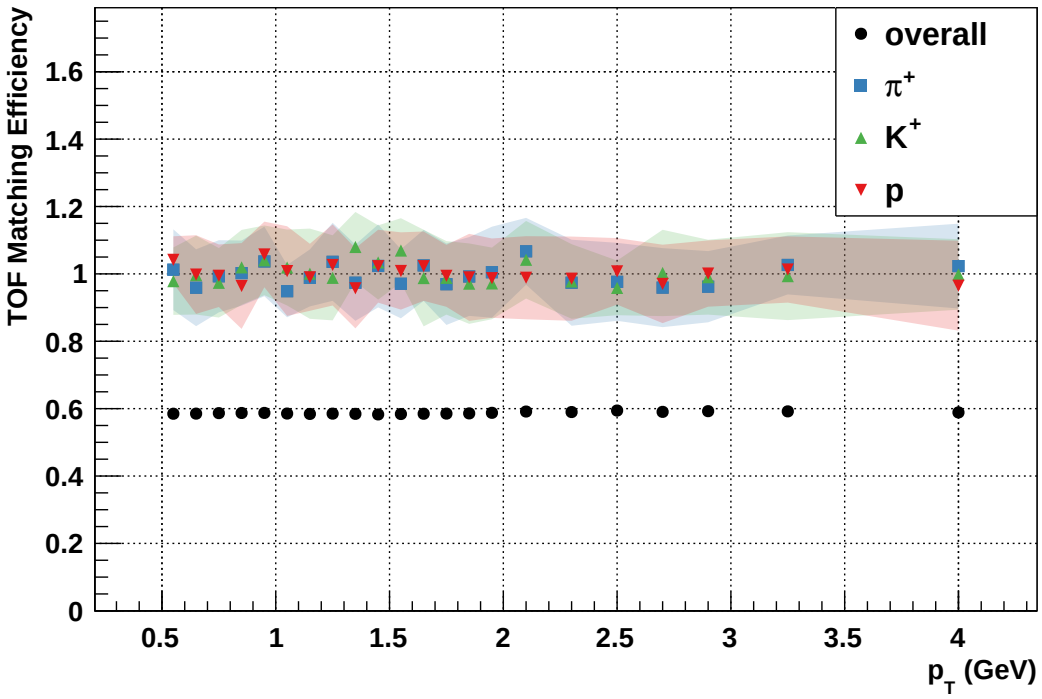

Figure 5.5: TOF matching efficiency at 19.6 GeV

TOF matching efficiency for events with 0-5% centrality at $\sqrt{s_{NN}} = 19.6$ GeV. The black points show the overall fraction of TPC tracks that were matched to a TOF measurement. The colored points show the additional species-dependent factor relating the $z_{1/\beta}$ and $z_{dE/dx}$ yields. The shaded bands show the systematic uncertainty in this factor.

Chapter 6

Spectra Corrections

Various corrections to the spectra are required in order to minimize biases introduced by both the experimental setup and physics outside of the focus of this analysis. In this chapter we outline the corrections that have been applied to spectra.

6.1 Spectra Fits

All of the corrections discussed in this chapter vary as a function of p_T. In order to apply these corrections to each data point some model is needed to describe the shape of the p_T distribution that the data point corresponds to. The simplest model is to assume that the data points accurately represent the spectra values at the center of each momentum bin. This model would suffice for very narrow bins but, because the high momentum focus of this analysis necessitates large p_T bins, we are better served by a more sophisticated model. Instead, we use physically-motivated fit functions to parameterize the p_T spectra and apply the corrections continuously across each bin.

6.1.1 The Boltzmann-Gibbs Model

For particles radiated from a small equilibrated thermal source with temperature T we can apply Boltzmann-Gibbs statistics to describe an invariant momentum spectrum. This gives the familiar expression in Equation 6.1 where the chemical potential and spin-

isospin-degeneracy factor has been been dropped because we are not interested in the overall scaling factor,

$$E\frac{d^3N}{dp^3} = \frac{d^3N}{p_T dy dp_T d\phi} \propto Ee^{-E/T} \tag{6.1}$$

We can then integrate over ϕ and evaluate at midrapidity to give the simplified

$$\frac{dN}{p_T dp_T} \propto m_T e^{-m_T/T}$$

where m_T is the transverse mass given by $\sqrt{p_T^2 + m^2}$. This model exhibits a turnover at low p_T followed by qualitatively exponential fall-off. This captures the basic behavior of the particle spectra and gives a reasonable approximation of the p_T distribution within each bin.

6.1.2 The Blast-Wave Model

In the low p_T region experimentally measured transverse momentum spectra are well described by the blast-wave model which applies longitudinal and transverse flow to thermal emission [70, 71]. The model is derived by integrating the superposition of Lorentz boosted Boltzmann-Gibbs invariant momenta spectra over the freeze-out hypersurface. The model assumes boost-invariant Bjorken longitudinal expansion in a region around midrapidity and allows for an arbitrary azimuthally-symmetric velocity profile [3]. If temperature and transverse flow do not depend on the longitudinal position in a longitudinally-comoving coordinate system then the transverse momentum spectrum factorizes and can be expressed independently of longitudinal flow as

$$\frac{dN}{p_T dp_T} \propto \int_0^R r dr m_T I_0\left(\frac{p_T \sinh\rho}{T}\right) K_1\left(\frac{m_T \cosh\rho}{T}\right) \tag{6.2}$$

where ρ is the Lorentz boost angle $\tanh^{-1}\beta_r$ for a given radius r and T is the freeze-out temperature [71]. The velocity profile is customarily chosen to be of the form $\beta_r = \beta_s\left({}^{r}/_{R}\right)^n$ where β_s is the surface velocity and the mean velocity is given by $\beta = \langle\beta_r\rangle = {}^{2\beta_s}/_{n+2}$. It was originally proposed to use $n = 2$ because early hydrodynamic solutions give a

radial dependence that closely resembled a quadratic profile but a linear profile has since proved more useful in describing data at both SPS and RHIC energies [72, 73]. It is now generally accepted to use a fixed value of $n = 1$, allowing for a broadly applicable description of the shape of thermal spectra that depends on only the two physically meaningful parameters β and T. The model has been extended to allow for azimuthal anisotropy in both momentum and coordinate space. These additions have a negligible effect when integrated over ϕ [74, 75, 76]. These extensions are therefore not relevant for our purposes.

6.1.3 The Tsallis Model

At intermediate to high p_T ($p_T > 1 - 2$ GeV/c) the thermal assumption of both the simple and blast-wave models breaks down as hard processes become the dominant source of particle production. The spectra in this region is known to exhibit power-law rather than exponential behavior [77]. A generalization of the Boltzmann distribution known formally as a q-exponential captures this power-law behavior at high p_T and exponential behavior at low p_T. This distribution, with or without the m_T factor, is more often called a Tsallis distribution in nuclear physics, after the Tsallis statistics from which it is derived [78, 79].

$$\frac{dN}{p_T dp_T} \propto m_T \left(1 + \frac{q-1}{T} m_T\right)^{-1/(q-1)} \tag{6.3}$$

Equation 6.3 gives the form of the Tsallis distribution which converges to Equation 6.1 as the non-extensivity parameter q goes to 1. This functional form has been shown to fit well both low and high p_T spectra at RHIC and LHC energies [80, 81, 82, 83]. The significance of its effectiveness at describing particle spectra is controversial. It could simply be a convenient functional form that evolves from exponential to power-law behavior as the physics shifts from soft to hard or it might be related to deeper physics such as anomalous diffusion or temperature inhomogeneities in the collisions [78]. In either case, it offers a model for fitting spectra that is more applicable across a broad p_T range than either the simple thermal or blast-wave models.

6.1.4 The Tsallis Blast-Wave Model

If we begin with a Tsallis distribution rather than a Boltzmann distribution in the derivation of the blast-wave model then we are able to get a description for particle spectra that captures the behavior of radial flow and thermal production at low p_T while better describing the Perturbative Quantum Chromodynamics (pQCD) power-law tails at high p_T. The result of this modification is given in Equation 6.4 [84].

$$\frac{dN}{p_T dp_T} \propto m_T \int_{-\infty}^{\infty} \cosh(y')\, dy' \int_{-\pi}^{\pi} d\phi \int_0^R r dr \times \left(1 + \frac{q-1}{T}\left(m_T \cosh(y')\cosh(\rho) - p_T \sinh(\rho)\cos(\phi)\right)\right)^{-1/(q-1)} \quad (6.4)$$

Unlike a the traditional blast-wave model, the rapidity and azimuthal angle no longer factorize in the transverse momentum spectrum. This means that the choice of the range to which the longitudinal boost is restricted is no longer inconsequential. In Equation 6.4 the range has been chosen to be infinite which is approximately true at midrapidity for RHIC energies [4].

6.1.5 Conclusion

After fitting the extracted spectra with each functional form we find that only the two blast-wave models can adequately describe the data due to the importance of radial flow. The Tsallis blast-wave model does, in some cases, better match the measured spectra due to the flexibility at high p_T but we also found that it sometimes has convergence issues during fitting. This behavior persisted even when fitting began with parameter values that gave good initial agreement with the data. In light of this, we use the blast-wave fits for our corrections and integrated yield extractions. None of the proceeding corrections vary much at high p_T so a perfect description of the spectra in that region is unnecessary.

6.2 Efficiency Corrections

The most significant correction that needs to be made is for the limited reconstruction efficiency of tracks in the TPC. The hits from some particles simply aren't reconstructed into tracks by the tracking algorithm. Other particles are reconstructed but are of questionable quality and get eliminated by track cuts designed to ensure that tracks correspond to actual particles. The measured particle yields are therefore lower than the true particle yields and the efficiency must be quantified and used to scale the observed yields.

To quantify the efficiency we simulate the detector response to MC tracks and determine what fraction of tracks are reconstructed by the STAR software. The simulation is done using GEometry ANd Tracking version 4 (GEANT4) in conjunction with components of the STAR framework which together generate detector responses for particles passing through geometries modeled after the STAR detectors [85, 86]. The resulting detector hits are then embedded into actual events before running reconstruction. The efficiency depends on background rates and a number of subtle effects and this embedding procedure creates the most realistic environment possible. The standard reconstruction code is run and tracks are matched with embedded particles based on the number of detector hits they share.

To determine the reconstruction efficiency within a given p_T, rapidity, and centrality bin we can simply apply our event and track cuts and take the ratio of matched tracks over embedded tracks for that bin. An example that illustrates the efficiency as a function of p_T is shown in Figure 6.1. There are large statistical fluctuations due to the limited size of the available embedding samples and so we exploit the smooth behavior of the efficiency as a function of p_T to construct a parameterization which we fit to the measured values.

The form of the parameterization for the reconstruction efficiency is given in Equation 6.5 and has been used extensively in STAR spectra analyses due to its ability to accurately describe the measured efficiency values from embedding. The effect of each parameter on the functional form can be qualitatively understood in the following way: a is the efficiency for high p_T particles that have relatively little curvature and escape the volume of the TPC, b is a characteristic momentum that sets the threshold for reconstruction of low p_T tracks, and c is a measure of how sharply the transition takes place.

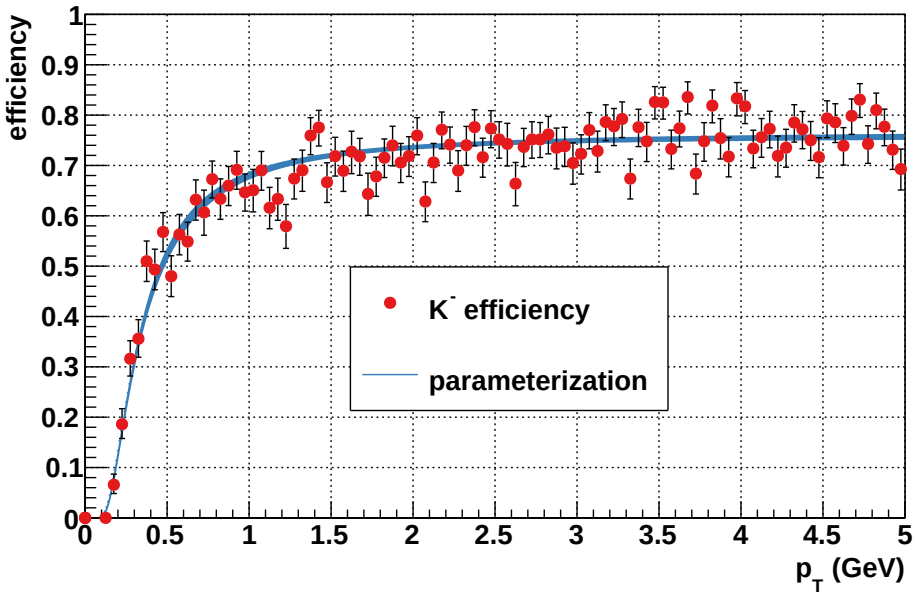

Figure 6.1: K^- efficiency at 27.0 GeV

K^- reconstruction efficiency at $\sqrt{s_{NN}} = 27.0$ GeV for a range of multiplicities between 321-360. The markers show the efficiency as calculated from embedding while solid line represented the parameterized fit.

$$\text{efficiency} = ae^{-(b/p_T)^c} \tag{6.5}$$

The fit parameters for each centrality bin are extracted and in all cases can be well described as linear functions of event multiplicity, as shown in Figure 6.2. The linear fits to the a, b, and c parameters are then used to calculate the efficiency for arbitrary values of reference multiplicity and transverse momentum. The uncertainty in the parameter fits is propagated through to give the systematic uncertainty for an efficiency value. The yield in a given bin is scaled by the inverse of its efficiency to correct for nonreconstructed particles. The systematic error on this procedure is included in the final yields.

There is an additional TOF matching efficiency that must be corrected for. This is a much simpler correction because it can be determined directly from the data as the fraction of tracks within a bin that have an associated TOF match. The matching efficiency is relatively p_T independent and has a value of about 60% as can be seen in Figure 5.5. The systematic uncertainty relating to this correction is taken into account independently, as explained in Section 5.4.

6.3 Background and Feeddown Subtraction

We arere primarily interested in the physics relating to particles that originate directly from a Au+Au collision. There are two additional sources for particles that do not originate in the collision: daughters from secondary weak decays and particles produced by collisions in the material of the detector or beam pipe. Our tight DCA cut reduces the contributions from these particles but there will always be some fraction of them that point back to the primary vertex and can't be eliminated by kinematic cuts alone. We turn to simulations to quantify and subtract the yields of these particles.

At each collision energy we simulated 100k minimum bias collisions using the Ultrarelativistic Quantum Molecular Dynamics (UrQMD) model [87, 88]. These simulated events were then run through GEANT4 and the STAR reconstruction software to recreate the experimental conditions as closely as possible. The same track and event cuts that are used in the analysis were also applied to the simulated data for the same reason. Each reconstructed track was then matched with the MC particle responsible for the predomi-

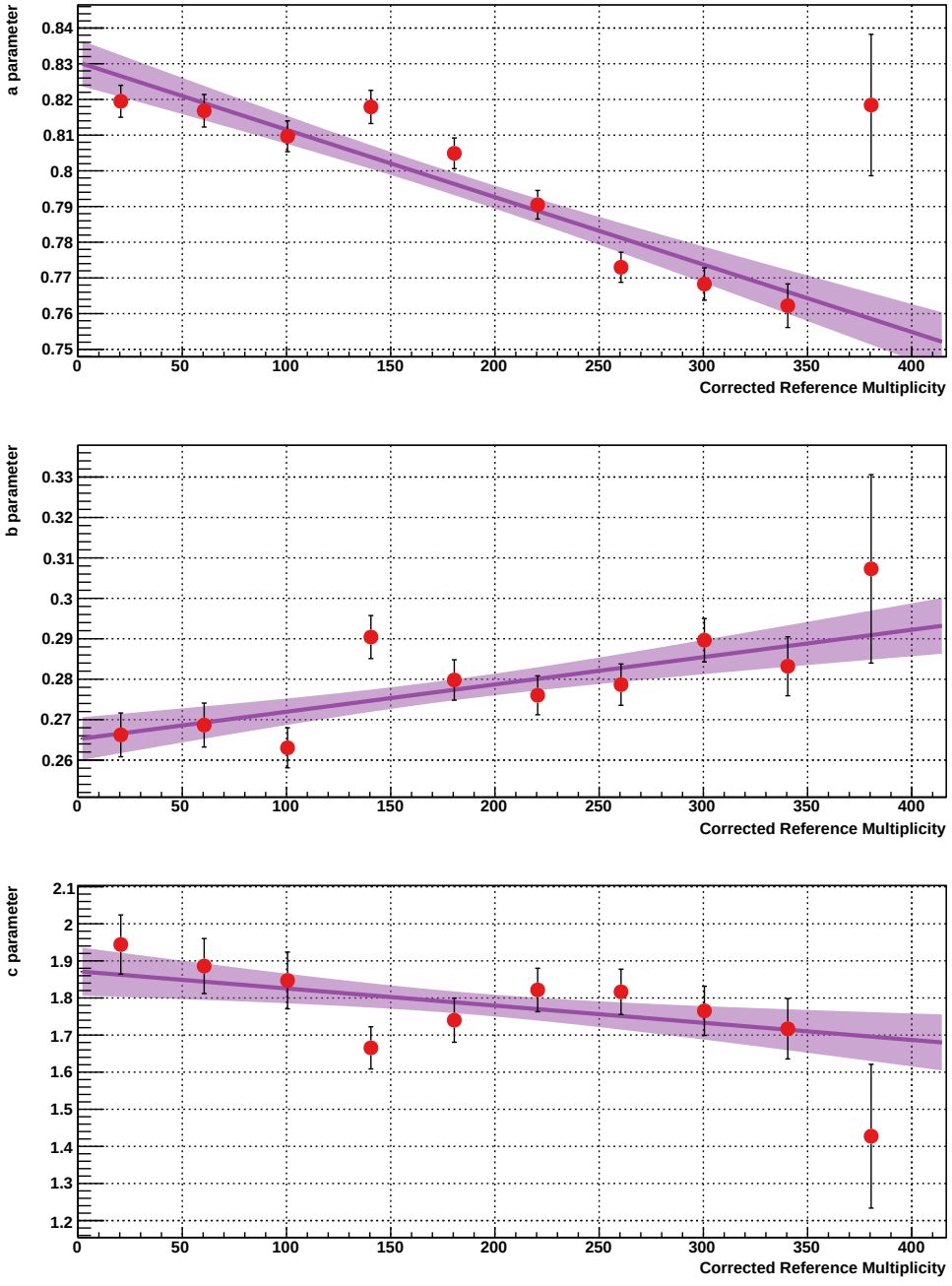

Figure 6.2: K^-efficiency parameter fits at 27.0 GeV

The fit parameters are shown as the red markers while the lines represent linear fits and the shaded bands the uncertainty on the fits.

Particle Type	Number of Parameters	Background Parameterization
π^-	2	$a_0 p_T^{-a_1}$
π^+	4	$a_0 p_T^{-a_1} + a_2 e^{-a_3 p_T}$
K^-	2	$a_0 e^{-a_1 p_T}$
K^+	2	$a_0 e^{-a_1 p_T}$
$\bar{p}$	3	$(a_0 + a_1 p_T^{a_2})^{-1}$
p	5	$a_0 \left(1 + a_1 p_T^{-a_2}\right) e^{-a_3 p_T} + a_4$

Table 6.1: Background parameterization functions

The functional forms used to describe the backgrounds for each particle type. The i^{th} parameter is represented by a_i. These functional forms were found to describe the fractional background yields as a function of p_T across all centrality bins and collision energies.

nant fraction of its detector hits. This matching allows for each track to be traced back to an origin process and parent. An example of the breakdown between various contribution sources can be seen in Figure 6.3.

The fractional portion of particle yields coming from background and feeddown was measured as a function of p_T in the simulation data for each particle type, centrality bin, and collision energy. The fractional yield was used in order to mitigate any potential disagreements between the true particle yields and those produced by UrQMD. To reduce the effect of statistical fluctuations, representative functional forms were chosen that could describe the behavior of the background and be used as parameterizations. The background characteristics are quite different for the different particle types which necessitates the use of parameterizations with varying degrees of complexity. The functional forms that were chosen are summarized in Table 6.1.

Examples of two prototypical fits are shown in Figure 6.4. The measured experimental yields are reduced by the parameterized fraction to remove the background and feeddown contributions. The systematic uncertainty in this correction is taken to be the statistical uncertainty in the fits. The correction above $p_T = 2.5$ GeV, the region of interest for hard physics, is on order of at most a few percent and has very little impact on the final results.

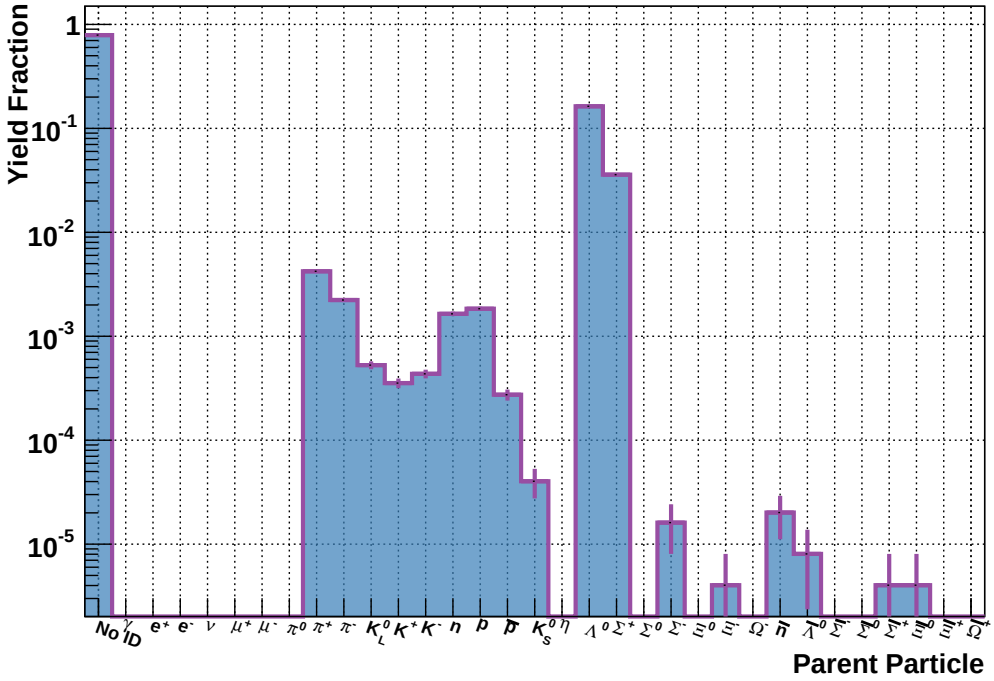

Figure 6.3: Parent particles for protons at 62.4 GeV

The fraction of total observed protons coming from various parent particles in a 0-5% central event at $\sqrt{s_{NN}}$ = 62.4 GeV. The fraction labeled as "No ID" corresponds to particles that were produced in the UrQMD event and embedded into GEANT4. The dominant source of secondary protons is feeddown from Λs and Σs which are responsible for roughly 15% of the total proton yield. Protons knocked out of detector material by particles created in the initial collision also contribute but this amounts to only about 1% of the total proton yield.

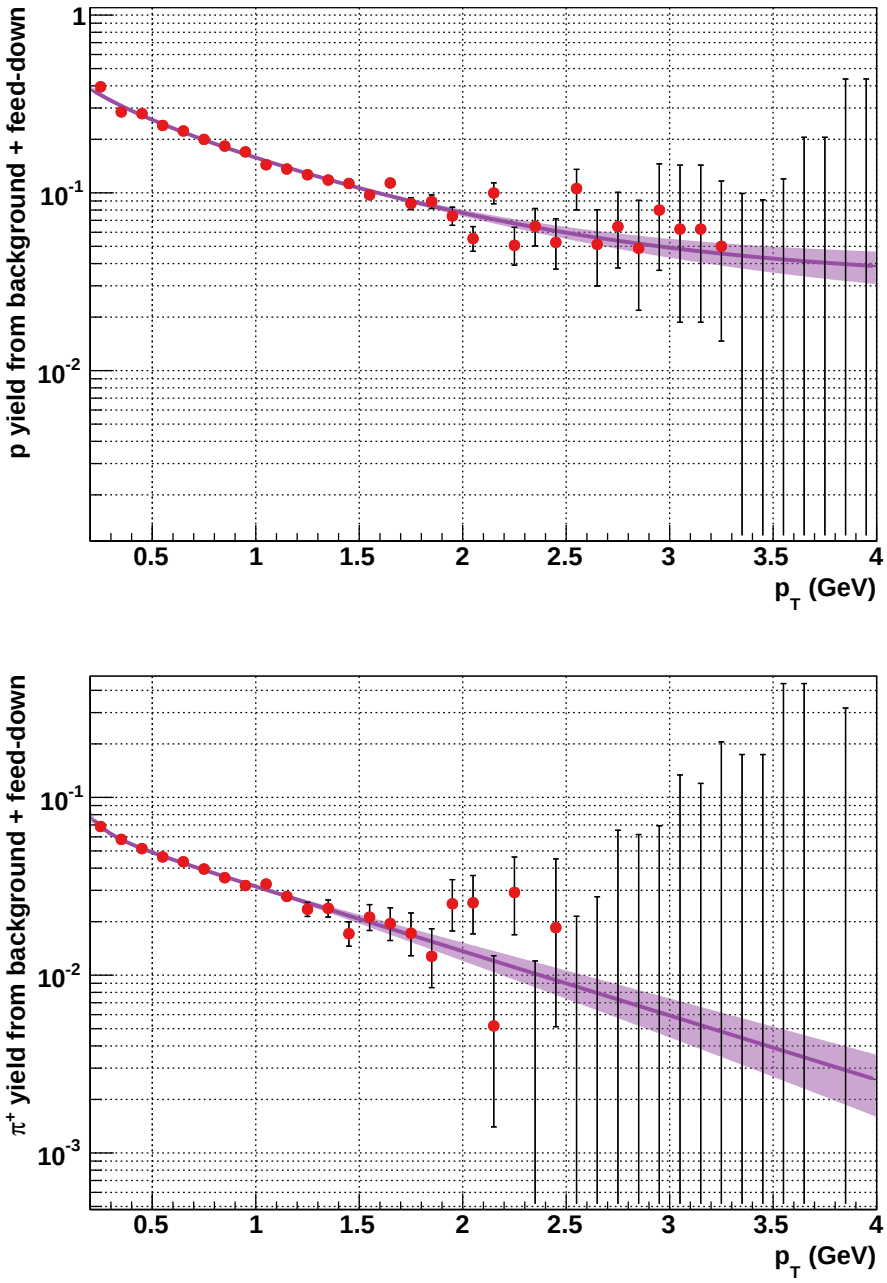

Figure 6.4: Background parameterizations for pions and protons at 19.6 GeV

Two example background fits for positive pions and protons at $\sqrt{s_{NN}} = 19.6$ GeV. Kaons are not shown because the feeddown contribution is negligible ($< 1\%$) above $p_T = 0.5$ GeV. The shaded bands indicate the systematic uncertainty in the fits.

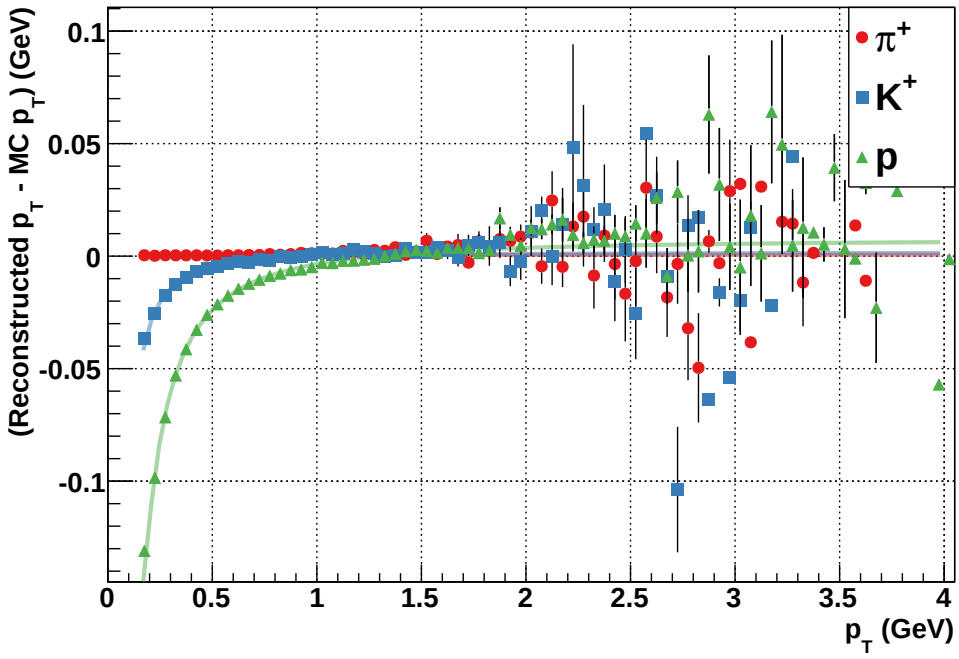

Figure 6.5: Energy loss in collisions at 7.7 GeV

6.4 Energy Loss Corrections

A particle passing through the STAR detector loses energy as it does so, which results in a decreasing radius of curvature along its path. The momentum that is reconstructed by fitting a helix to the detector hits it leaves behind will tend to be systematically low as a result of this. In order to counteract this effect the momenta of all tracks are calibrated during reconstruction with the assumption that the particles were pions. This calibration works very well when the particles are indeed pions but both protons and kaons lose more energy than pions and so they require an additional correction.

The energy loss for protons and kaons can be estimated by studying the same GEANT4 simulations of events that were used for the background and feeddown subtraction. After applying our standard set of cuts we measure the difference in transverse momentum between each matched pair of reconstructed and embedded tracks to determine the average energy loss as a function of p_T. The bias in p_T is parameterized by fitting the functional form $a + bp_T^{-c}$ for each particle type and the uncertainty in the fit is taken as a systematic

error. The energy loss does not depend on centrality and so a single set of parameterizations is used for each energy. An example of the fits to the simulated data can be seen in Figure 6.5.

Chapter 7

Results

7.1 Identified Particle Spectra

As discussed in detail in earlier chapters, a robust approach to yield extraction was developed which simultaneously leverages multiple PID detectors and is highly tolerant to calibration errors. This method has allowed for the measurement of identified particle yields up to $p_T = 6$ GeV, well into the region where PID at STAR had previously not been possible without significant additional assumptions (e.g. fixing charged kaon yields to match those of K^0_S [89]). The extracted yields have been carefully corrected for a variety of effects including trigger efficiency, track reconstruction efficiency, energy loss, proton knockout, and weak decay feeddown. The end result is a comprehensive set of exclusive identified particle spectra for $\pi^{+(-)}$, $K^{+(-)}$, and $p(\bar{p})$ across six different centrality ranges and at six different collision energies which help fill the significant gaps between previous SPS and RHIC energies. An example of the spectra for the $0-5\%$ most central bin can be seen in Figure 7.1.

Although the spectra themselves are difficult to interpret directly, they are undeniably the key accomplishment of this analysis. From here there are wide opportunities for model comparisons or fitting and for the extraction of physically meaningful qualities. I will attempt to revisit several of the main QGP observables that were discussed in the introduction but also note that these spectra open the doors for a variety of future analyses and have additionally already been used to improve efficiency corrections in a

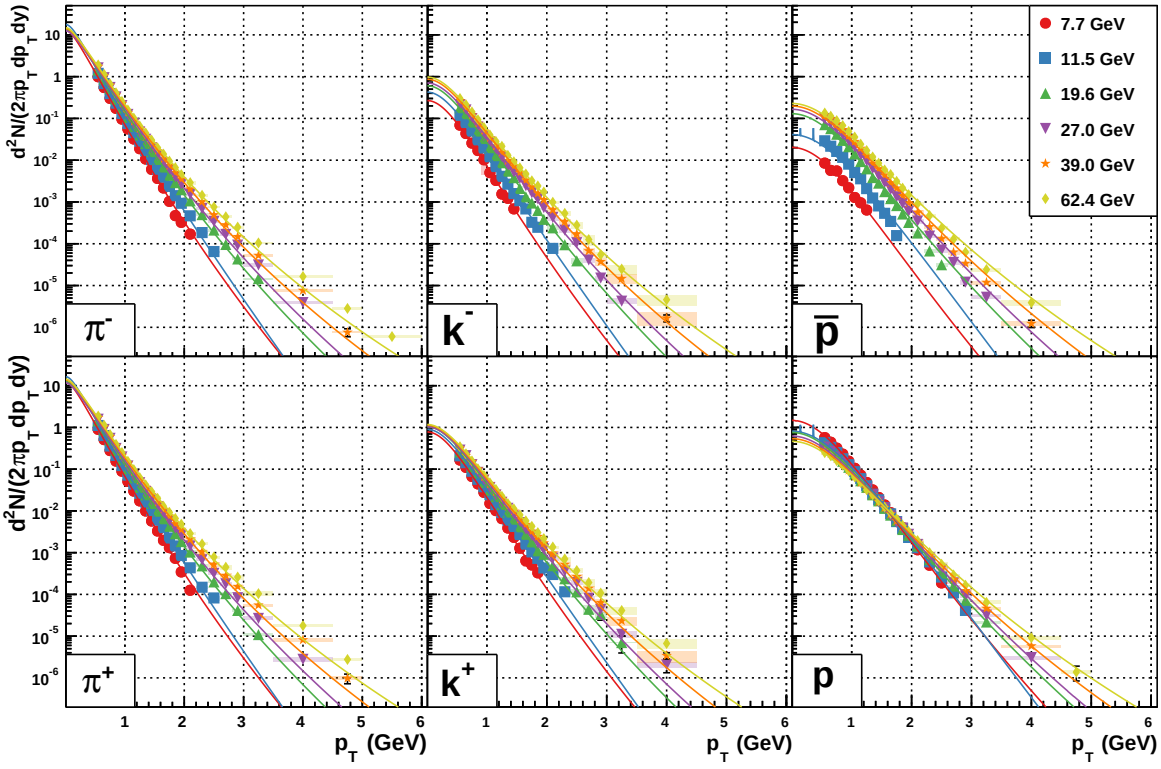

Figure 7.1: Exclusive identified particle spectra

Identified particle spectra for 0-5% central events at each collision energy after all previously discussed corrections have been applied. The solid lines represent Tsallis-Blastwave models fit simultaneously across the six particle types at each collision energy.

net kaon fluctuation analysis and to refine the cocktail in a dilepton analysis.

7.2 Integrated Yields at Midrapidity

A natural next step after producing the identified particle spectra is to look at the integrated yields at midrapidity. These were found by turning off weak decay subtraction in the analysis so that the charged yields would be more directly comparable to the inclusive charged particle spectra used in the other analyses. The central spectra for a given energy were then simultaneously fit with Blastwave functions which were subsequently weighted

by a factor of $y_{\max}/\sinh^{-1}\left(\sinh\left(y_{\max}\right)m_T/p_T\right)$ where $y_{\max} = 0.25$ before integrating to account for the use of a rapidity window in the analysis rather than a pseudorapidity window. The resulting integrated yields for each particle type were then summed together and scaled by the Glauber model expectations of $\langle N_{part}/2\rangle$ for the $0-5\%$ centrality bin at each energy. This scaling ensures a reasonable comparison between Au+Au and Pb+Pb systems and partially accounts for the lower centrality resolution at lower collision energies. The final integrated yields can be seen in Figure 7.2.

The first thing to note is the stunning agreement with both the SPS and previous RHIC results. Considering how vastly different the detectors and analyses were this consistency is really a testament to the quality of the work that went into them. The next striking feature is that the new measurements appear to drop below the logarithmic fit that appeared in the PHOBOS whitepaper. This logarithmic scaling had been shown to break with the LHC results and they proposed a power-law fit which is also shown in Figure 7.2. The current results are clearly more consistent with this power-law than with the logarithmic curve and even hint at a more pronounced flattening between $\sqrt{s_{NN}} = 19.6$ and 62.4 GeV.

There have been several BES results so far that have been interpreted as possible evidence of a softening of the equation of state of nuclear matter. Examples of these include net proton directed flow having a minimum at a center of mass energy of 19.6 GeV [103] and the event-averaged p_T exhibiting a similar minimum at the same energy [104]. The charged particle densities presented here, when coupled with the energy density estimates from Section 7.3, suggest a minimum in the system's charged particle number susceptibility to an increase in energy density, $^{dN_{ch}/d\eta}/_{d\epsilon}$, near this same collision energy of 19.6 GeV. It is tempting to see this as clear evidence of a softening of the equation of state but it is important to remember how drastically the baryon chemical potential is dropping as a function of increasing collision energy. The two previously cited analyses have minimums that hinge on the reduction in baryon stopping at higher energies and this is a possibility for any analysis that looks at all charged particles. Indeed, the plateau-like behavior observed here is driven entirely by the dropping proton yields and does not appear when only meson yields are considered. This does not necessarily exclude interesting physics happening but it makes it clear that what we're seeing is a conflation

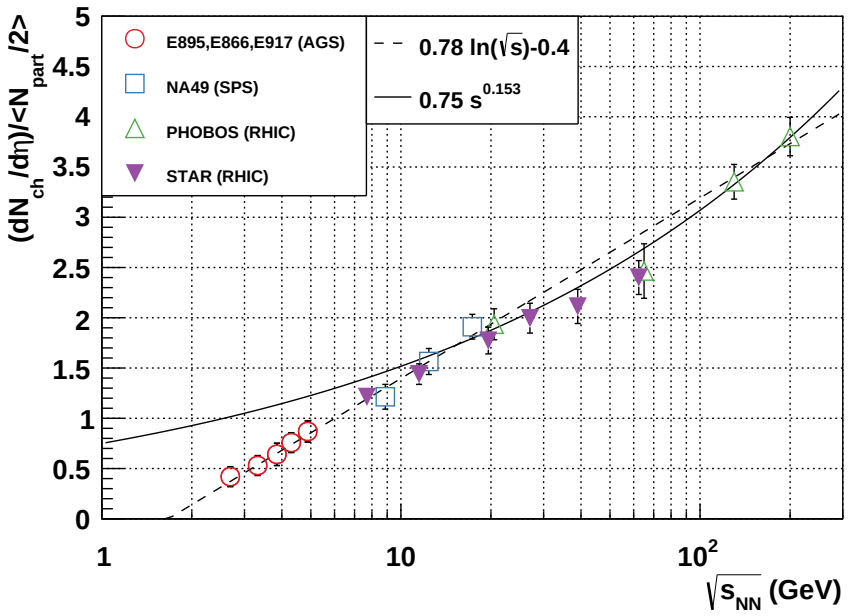

Figure 7.2: Charged particle yields at mid-rapidity

The STAR BES charged particle densities at mid-rapidity shown with assorted results from the AGS [90, 91, 92, 93, 94], SPS [95, 96], and RHIC [97, 98, 99, 100, 101, 102]. The previous RHIC results at $\sqrt{s_{NN}} = 19.6$ and 62.4 GeV are offset slightly to the right for clarity of the error bars. The logarithmic fit shown as a dashed line was the standard fit to the world data prior to the first LHC results. After the turn-on of the LHC this logarithmic scaling was observed to be broken and the solid line power-law fit proposed as a more accurate description [5]. The new results show a clear softening of the logarithmic scaling in the region of $\sqrt{s_{NN}} = 19.6 - 62.4$ GeV, even moreso than what was suggested by the LHC results.

of the system's response to both baryon chemical potential and energy density.

7.3 Energy Density

From the integrated yields we can construct estimates of the energy density for the system. The same prescription laid out in the previous section was followed at each collision energy to produce integrated $^{dN_X}/_{d\eta}$ values for each particle type X, again including weak decay daughters. Additionally, the Blastwave fits were integrated with a factor of m_T for each particle to find the average transverse energy $\langle E_T \rangle$ for each particle. The π^0 integrated yield and $\langle E_T \rangle$ were then estimated to be the averages of the corresponding quantities for charged pions. The same assumption was made for the relationship of K^0_S to charged kaons. Neutrons were a slightly more complicated case which needed to be treated separately for stopped and created baryons. For the created baryons it was estimated that there would be twice as many combined neutrons and anti-neutrons as there are anti-protons and that they would have the same $\langle E_T \rangle$. For stopped baryons it was assumed that the yield of stopped neutrons would be equal to the yield of protons minus the yield of antiprotons multiplied by a factor of $^{118}/_{79}$ to account for the ratio of neutrons to protons in a gold nucleus. The average transverse energy for the stopped neutrons is then given by $\langle E_{T,n} \rangle = \left(\langle E_{T,p} \rangle N_p - \langle E_{T,\bar{p}} \rangle N_{\bar{p}}\right)/_{(N_p - N_{\bar{p}})}$.

Once these quantities were calculated the total energy was tabulated within $|\eta| < 0.25$ and scaled by the inverse fraction of solid angle that this covered (~ 6.35). It's important to note here that we are not making an assumption of isotropic emission but rather we're focusing on the portion of the distribution that is consistent with isotropic emission from a source at midrapidity. This procedure gives an estimate of the total energy of particles emitted at midrapidity with momenta consistent with that of an equilibrated source.

With the total energy calculated all that is needed to find the energy density is the volume of the equilibrated system. There are several ways to estimate this volume but I've chosen to use the assumptions proposed by Bjorken [3], namely that the system has expanded in the longitudinal direction at the speed of light for 1 fm/c and not at all in the transverse direction. This set of assumptions was chosen because it has been used by a number of other experiments and therefore allows for somewhat more direct comparisons.

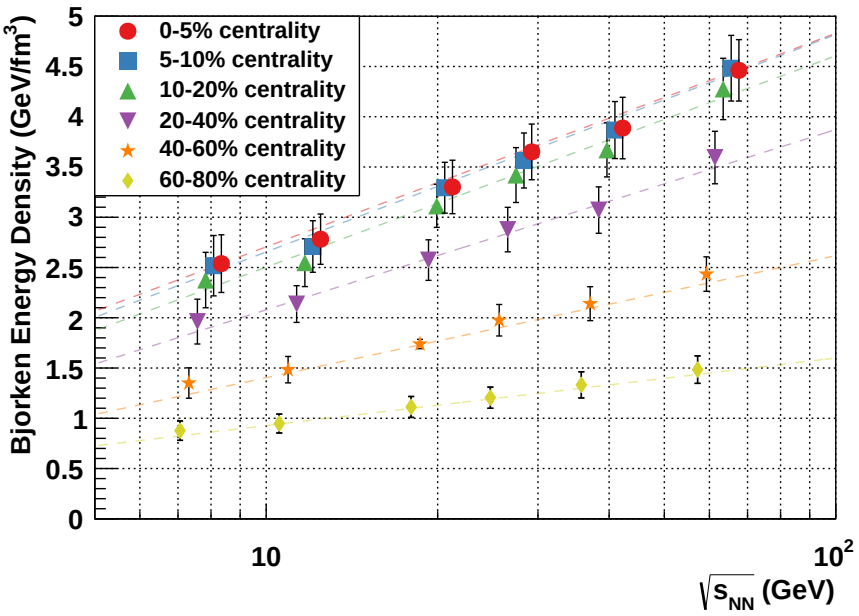

Figure 7.3: Bjorken energy density

Energy density estimates for various centrality bins at each of the BES energies. The quoted error bars represent systematic uncertainties from the fitting procedure. The data points for each centrality bin at a given collision energy are offset slightly along the x axis for clarity in reading the error bars. The lines are logarithmic fits to guide the eye.

To find the volume of the equilibrated system as a function of centrality in accordance with these assumptions we can treat the gold nuclei as hard spheres with radii of 7.3 fm [105] and express the area of overlap times the 2 fm longitudinal expanse as roughly $213\left[\cos^{-1}(\sqrt{c}) - \sqrt{c(1-c)}\right]$ fm^3 where c ranges from 0 for most central to 1 for most peripheral. This allows us to get some idea of the centrality dependence in addition to the collision energy dependence of the energy density, though neglecting radial expansion becomes increasingly problematic in peripheral events because of their relatively small transverse size. An additional assumption of radial expansion with $\beta_\perp \approx 0.6$ over this same 1 fm/c time scale would reduce the central energy density estimates by about 15% and the peripheral estimates by about 40% from the values shown in Figure 7.3.

Again, we will begin by putting these results in the context of earlier results from other experiments. The energy density estimates for each centrality class exhibit a logarithmic scaling as a function of collision energy as illustrated by the dashed lines in Figure 7.3. Extrapolating the fit for the 0-5% centrality class to $\sqrt{s_{NN}} = 200$ GeV gives a value of 5.5 GeV/fm^3 which is slightly higher than the PHOBOS estimate of 5 GeV/fm^3 but consistent within systematic uncertainties [4]. A further extrapolation to 2.76 GeV yields a value of 7.9 GeV/fm^3, roughly half that of the LHC estimate of 15 GeV/fm^3[5, 6], suggesting that the logarithmic scaling breaks in a similar fashion to that observed with the integrated yields.

We next focus on the actual values of the measurement. Even if we allow for a liberal uncertainty of a factor of 2 on the volume of the system at equilibration, we still find that collisions in the 0-20% centrality range are achieving energy densities above 1 GeV/fm^3 all the way down to $\sqrt{s_{NN}} = 7.7$ GeV. Allowing for a factor of 2 larger volume like this corresponds roughly to the PHOBOS methodology for calculating a lower bound on the density. From this, we conclude that a purely hadronic description is inappropriate in central events at all of the BES energies. The situation for peripheral events is more ambiguous as a lower bound estimate of the energy density would sit very close to the hadronic density of 0.5 GeV/fm^3.

7.4 Baryon/Meson Ratios at High p_T

The various particle ratios that can be constructed from the spectra all shed some light on underlying physics but of particular interest are the proton to pion ratios. To address the question of baryon enhancement we constructed the double ratio of $p(\bar{p})/\pi^{+(-)}$ between central and peripheral events as a function of p_T. At high p_T we would expect this ratio to be one in the absence of any modification to jet fragmentation in central events. In Figure 7.4, we observe that the ratios rise to approximately two at around $p_T = 2$ GeV and then remain constant or rise for the remaining p_T reach. We find no evidence for the turn-off of the baryon enhancement QGP signature at any of the BES energies but we must consider additional factors that will influence these measurements.

There's no reason to expect that fragmentation functions would not be modified in

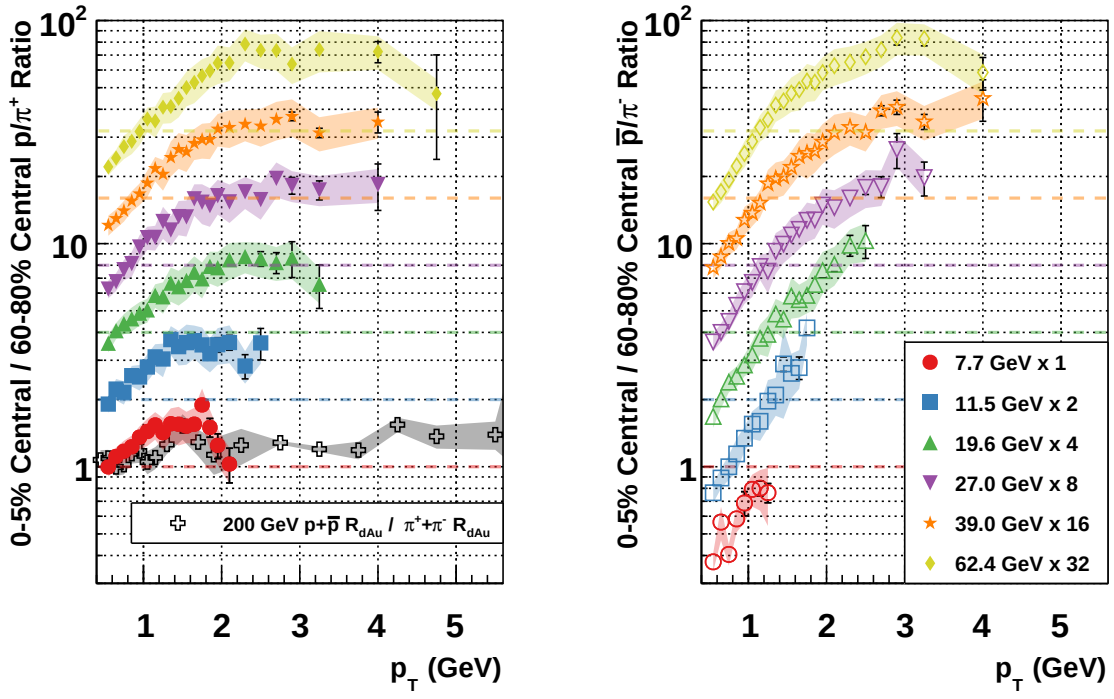

Figure 7.4: p/π enhancement in central events

The ratio of $p(\bar{p})$over $\pi^{+(-)}$ between central and peripheral events as a function of p_T. Each collision energy is offset by a factor of 2 for clarity and a light dashed line illustrates where a ratio of one would be for each respective offset. The $(p+\bar{p})/(\pi^+ + \pi^-)$ ratio in 0-20% top multiplicity events in d+Au over the same ratio in $p+p$ events is shown as a reference for cold nuclear matter effects [68]. Virtually no collision energy dependence is detectable with the given errors and an enhancement of roughly a factor of two is found above $p_T > 2$ GeV for all energies other than $\sqrt{s_{NN}} = 7.7$ GeV where the p_T reach is insufficient to draw a firm conclusion.

cold nuclear matter and, in fact, we would expect that any additional presence of quark matter would lead to a baryon enhancement relative to a vacuum. To help get a handle on this effect we've constructed the double ratio of $(p + \bar{p})/(\pi^+ + \pi^-)$ between 0-20% top multiplicity d+Au events and $p + p$ events at $\sqrt{s_{NN}} = 200$ GeV. This ratio should give us some idea of what degree of baryon enhancement we expect from a jet passing through hadronic matter instead of a vacuum. Above $p_T = 2$ GeV we observe a fairly constant ratio of about ~ 1.4. This is clearly an enhancement but is definitively lower than that observed between central and peripheral Au+Au events. It would be ideal to have additional d+Au and $p + p$ references at the lower collision energies but in their absence we suggest that there might be relatively little energy dependence in this enhancement based on the fact that the Au+Au results exhibit almost none.

Increased baryon stopping in central collisions is an obvious potential source for enhancement and we do indeed see evidence for this in the particle ratios at low p_T. At $\sqrt{s_{NN}} = 7.7$ GeV the positive ratios in this p_T region are markedly higher than the negative ratios, a relationship that remains clear at all collision energies but becomes less pronounced at the higher energies where baryon transport becomes less significant. The positive and negative particle ratios appear to agree well above $p_T = 2.0$ GeV, roughly where we expect hard processes to become dominant. This agreement is strong evidence that baryon stopping is not a driving contributor to the enhancement observed in the high p_T region.

Additionally, we expect radial flow to result in an enhancement of baryons at high p_T in central events. The suppression observed at $p_T < 1.0$ GeV is evidence of protons being boosted to higher momentum by this effect. Radial flow will shape the spectra for protons out to a much higher p_T than it does for pions due to their relative masses resulting in this apparent suppression. It's not possible to determine from this analysis alone whether we're observing evidence of quark deconfinement or simply the effects of radial flow. Hydrodynamic models fit to v_2 flow results used in conjunction with this spectra should, however, be able to put constraints on how much enhancement is coming from radial flow.

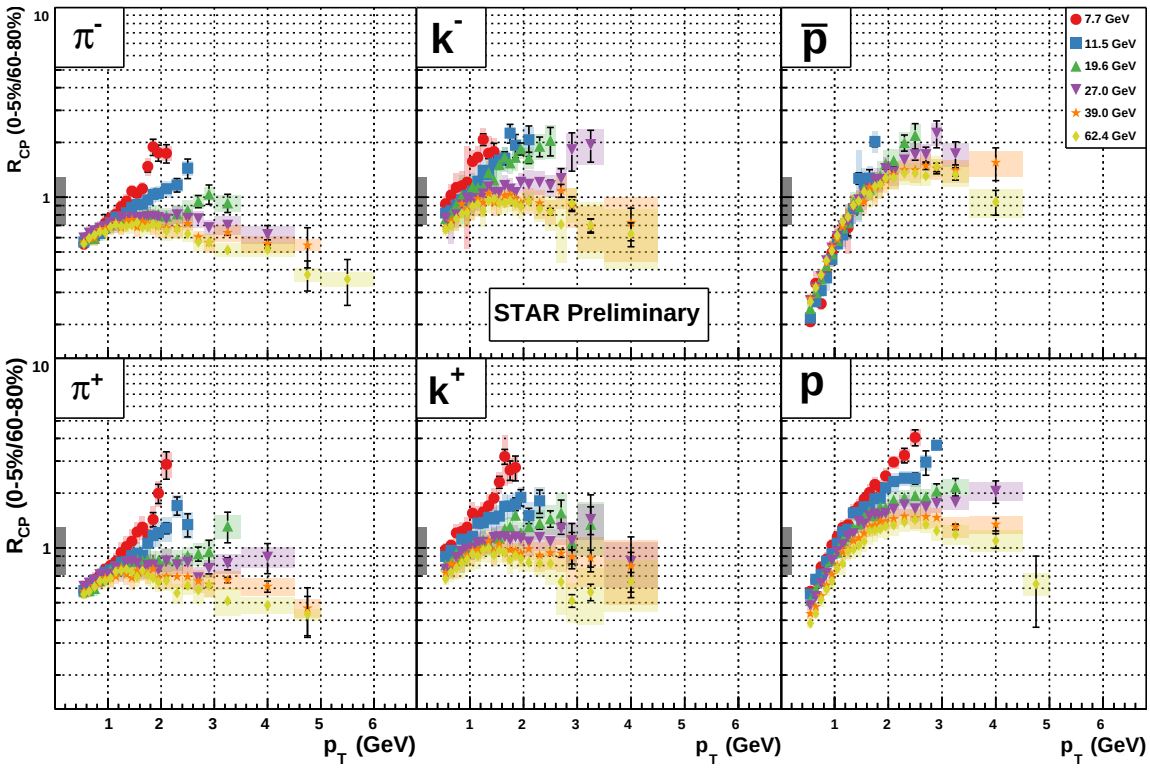

Figure 7.5: Identified particle R_{CP}

Identified particle R_{CP} for each particle species. Error bars are statistical while error boxes are systematic. The gray band at one shows the overall uncertainty in N_{coll} scaling.

7.5 Identified Particle R_{CP}

The hard portion of the p_T spectra should scale with the number of binary collisions in a centrality class. After using a Glauber model to scale the spectra by $1/N_{coll}$ we can take the ratio of central to peripheral collisions to construct the nuclear modification factor R_{CP} and look for evidence of enhancement and suppression. The resulting energy dependence of the nuclear modification factor can be seen for each particle type in Figure 7.5.

One of the most pronounced features of the identified particle R_{CP} is that there is little difference between positive and negative mesons while protons and antiprotons have strikingly different behavior. The proton R_{CP} exhibits a collision energy ordering and

is significantly higher than that of antiprotons at low p_T, both of which are results of baryon stopping. The baryons also exhibit a more significant suppression at low p_T than the mesons which is a result of the greater momentum boost caused by radial flow for heavier particles. These are features that obscure any relationship with hard physics and are one of the main motivators for studying identified particle R_{CP} in addition to that of unidentified charged particles. We sacrifice some of our high p_T reach in order to produce the meson nuclear modification factors which should be largely free of the effects of baryon stopping and less influenced by radial flow.

Moving on to the mesons we notice that the pion R_{CP} appears to have little energy dependence below $p_T = 1.5$ GeV while the kaons exhibit a significant collision energy ordering. This ordering can simply be described by the canonical suppression of thermal phase space in peripheral collisions at lower energies. The overall trends at low transverse momentum are driven by the transition from N_{part} scaling in the soft physics region to N_{coll} scaling in the hard physics region. With the exception of the canonical suppression in kaons and the higher momentum reach of pions, there appears to be little difference in the features of kaons and pions.

Due to all of these factors, we find that the pion R_{CP} will be the most sensitive to evidence of jet suppression. Focusing on the pions, we see a clear peak at roughly $p_T = 1.5$ GeV which is followed by an increasing level of suppression in both $\sqrt{s_{NN}} = 39.0$ and 62.4 GeV. This becomes more subtle at 27.0 GeV but the same feature is apparent. At 19.6 GeV the R_{CP} is consistent with being flat above $p_T = 1.5$ GeV and for the lowest two collision energies there is an exponentially increasing enhancement. We conclude from this that we observe high p_T suppression at $\sqrt{s_{NN}} = 27.0$ GeV and above, that the situation at 19.6 GeV is ambiguous, and that no evidence of suppression was found at the lowest two energies. We also note that the significant change in behavior between 11.5 and 19.6 GeV could easily be the result of the rapidly vanishing phase space for high p_T jets or increasing Cronin enhancement and that the disappearance of the signature does not imply that there does not still exist a deconfined state.

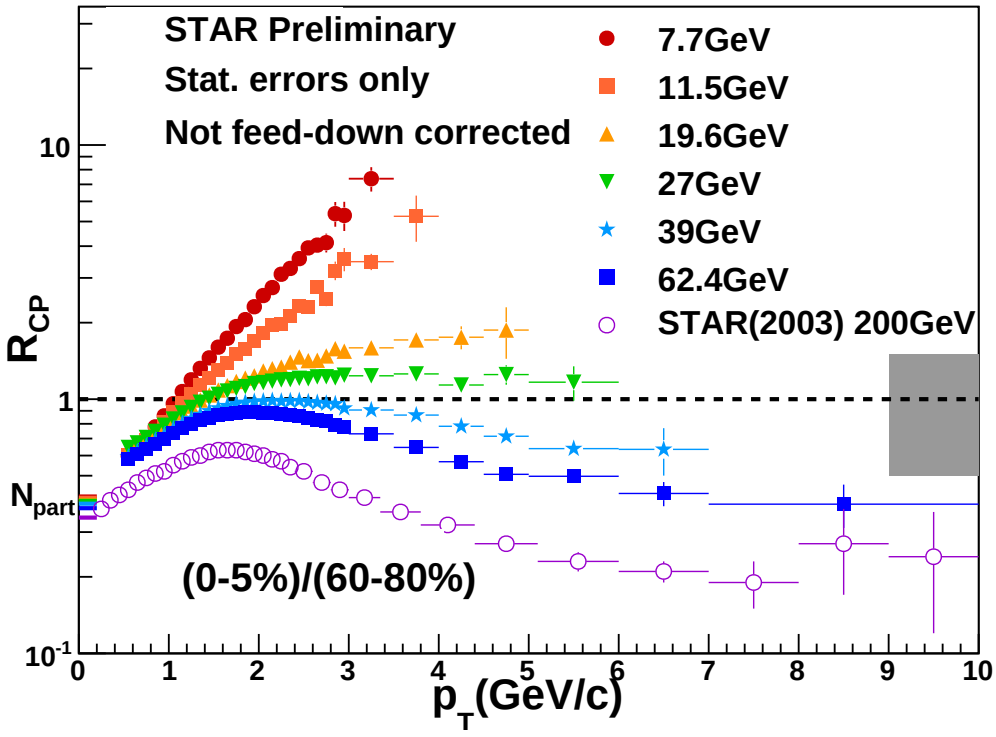

Figure 7.6: Unidentified particle R_{CP}

Charged hadron R_{CP} [106, 11]. Error bars are statistical only. The gray band around one represents the systematic uncertainty in N_{coll} scaling.

7.6 Unidentified Particle R_{CP}

By looking at all unidentified charged particles we are able to extend the momentum reach of the R_{CP} analysis significantly. This portion of the analysis was primarily performed by Stephen Horvat [106] but was also done independently as a crosscheck. To account for detector efficiency in this analysis the identified spectra was used to form a weighted average of each particle's efficiency as a function of p_T. At high momentum this weighted efficiency is constant and can be reasonably extrapolated to high p_T. The effects of energy loss and feeddown were deemed to be insignificant in the high p_T region and were not included. The resulting nuclear modification factors can be found in Figure 7.6.

We see that the peak features at 39 and 62.4 GeV are shifted to a higher p_T relative to their locations in the pion R_{CP}. This is a result of the radial flow contributions from

protons and antiprotons. These same contributions, and possibly baryon enhancement in fragmentation, also serve to eliminate the suppression signature at 27.0 GeV. Overall, we find that the unidentified particle R_{CP} offers significantly higher momentum reach than that of identified particles but that the inclusion of baryons reduces the sensitivity of the observable to suppression and that we are not able to draw any further conclusions.

Chapter 8

Conclusion

In this analysis, we have studied particle production in Au+Au collisions at $\sqrt{s_{NN}}$ =7.7, 11.5, 19.6, 27.0, 39.0, and 62.4 GeV measured using the STAR detector during the BES at RHIC during 2010 and 2011. Exclusive identified momentum spectra have been been extracted for $\pi^{+(-)}$, $K^{+(-)}$, and $p(\bar{p})$ particles in six centrality classes with a focus on maximizing the p_T reach of the spectra for the purpose of making observations relating to hard physics. This comprehensive set of spectra has allowed us to shed light on the collision energy dependence of several key QGP signatures and has served to help bridge the gap between SPS energies and top energy RHIC results.

We've used fits to these spectra to study the integrated density of charged particles at midrapidity as a function of collision energy and have observed a reduction in the rate of increase in the region of 19.6-39.0 GeV. This feature has been found to be driven by the proton yields and is caused by an interplay of the system's response to both increasing energy density and rapidly falling baryon chemical potential.

Our integrated yields and m_T expectations from fits have been used to construct Bjorken energy density estimates. These measurements show that even lower bounds on the energy density of collisions in the 0-20% centrality range fall above 1 GeV/fm^3 for each BES energy. From this, we conclude that a purely hadronic description does not seem possible for central events at any collision energy.

The nuclear modification factors of $p(\bar{p})/\pi^{+(-)}$ ratios between central and peripheral events have been measured as a function of p_T for each collision energy. An enhancement

of roughly a factor of 2 has been observed at $p_T > 2.0$ GeV for both positive and negative particles while the enhancement in d+Au relative to $p+p$ events at 200 GeV is about 1.4. No significant collision energy dependence has been seen in the high transverse momentum region of the observable, although statistics significantly limit the momentum reach at 7.7 and 11.5 GeV. This enhancement is consistent with an expectation of baryon enhancement in jet fragmentation inside a deconfined medium but is also possibly an artifact of radial flow. Hydrodynamic model fits to flow results at these energies should allow for us to put limits on the radial flow and draw a firmer physics conclusion.

Additionally, we've produced both identified and unidentified R_{CP} results for charged hadrons. The unidentified results offer a higher momentum reach but are obfuscated by baryon transport, radial flow, and possibly baryon enhancement in fragmentation. Due to this, we find the clearest picture of high p_T suppression in the pion R_{CP} which shows clear evidence of high p_T suppression at $\sqrt{s_{NN}}$ =27.0, 39.0, and 62.4 GeV and an ambiguous situation at 19.6 GeV. It seems a plausible explanation for this suppression that the jets are passing through a colored medium.

Overall, we've studied several observables which address the formation of a QGP across a range of collision energies. We've observed that baryon enhancement, R_{CP}, and energy densities at 27.0, 39.0, and 62.4 GeV are all suggestive of the presence of a QGP. The energy densities are high enough at 7.7, 11.5, and 19.6 GeV to suggest the existence of a non-hadronic medium but the other signatures are not statistically accessible. This disappearance of the other signatures is primarily the result of the much smaller cross-sections for high p_T processes and only tells us that these signatures are less useful at these energies, not that a QGP is or isn't formed.

Bibliography

[1] G. Chapline, M. Johnson, E. Teller, and M. Weiss. Highly Excited Nuclear Matter. *Physical Review D*, 8(12):4302–4308, December 1973.

[2] F. Karsch. Lattice results on QCD thermodynamics. *Nuclear Physics A*, 698(1-4):199–208, February 2002.

[3] J. D. Bjorken. Highly relativistic nucleus-nucleus collisions: The central rapidity region. *Physical Review D*, 27(1):140–151, January 1983.

[4] B.B. Back, M.D. Baker, M. Ballintijn, et al. The PHOBOS perspective on discoveries at RHIC. *Nuclear Physics A*, 757(1):28–101, 2005.

[5] Berndt Müller, Jürgen Schukraft, and Bolesław Wysłouch. First Results from Pb+Pb Collisions at the LHC. *Annual Review of Nuclear and Particle Science*, 62(1):361–386, November 2012.

[6] Krisztián Krajczár. Charged hadron multiplicity and transverse energy densities in PbPb collisions from CMS. *Journal of Physics G: Nuclear and Particle Physics*, 38(12):124041, December 2011.

[7] J. Adams, C. Adler, M. Aggarwal, et al. Particle-Type Dependence of Azimuthal Anisotropy and Nuclear Modification of Particle Production in Au+Au Collisions at sNN=200 GeV. *Physical Review Letters*, 92(5):052302, February 2004.

[8] Javier Castillo and (for the STAR Collaboration). Elliptic flow of multistrange baryons and in Au+Au collisions at GeV. *Journal of Physics G: Nuclear and Particle Physics*, 30(8):S1207–S1211, August 2004.

[9] S. Adler, S. Afanasiev, C. Aidala, et al. Elliptic Flow of Identified Hadrons in Au+Au Collisions at sNN=200 GeV. *Physical Review Letters*, 91(18):182301, October 2003.

[10] J. Adams, M.M. Aggarwal, Z. Ahammed, et al. Experimental and theoretical challenges in the search for the quark–gluon plasma: The STAR Collaboration's critical assessment of the evidence from RHIC collisions. *Nuclear Physics A*, 757(1-2):102–183, August 2005.

[11] J. Adams, C. Adler, M. M. Aggarwal, et al. Transverse-Momentum and Collision-Energy Dependence of High-p_{T} Hadron Suppression in Au+Au Collisions at Ultrarelativistic Energies. *Physical Review Letters*, 91(17):172302, October 2003.

[12] Xin-Nian Wang. High-pT hadron spectra, azimuthal anisotropy and back-to-back correlations in high-energy heavy-ion collisions. *Physics Letters B*, 595(1-4):165–170, August 2004.

[13] Ivan Vitev and Miklos Gyulassy. High-pT Tomography of d+Au and Au+Au at SPS, RHIC, and LHC. *Physical Review Letters*, 89(25):252301, December 2002.

[14] Yen-Jie Lee. Nuclear modification factors from the CMS experiment. *Journal of Physics G: Nuclear and Particle Physics*, 38(12):124015, December 2011.

[15] B. Alper, H. Böggild, P. Booth, et al. Production spectra of $\pi\pm$, K±, p± at large angles in proton-proton collisions in the CERN intersecting storage rings. *Nuclear Physics B*, 100(2):237–290, December 1975.

[16] P. Abreu et al. Identified charged particles in quark and gluon jets. *The European Physical Journal C*, 17(2):207–222, October 2000.

[17] A. Bartl, H. Fraas, and W. Majerotto. Quark and diquark fragmentation into mesons and baryons. *Physical Review D*, 26(5):1061–1075, September 1982.

[18] K. Adcox, S.S. Adler, S. Afanasiev, et al. Formation of dense partonic matter in relativistic nucleus–nucleus collisions at RHIC: Experimental evaluation by the PHENIX Collaboration. *Nuclear Physics A*, 757(1-2):184–283, August 2005.

[19] L. Ahle, Y. Akiba, D. Beavis, et al. Baryon emission at target rapidities in Si+Al,Cu,Au collisions at 14.6A GeV/c and Au+Au collisions at 11.7A GeV/c. *Physical Review C*, 55(5):2604–2614, May 1997.

[20] L. Ahle, Y. Akiba, K. Ashktorab, et al. Centrality and collision system dependence of antiproton production from p+A to Au+Au collisions at AGS Energies. *Nuclear Physics A*, 638(1-2):427c–430c, August 1998.

[21] I. Bearden, H. Bø ggild, J. Boissevain, et al. Particle production in central Pb+Pb collisions at 158A GeV/c. *Physical Review C*, 66(4):044907, October 2002.

[22] T. Anticic, B. Baatar, D. Barna, et al. Energy and centrality dependence of deuteron and proton production in Pb+Pb collisions at relativistic energies. *Physical Review C*, 69(2):024902, February 2004.

[23] Transverse mass distributions of neutral pions from 208Pb-induced reactions at 158 · A GeV | Eur. Phys. J. C.

[24] S. Adler, S. Afanasiev, C. Aidala, et al. Scaling Properties of Proton and Antiproton Production in sNN=200 GeV Au+Au Collisions. *Physical Review Letters*, 91(17):172301, October 2003.

[25] Owe Philipsen. The QCD equation of state from the lattice. *Progress in Particle and Nuclear Physics*, 70:55–107, May 2013.

[26] Matthias Bach, Volker Lindenstruth, Owe Philipsen, and Christopher Pinke. Lattice QCD based on OpenCL. *Computer Physics Communications*, 184(9):2042–2052, September 2013.

[27] Top500 List - November 2000 | TOP500 Supercomputer Sites.

[28] Szabolcs Borsányi. Thermodynamics of the QCD transition from lattice. *Nuclear Physics A*, 904-905:270c–277c, May 2013.

[29] Y Aoki, G Endrodi, Z Fodor, S D Katz, and K K Szabó. The order of the quantum chromodynamics transition predicted by the standard model of particle physics. *Nature*, 443(7112):675–8, October 2006.

[30] Owe Philipsen. Status of the QCD phase diagram from lattice calculations. page 10, November 2011.

[31] Edward Shuryak. Physics of strongly coupled quark–gluon plasma. *Progress in Particle and Nuclear Physics*, 62(1):48–101, January 2009.

[32] Helen Caines and for the STAR Collaboration. The RHIC Beam Energy Scan - STAR'S Perspective. June 2009.

[33] H. Hahn, E. Forsyth, H. Foelsche, et al. The RHIC design overview. *Nuclear Instruments and Methods in Physics Research Section A: Accelerators, Spectrometers, Detectors and Associated Equipment*, 499(2-3):245–263, March 2003.

[34] J. Benjamin, C. Carlson, I. Feigenbaum, et al. Injecting RHIC from the Brookhaven Tandem Van de Graaff. In *Proceedings of the 1999 Particle Accelerator Conference (Cat. No.99CH36366)*, volume 4, pages 2277–2279 vol.4. IEEE, 1999.

[35] E.D Courant and H.S Snyder. Theory of the alternating-gradient synchrotron. *Annals of Physics*, 3(1):1–48, January 1958.

[36] L. Ahrens, J. Alessi, W. van Asselt, et al. Status and recent performance of the accelerators that serve as gold injector for RHIC. In *PACS2001. Proceedings of the 2001 Particle Accelerator Conference (Cat. No.01CH37268)*, volume 5, pages 3326–3328. IEEE, 2001.

[37] M Bai, P Cameron, P Cerniglia, et al. RHIC beam instrumentation. *Nuclear Instruments and Methods in Physics Research Section A: Accelerators, Spectrometers, Detectors and Associated Equipment*, 499(2-3):372–387, March 2003.

[38] R. Burns, H.C. Hseuh, R.C. Lee, et al. The RHIC vacuum systems. *Nuclear Instruments and Methods in Physics Research Section A: Accelerators, Spectrometers, Detectors and Associated Equipment*, 499(2-3):349–355, March 2003.

[39] D.S Barton, S Binello, W Buxton, et al. RHIC control system. *Nuclear Instruments and Methods in Physics Research Section A: Accelerators, Spectrometers, Detectors and Associated Equipment*, 499(2-3):356–371, March 2003.

[40] A. Etkin, T. Williams, S. Musselino, et al. The RHIC personnel safety system. *Nuclear Instruments and Methods in Physics Research Section A: Accelerators, Spectrometers, Detectors and Associated Equipment*, 499(2-3):388–391, March 2003.

[41] M Anerella, J Cottingham, J Cozzolino, et al. The RHIC magnet system. *Nuclear Instruments and Methods in Physics Research Section A: Accelerators, Spectrometers, Detectors and Associated Equipment*, 499(2-3):280–315, March 2003.

[42] D Bruno, W Eng, P.K Feng, et al. RHIC magnet electrical system. *Nuclear Instruments and Methods in Physics Research Section A: Accelerators, Spectrometers, Detectors and Associated Equipment*, 499(2-3):316–348, March 2003.

[43] M.A. Iarocci, D. Brown, J. Sondericker, et al. RHIC cryogenics. *Nuclear Instruments and Methods in Physics Research Section A: Accelerators, Spectrometers, Detectors and Associated Equipment*, 499(2-3):264–279, March 2003.

[44] M. Harrison, T. Ludlam, and S. Ozaki. RHIC project overview. *Nuclear Instruments and Methods in Physics Research Section A: Accelerators, Spectrometers, Detectors and Associated Equipment*, 499(2-3):235–244, March 2003.

[45] T. Ludlam. Overview of experiments and detectors at RHIC. *Nuclear Instruments and Methods in Physics Research Section A: Accelerators, Spectrometers, Detectors and Associated Equipment*, 499(2-3):428–432, March 2003.

[46] M Adamczyk, L Antvorskov, K Ashktorab, et al. The BRAHMS experiment at RHIC. *Nuclear Instruments and Methods in Physics Research Section A: Accelerators, Spectrometers, Detectors and Associated Equipment*, 499(2-3):437–468, March 2003.

[47] B.B Back, M.D Baker, D.S Barton, et al. The PHOBOS detector at RHIC. *Nuclear*

Instruments and Methods in Physics Research Section A: Accelerators, Spectrometers, Detectors and Associated Equipment, 499(2-3):603–623, March 2003.

[48] K. Adcox, S.S. Adler, M. Aizama, et al. PHENIX detector overview. *Nuclear Instruments and Methods in Physics Research Section A: Accelerators, Spectrometers, Detectors and Associated Equipment*, 499(2-3):469–479, March 2003.

[49] K.H. Ackermann, N. Adams, C. Adler, et al. STAR detector overview. *Nuclear Instruments and Methods in Physics Research Section A: Accelerators, Spectrometers, Detectors and Associated Equipment*, 499(2-3):624–632, March 2003.

[50] Y. Wang, H.S. Chen, W.C. Ding, et al. Performance of a new LMRPC prototype for the STAR MTD system. *Nuclear Instruments and Methods in Physics Research Section A: Accelerators, Spectrometers, Detectors and Associated Equipment*, 640(1):85–90, June 2011.

[51] B. Surrow. The STAR Forward GEM Tracker. *Nuclear Instruments and Methods in Physics Research Section A: Accelerators, Spectrometers, Detectors and Associated Equipment*, 617(1-3):196–198, May 2010.

[52] M. Anderson, J. Berkovitz, W. Betts, et al. The STAR time projection chamber: a unique tool for studying high multiplicity events at RHIC. *Nuclear Instruments and Methods in Physics Research Section A: Accelerators, Spectrometers, Detectors and Associated Equipment*, 499(2-3):659–678, March 2003.

[53] L. Kotchenda, S. Kozlov, P. Kravtsov, et al. STAR TPC gas system. *Nuclear Instruments and Methods in Physics Research Section A: Accelerators, Spectrometers, Detectors and Associated Equipment*, 499(2-3):703–712, March 2003.

[54] J. Abele, J. Berkovitz, J. Boehm, et al. The laser system for the STAR time projection chamber. *Nuclear Instruments and Methods in Physics Research Section A: Accelerators, Spectrometers, Detectors and Associated Equipment*, 499(2-3):692–702, March 2003.

[55] M. Anderson, F. Bieser, R. Bossingham, et al. A readout system for the STAR time projection chamber. *Nuclear Instruments and Methods in Physics Research Section A: Accelerators, Spectrometers, Detectors and Associated Equipment*, 499(2-3):679–691, March 2003.

[56] B Bonner, H Chen, G Eppley, et al. A single Time-of-Flight tray based on multigap resistive plate chambers for the STAR experiment at RHIC. *Nuclear Instruments and Methods in Physics Research Section A: Accelerators, Spectrometers, Detectors and Associated Equipment*, 508(1-2):181–184, August 2003.

[57] W.J Llope, F Geurts, J.W Mitchell, et al. The TOFp/pVPD time-of-flight system for STAR. *Nuclear Instruments and Methods in Physics Research Section A: Accelerators, Spectrometers, Detectors and Associated Equipment*, 522(3):252–273, April 2004.

[58] F. Geurts, M. Shao, B. Bonner, et al. Performance of the prototype MRPC detector for STAR. *Nuclear Instruments and Methods in Physics Research Section A: Accelerators, Spectrometers, Detectors and Associated Equipment*, 533(1-2):60–64, November 2004.

[59] W.J. Llope. Multigap RPCs in the STAR experiment at RHIC. *Nuclear Instruments and Methods in Physics Research Section A: Accelerators, Spectrometers, Detectors and Associated Equipment*, 661:S110–S113, January 2012.

[60] F.S. Bieser, H.J. Crawford, J. Engelage, et al. The STAR trigger. *Nuclear Instruments and Methods in Physics Research Section A: Accelerators, Spectrometers, Detectors and Associated Equipment*, 499(2-3):766–777, March 2003.

[61] J.S Lange, C Adler, J Berger, et al. The STAR level-3 trigger system. *Nuclear Instruments and Methods in Physics Research Section A: Accelerators, Spectrometers, Detectors and Associated Equipment*, 453(1-2):397–404, October 2000.

[62] C. Adler, A. Denisov, E. Garcia, et al. The RHIC zero-degree calorimeters. *Nuclear Instruments and Methods in Physics Research Section A: Accelerators, Spectrometers, Detectors and Associated Equipment*, 499(2-3):433–436, March 2003.

[63] C. A. Whitten, Ahovi Kponou, Yousef Makdisi, and Anatoli Zelenski. The Beam-Beam Counter: A Local Polarimeter at STAR. In *AIP Conference Proceedings*, volume 980, pages 390–396. AIP, February 2008.

[64] M. Beddo, E. Bielick, T. Fornek, et al. The STAR Barrel Electromagnetic Calorimeter. *Nuclear Instruments and Methods in Physics Research Section A: Accelerators, Spectrometers, Detectors and Associated Equipment*, 499(2-3):725–739, March 2003.

[65] Michael L. Miller, Klaus Reygers, Stephen J. Sanders, and Peter Steinberg. Glauber Modeling in High-Energy Nuclear Collisions. *Annual Review of Nuclear and Particle Science*, 57(1):205–243, November 2007.

[66] B. B. Back, M. D. Baker, M. Ballintijn, et al. Collision geometry scaling of Au+Au pseudorapidity density from sqrt[s_{NN}]=19.6to200GeV. *Physical Review C*, 70(2):021902, August 2004.

[67] H. Bichsel. Particle identification at STAR-TPC with ionization measurements. pages 448–454, 2003.

[68] J. Adams, M.M. Aggarwal, Z. Ahammed, et al. Identified hadron spectra at large transverse momentum in and collisions at. *Physics Letters B*, 637(3):161–169, June 2006.

[69] L. Adamczyk, J. K. Adkins, G. Agakishiev, et al. Elliptic flow of identified hadrons in Au+Au collisions at sqrt[s_{NN}]=7.7–62.4 GeV. *Physical Review C*, 88(1):014902, July 2013.

[70] J. Adams, C. Adler, M. Aggarwal, et al. Identified Particle Distributions in pp and Au+Au Collisions at sNN=200 GeV. *Physical Review Letters*, 92(11):112301, March 2004.

[71] Ekkard Schnedermann, Josef Sollfrank, and Ulrich Heinz. Thermal phenomenology of hadrons from 200A GeV S+S collisions. *Physical Review C*, 48(5):2462–2475, November 1993.

[72] Ekkard Schnedermann and Ulrich Heinz. Relativistic hydrodynamics in a global fashion. *Physical Review C*, 47(4):1738–1750, April 1993.

[73] D. Teaney, J. Lauret, and E. V. Shuryak. A Hydrodynamic Description of Heavy Ion Collisions at the SPS and RHIC. October 2001.

[74] Ulrich Heinz and Peter F. Kolb. Emission angle dependent pion interferometry at RHIC and beyond. 2002.

[75] C. Adler, Z. Ahammed, C. Allgower, et al. Identified Particle Elliptic Flow in Au+Au Collisions at sNN=130 GeV. *Physical Review Letters*, 87(18):182301, October 2001.

[76] Fabrice Retière and Michael Lisa. Observable implications of geometrical and dynamical aspects of freeze-out in heavy ion collisions. *Physical Review C*, 70(4):044907, October 2004.

[77] Tamás S Biró and Berndt Müller. Almost exponential transverse spectra from power law spectra. 2004.

[78] G. Wilk and Z. Włodarczyk. Interpretation of the Nonextensivity Parameter q in Some Applications of Tsallis Statistics and Lévy Distributions. *Physical Review Letters*, 84(13):2770–2773, March 2000.

[79] C Tsallis. Possible generalization of Boltzmann-Gibbs statistics. *Journal of statistical physics*, 52:479–487, 1988.

[80] A. Adare, S. Afanasiev, C. Aidala, et al. Identified charged hadron production in p+p collisions at sqrt[s]=200 and 62.4 GeV. *Physical Review C*, 83(6):064903, June 2011.

[81] B. Abelev, J. Adams, M. Aggarwal, et al. Strange particle production in p+p collisions at s=200 GeV. *Physical Review C*, 75(6):064901, June 2007.

[82] K. Aamodt, N. Abel, U. Abeysekara, et al. Production of pions, kaons and protons in pp collisions at sNN= 900GeV with ALICE at the LHC. *The European Physical Journal C*, 71(6):1655, June 2011.

[83] V. Khachatryan, a. M. Sirunyan, A. Tumasyan, et al. Strange particle production in pp collisions at sNN = 0.9 and 7 TeV. *Journal of High Energy Physics*, 2011(5):64, May 2011.

[84] Zebo Tang, Yichun Xu, Lijuan Ruan, et al. Spectra and radial flow in relativistic heavy ion collisions with Tsallis statistics in a blast-wave description. *Physical Review C*, 79(5):051901, May 2009.

[85] S. Agostinelli, J. Allison, K. Amako, et al. Geant4—a simulation toolkit. *Nuclear Instruments and Methods in Physics Research Section A: Accelerators, Spectrometers, Detectors and Associated Equipment*, 506(3):250–303, July 2003.

[86] J. Allison, K. Amako, J. Apostolakis, et al. Geant4 developments and applications. *IEEE Transactions on Nuclear Science*, 53(1):270–278, February 2006.

[87] S Bass. Microscopic models for ultrarelativistic heavy ion collisions. *Progress in Particle and Nuclear Physics*, 41:255–369, March 1998.

[88] M Bleicher, E Zabrodin, C Spieles, et al. Relativistic hadron-hadron collisions in the ultra-relativistic quantum molecular dynamics model. *Journal of Physics G: Nuclear and Particle Physics*, 25(9):1859–1896, September 1999.

[89] Ming Shao and the STAR Collaboration. Pion, kaon and (anti-)proton production in Au+Au collisions at. *Journal of Physics G: Nuclear and Particle Physics*, 31(4):S85–S92, April 2005.

[90] L. Ahle, Y. Akiba, K. Ashktorab, et al. Particle production at high baryon density in central Au+Au reactions at 11.6A GeV/c. *Physical Review C*, 57(2):R466–R470, February 1998.

[91] B. Back, R. Betts, J. Chang, et al. Proton emission in Au+Au collisions at 6, 8, and 10.8 GeV/nucleon. *Physical Review C*, 66(5):054901, November 2002.

[92] L Ahle, Y Akiba, K Ashktorab, et al. An excitation function of K− and K+ production in Au+Au reactions at the AGS. *Physics Letters B*, 490(1-2):53–60, September 2000.

[93] J. Klay, N. Ajitanand, J. Alexander, et al. Charged pion production in 2A to 8AGeV central Au+Au Collisions. *Physical Review C*, 68(5):054905, November 2003.

[94] James Dunlop. *No Title*. PhD thesis, Massachusetts Institut of Technology, 1999.

[95] S. Afanasiev, T. Anticic, D. Barna, et al. Energy dependence of pion and kaon production in central Pb+Pb collisions. *Physical Review C*, 66(5):054902, November 2002.

[96] T. Anticic, B. Baatar, D. Barna, et al. Energy and centrality dependence of deuteron and proton production in Pb+Pb collisions at relativistic energies. *Physical Review C*, 69(2):024902, February 2004.

[97] B. Back, M. Baker, D. Barton, et al. Significance of the Fragmentation Region in Ultrarelativistic Heavy-Ion Collisions. *Physical Review Letters*, 91(5):052303, August 2003.

[98] B. Back, M. Baker, D. Barton, et al. Charged-Particle Multiplicity near Midrapidity in Central Au+Au Collisions at sNN=56 and 130 GeV. *Physical Review Letters*, 85(15):3100–3104, October 2000.

[99] B. Back, M. Baker, M. Ballintijn, et al. Scaling of charged particle production in d+Au collisions at sNN=200GeV. *Physical Review C*, 72(3):031901, September 2005.

[100] B. Back, M. Baker, D. Barton, et al. Energy Dependence of Particle Multiplicities in Central Au+Au Collisions. *Physical Review Letters*, 88(2):022302, December 2001.

[101] B. Back, M. Ballintijn, M. Baker, et al. Centrality dependence of the charged particle multiplicity near midrapidity in Au+Au collisions at sNN=130 and 200 GeV. *Physical Review C*, 65(6):061901, June 2002.

[102] B. B. Back, M. D. Baker, M. Ballintijn, et al. Collision geometry scaling of Au+Au pseudorapidity density from sqrt[s_{NN}]=19.6to200GeV. *Physical Review C*, 70(2):021902, August 2004.

[103] L. Adamczyk, J. K. Adkins, G. Agakishiev, et al. Beam-Energy Dependence of the Directed Flow of Protons, Antiprotons, and Pions in Au+Au Collisions. *Physical Review Letters*, 112(16):162301, April 2014.

[104] John Novak. *Energy Dependence of Fluctuation and Correlation Observables of Transverse Momentum in Heavy-Ion CollisionsNo Title*. PhD thesis, Michigan State University, 2014.

[105] E.J. Downie, R.N. Lee, A.I. Milstein, and G. Ron. Charge asymmetry in high-energy photoproduction in the electric field of a heavy atom. *Physics Letters B*, 728:645–649, January 2014.

[106] Stephen Horvat. Charged Hadron Nuclear Modification Factors in the Beam Energy Scan from STAR. *PoS*, CPOD2013:002, 2013.

[107] C. Bromberg, D. Chaney, D. Cohen, et al. Cross Sections and Charged-Particle Multiplicities at 102 and 405 GeV/c. *Physical Review Letters*, 31(26):1563–1566, December 1973.

[108] K. Redlich and A. Tounsi. Strangeness enhancement and energy dependence in heavy ion collisions. *The European Physical Journal C - Particles and Fields*, 24(4):589–594, August 2002.

[109] A.S. Carroll, I.-H. Chiang, T.F. Kycia, et al. Total cross sections of $\pi\pm$, K$\pm$, p and on protons and deuterons between 200 and 370 GeV/c. *Physics Letters B*, 80(4-5):423–427, January 1979.

[110] I. Arsene, I.G. Bearden, D. Beavis, et al. Quark–gluon plasma and color glass condensate at RHIC? The perspective from the BRAHMS experiment. *Nuclear Physics A*, 757(1-2):1–27, August 2005.

[111] J. Cronin, H. Frisch, M. Shochet, et al. Production of hadrons at large transverse momentum at 200, 300, and 400 GeV. *Physical Review D*, 11(11):3105–3123, June 1975.

[112] D. Antreasyan, J. Cronin, H. Frisch, et al. Production of hadrons at large transverse momentum in 200-, 300-, and 400-GeV p-p and p-nucleus collisions. *Physical Review D*, 19(3):764–778, February 1979.

[113] Hongyu Da, Xiangli Cui, Yichun Xu, et al. High-pT hadronic trigger using electromagnetic calorimeter with the STAR detector. *Nuclear Instruments and Methods in Physics Research Section A: Accelerators, Spectrometers, Detectors and Associated Equipment*, 698:19–25, January 2013.

Input the Appendices here.